
Università degli Studi di Padova
Dipartimento di Ingegneria dell'Informazione

# Analysis and Design of Radio Frequency Integrated Circuits for Breast Cancer Radar Imaging in CMOS Technology

Tesi di: Matteo Bassi

Scuola di Dottorato in Ingegneria dell'Informazione
Indirizzo in Scienza e Tecnologia dell'Informazione
Ciclo XXV

**Supervisore**:
Chiar.mo Prof. Andrea Neviani

**Direttore della Scuola**:
Chiar.mo Prof. Matteo Bertocco

**Coordinatore di Indirizzo**:
Chiar.mo Prof. Carlo Ferrari

*You can quit if you want, and no one will care.*
*But you will know the rest of your life.*
— John Collins (Founder of The Ironman Triathlon)

To my father and to my mother
To Irene

# Acknowledgements

*Ad astra, per aspera.*
— Pierfrancesco Bassi

I definitely had a lot of fun as a Ph.D. student, but acknowledgements are (always) difficult to make. There is some people that you would like to acknowledge for what they did and some other people that you would like to acknowledge for what they did not. Then you would also like to acknowledge things - not living people, and that is also difficult to make.
Among the people that did something (read: a lot), I would like to thank Prof. Andrea "Il Bevi" Bevilacqua for his patience and competence. I definitely had a great time with him. He motivated me and helped me out whenever I was asking. I also want to thank Prof. Andrea Neviani for his unlimited kindness and attention to the details. Most importantly, Prof. Andrea Bevilacqua and Prof. Andrea Neviani taught me the right way of working in terms of fairness, accuracy and responsibility. I will take care to keep their teachings with me, with the hope of being eventually able to work together again.
I spent some months at the University of Pavia. I would like to thank Prof. Francesco "Frank" Svelto, Prof. Andrea "Mazza" Mazzanti and Andrea Ghilioni for injecting enthusiasm in me in every technical and nontechnical discussion we had together.
Then, I want to thank Michele Caruso, for the great time we had together. He sustained me in most of my dark moments while not killing me whenever I was getting too crabby (mostly close to tape-outs or when not eating enough). Thanks for the infinite number of coffees you had with me without drinking any (he does not like coffee), for waiting three years to play squash with me and for the endless nice conversations we had together. You are a great friend, and I hope to have the pleasure to work again with you in the future.
I would like to thank Paolo Baracca, for being a real friend and constant inspiration for me.
Behind the electronics scene (or maybe not even too much), I want to thank my father for being an endless source of enthusiasm and encouragement. Thank you for showing me that honor, responsibility and quality thinking bring happiness and satisfaction: *ad astra, per aspera*.
Last, but not least, I would like to thank Irene for guiding me with the hand and listening to me talking about electronics while pretending to be enthusiastic as I am - love does that, I know.

*Padova, 31st December 2012* M. B.

# Abstract

Breast cancer is by far the most incident tumor among female population. Early stage prevention is a key factor in delivering long term survival of breast cancer patients. X-ray mammography is the most commonly used diagnostic technique to detect non-palpable tumors. However, 10-30 % of tumors are missed by mammography and ionizing radiations together with breast compression do not lead to comfort in patient treatment. In this context, ultrawideband microwave radar technology is an attractive alternative. It relies on the dielectric contrast of normal and malignant tissues at microwave frequencies to detect and locate tumors inside the breast. This work presents the analysis and design of radio frequency integrated circuits for breast cancer imaging in CMOS technology.

The first part of the thesis concerns the system analysis. A behavioral model of two different transceiver architectures for UWB breast cancer imaging employing a SFCW radar system are presented. A mathematical model of the direct conversion and super heterodyne architectures together with a numerical breast phantom are developed. FDTD simulations data are used to on the behavioral model to investigate the limits of both architectures from a circuit-level point of view. Insight is given into I/Q phase inaccuracies and their impact on the quality of the final reconstructed images. The result is that the simplicity of the direct conversion architecture makes the receiver more robust toward the critical impairments for this application.

The second part of the thesis is dedicated to the circuit design. The main achievement is a 65 nm CMOS 2-16 GHz stepped frequency radar transceiver for medical imaging. The RX features 36 dB conversion gain, $>29$ dBm compression point, 7 dB noise figure, and 30 Hz 1/f noise corner. The TX outputs 14 dBm with $>40$ dBc harmonic rejection and $<109$ dBc/Hz phase noise at 1 MHz offset. Overall power dissipation is 204 mW from 1.2 V supply. The radar achieves 3 mm resolution within the body, and 107 dB dynamic range, a performance enabling the use for breast cancer diagnostic imaging. To further assess the capabilities of the proposed radar, a physical breast phantom was synthesized and two targets mimicking two tumors were buried inside the breast. The targets are clearly identified and correctly located, effectively proving the performance of the designed radar as a possible tool for breast cancer detection.

# Sommario

Il tumore al seno é di gran lunga il piú comune tumore nella popolazione femminile. La mammografia a raggi X é la tecnica diagnostica piu' utilizzata e copre un ruolo chiave nella prevenzione, elemento fondamentale per assicurare la cura e la sopravvivenza dei pazienti. La mammografia presenta peró importanti limitazioni, quali la necessitá di comprimere il seno durante l'esame, l'esposizione a radiazioni ionizzanti e l'alta percentuale di falsi negativi. In questo contesto, sembra interessante poter affiancare alla mammografia nuove tecniche diagnostiche, quali le tecnologie di imaging a radar nel range delle microonde, che si basano sull'intrinseco contrasto dielettrico presente tra tessuti benigni e maligni nel range delle microonde. Questo lavoro presenta quindi l'analisi e il progettazione di circuiti integrati in radio frequenza per l'imaging del tumore al seno in tecnologia CMOS.

Nella prima parte della tesi vengono analizzati i modelli comportamentali di due diverse architetture di ricetrasmissione per l'imaging del tumore al seno. Vengono sviluppati dei modelli di ricetrasmettitori a conversione diretta e a super eterodina basati su radar SFCW e un modello numerico del seno. Simulazioni FDTD vengono utilizzate per investigare i limiti delle architetture considerate e individuare i punti critici nel design circuitale. Particolare attenzione viene dedicata ai mismatch tra i canali I e Q del ricetrasmettitore e al loro impatto sulla qualitá finale dell'immagine. Il risultato é che la semplicitá della conversione diretta rende il ricetrasmettitore piú robusto alle piú critiche non-idealitá circuitali per questa applicazione.

Nella seconda parte viene presentato un ritrasmettitore SFCW operante da 2 a 16 GHz per imaging medicale realizzato in tecnologia CMOS 65 nm. Il ricevitore ha un guadagno di conversione di 36 dB, punto di compressione $> 29$ dBm, figura di rumore di 7 dB e corner 1/f a 30 Hz. Il trasmettitore ha una potenza di uscita di 14 dBm, con reiezione delle armoniche di $> 40$ dBc e rumore di fase $< 109$ dBc/Hz ad un offset di 1 MHz. Il sistema completo consuma 204 mW. Il radar presentato raggiunge una risoluzione di 3 mm dentro al corpo umano con un range dinamico di 107 dB. Per dimostrarne l'efficacia, é stato realizzato un seno sintetico dentro al quale sono stati inclusi due tumori. Il radar ha evidenziato correttamente i due tumori nella giusta posizione, a dimostrazione della sua efficacia come possibile strumento diagnostico.

# Contents

# List of Figures

# List of Tables

# 1 Introduction

In the last few years, a significant growth of research involving the use of microwaves to image the human body has been taking place. Among the many examples of ongoing research, the use of microwaves for breast cancer diagnostic imaging has seen an increase of interest [2, 5–14]. Fig. 1.1(a) shows the tumor incidence rate over 100 thousand people. Breast cancer is by far the most incident tumor among the female population [1], with a rate that is at least twice the one of any other tumor. A 5-year rate of survival of only 20 % is recorded if the tumor is detected in a metastasized stage, as highlighted in Fig. 1.1(b). On the other hand, 98 % cure rates are possible if detected in its early stages, definitely making early detection a key factor in delivering long term survival to breast cancer patients [1].

The mammography, consisting of X-ray imaging of a compressed breast, is the most commonly used diagnostic technique to detect non-palpable breast tumors [15]. However, ionizing radiations cause health hazard, while breast compression induces considerable discomfort in patients. Moreover, circumstances like the presence of dense glandular tissue around the tumor, the absence of microcalcifications in the early stages of the disease, tumors located close to the chest wall or underarm result in a 10-30% rate of false negatives. Additionally, the fraction of positive mammograms not ending up in the diagnosis of an actual malignancy is about 10% [15, 16]. However, an invasive biopsy that involves the partial removal of breast tissues, is necessary to asses the false positive.

The limitations of X-ray mammography have provided the motivations for the development of complementary imaging tools [17, 18]. According to the Institute of Medicine (IOM), an ideal breast screening tool should feature low health risk, be sensitive to specific malignancies, detect breast cancer in its early and hence curable stages, be noninvasive, cost effective and widely available, while introducing minimal discomfort for the patient and providing reliable results for interpretation [15, 18].

Among the several contrast-based diagnostic techniques, ultrawideband (UWB) microwave technology [5–7, 10–13] has raised a considerable interest. This technique leverages the contrast between the dielectric properties of benignant and neoplastic tissues at microwave frequencies to identify the presence and location of significant scatters [19]. The general approach is to illuminate the breast with a UWB pulse from a number of antenna locations. Thanks to the difference in the dielectric properties, the waves scatter at each dielectric interface. Consequently,

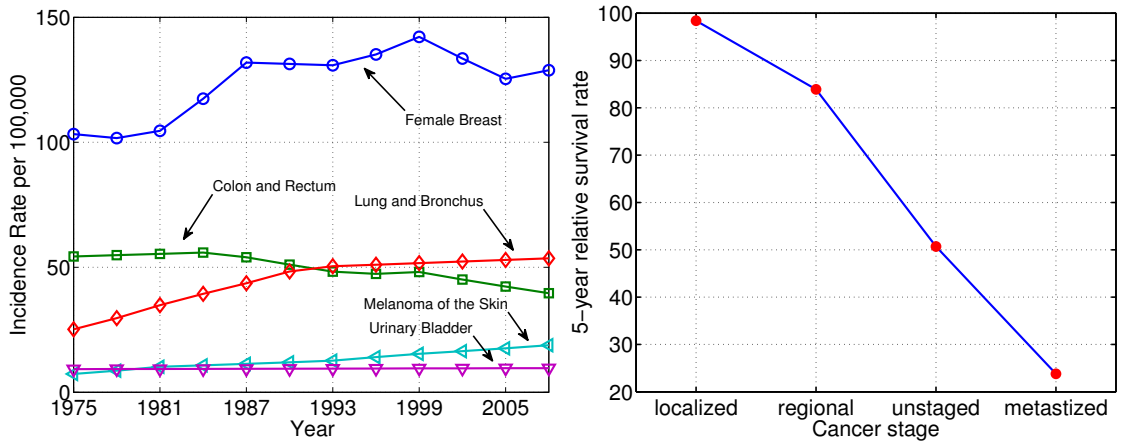


(a) (b)

Figure 1.1: (a) Age-adjusted tumor incidence rates per 100000 people grouped by cancer site [1]. (b) 5-year relative survival rate with respect to the tumor stage [1].

the retrieved waveforms contain information about the scattering object, such as the distance and size. By collecting and post-processing the backscatters, a high resolution dielectric map of the breast can be generated.

In this context, the sensitivity and ability to detect small tumors is allowed by the combined action of the UWB microwave radar technology and the intrinsic contrast between the neoplastic tissue and the benignant tissues around it. The electrical contrast allows to enhance the tumor response with respect to the surrounding healthy tissue, therefore enabling an efficient detection and diagnosis. Additionally, the high-resolution breast dielectric map is expected to be generated very rapidly. This feature, along with the fact that the breast does not need to be compressed as in X-ray mammography, leads to a more comfortable and rapid patient examination. Further, UWB microwave technology does not involve the use of ionizing radiations, certainly resulting more attractive to patients.

## 1.1 Motivations

Several works on microwave imaging reported over the past years show the feasibility of this technique [2, 5–13]. Actually, the imaging system show in Fig. 1.2 has demonstrated excellent results compared to X-rays mammography [3]. In this system, the patient is lying face down in the supine position while the breast is extending through a hemispherical hole of about 17 cm diameter. The hole is filled with coupling liquid for better matching and covered by a highly-dense 60-elements antenna array. An electromechanical switching system, whose size is at least three times the one of the antenna array, connects the antenna elements to a 8-port vector network analyzer (VNA) that allows 15 simultaneous S-parameter measurements in the frequency range up to 8 GHz. The whole switching and acquisition system connected to the VNA is driven by a PC and assembled on a hydraulic trolley to ease the transportation. This system achieved excellent results in terms of acquisition time and success rate compared to X-rays, and it is undergoing clinical trials [20].

A feature that is common to the works that, so far, report also experimental data, is the use of

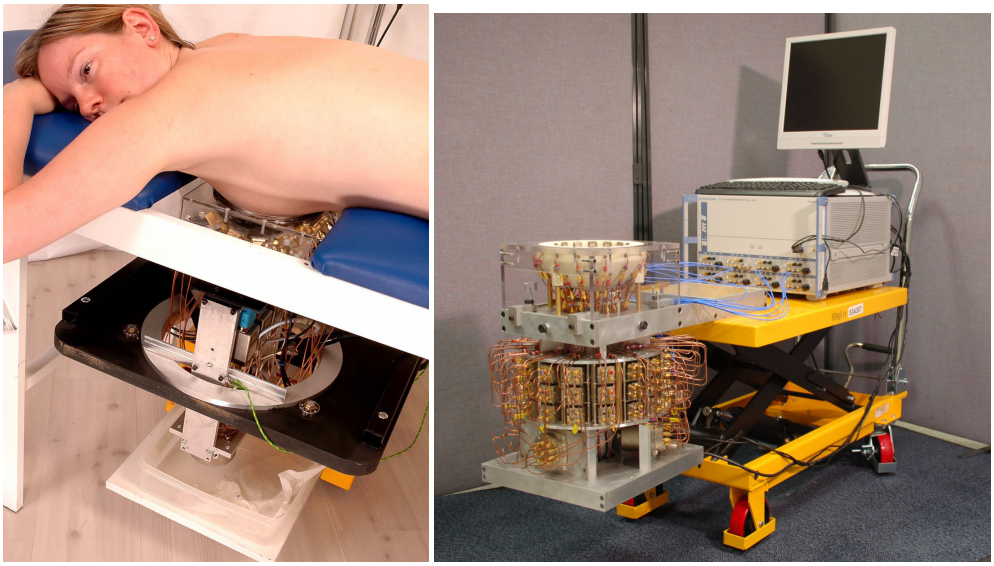

(a) (b)

Figure 1.2: Microwave radar-based clinical setup for breast cancer detection presented by the University of Bristol. (a) patient lying in a prone position [2]. (b) complete array and switch assembly integrated with the VNA and the hydraulic trolley [3].

microwave laboratory equipment to implement the radar transceiver. As an example, the system presented in [3] requires an electromechanical switching system to interface its 60-element antenna array to the 8-port VNA that is used as radar transceiver (c.f. Fig. 1.2(b)). The complex switching system introduces losses and limits the number of simultaneous measurements thus increasing the acquisition time. Due to its bulky and costly high-frequency rigid-cable connections, the number of antenna array elements is limited. Further, it requires the system to be mounted on an hydraulic trolley to ease the transportation. All these elements reduce its ability to be used as a cost-effective solution for follow-up post-treatment cancer surveillance [21].

As a matter of fact, the development of custom hardware is seen as a critical need by the microwave imaging community in order to improve the performance and reduce the size and cost of the system [17]. Contextually, enabled by the advances in silicon technologies, a clear trend towards the integration of radar imaging systems for security and industrial applications has emerged in recent years [22–25]. Therefore, given the aforementioned considerations, the system analysis and design of a compact module made of a CMOS integrated radar transceiver companioned by two specifically designed wideband patch antennas for simultaneous transmission and reception is the main motivation lying behind this work. A dedicated integrated circuit can be tailored to cover the specific wide bandwidth required by medical imaging, while achieving very large dynamic ranges. The miniaturization carried about by system integration allows to envision an antenna array made of modules in which each compact or planar antenna is directly assembled together with the radar transceiver chip. A switching system is therefore avoided along with any high frequency interconnects. Only signals at low frequencies are to be distributed to the array elements. At the same time, having a transceiver for each antenna removes any limitation on the number of simultaneous measurements that can be performed. A more compact, higher performance, and lower cost system results.

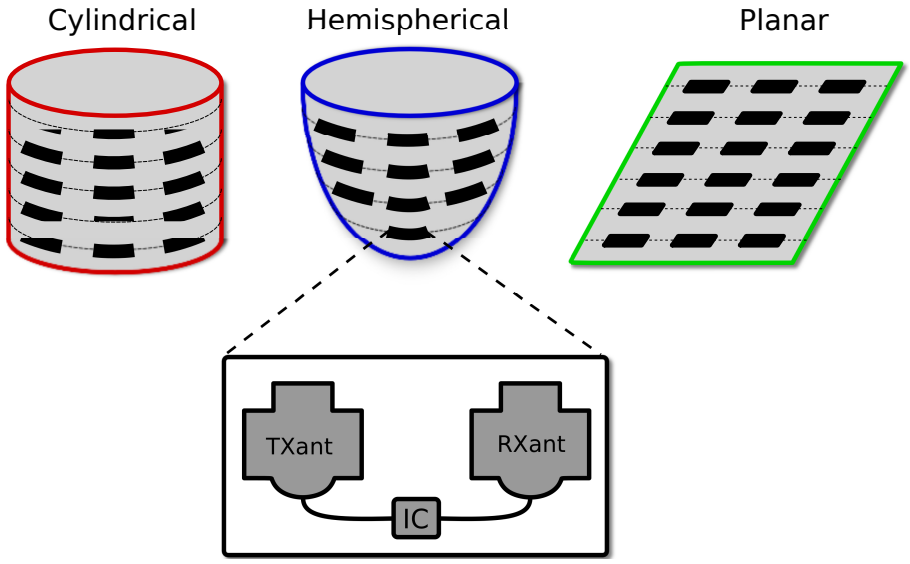


Figure 1.3: The three different antenna array configurations that can be used to scan the breast in a radar imaging system. Below, the envisioned imaging module made of the CMOS radar transceiver and the two wideband patch antennas.

## 1.2 System Overview

In a breast cancer radar imaging system, the patient positioning leads to different system configurations [5]. In the supine position, a planar array of antennas is used to scan the naturally flattened breast of the patient. In the prone position, the patient lies face down while the breast is extending through the examination hole, where it is scanned by an hemispherical or cylindrical antenna array. The resulting planar, hemispherical and cylindrical configurations are depicted in Fig. 1.3. Among them, the hemispherical one is preferred because it allows the imaging from many view angles while the prone position reduces the motion effects due to patient breathing [20]. In this scenario, the antenna array elements could be made of the module proposed in Sec. 1.1, in which the radar transceiver is directly assembled together with the two wideband patch antennas, as depicted in Fig. 1.3. Such a module would allow a highly reconfigurable antenna array while yielding a more compact, higher performance and lower cost system.

In principle, the UWB microwave imaging radar relies on the transmission of UWB pulses and the detection of the radiation backscattered by the disuniformity of the dielectric properties of the illuminated volume. Its main building blocks are then an antenna array, one or more transceivers connected to the array that generate the UWB pulses and detect the backscattered radiation, and an imaging algorithm that processes the received waveforms to obtain a high-resolution map of the target. As discussed later on, in order to achieve the resolution required by the breast imaging application, a combination of short pulse duration (well below 1 ns), and receiver dynamic range (in excess of 100 dB) is required, which makes the implementation of the transceiver in the time domain extremely difficult. In particular, the receiver should be able to sample the backscattered waveform with a sampling frequency well over 10 GHz and convert it to the digital domain with over 16 bit of resolution.

This problem can be circumvented by adopting the stepped-frequency, continuous-wave (SFCW) radar concept, where the UWB time domain pulse is synthetically generated start-

ing from measurements performed in the frequency domain. In a SFCW radar, a sequence of $M$ sinusoidal tones, whose frequency is stepped from $f_{\min}$ to $f_{\max}$ with increments equal to $\Delta f$, is generated. Provided that the frequency span $f_{\max} - f_{\min}$ is large enough, the set of M tones corresponds to the frequency-domain representation of an UWB pulse. Actually, since the set of M tones is discrete, the corresponding waveform in the time domain is a discrete-time pulse with a sampling interval given by $\Delta T = (M \cdot \Delta f)^{-1}$. On the receiver side, the detection of the backscattered signal consists of a series of $M$ narrowband measurements that recover the amplitude and the phase of each reflected sinusoidal tone. High resolution pulses are then obtained by performing the inverse Fourier transform (IFFT) on the collected results, thus retrieving time-domain waveforms [26–28]. It is then easy to see that, provided the illuminated target does not change during the measurement acquisition time, the approach based on SFCW radar is equivalent (in as much as the output waveform is the same) to a pulsed radar operating in the time domain.

It should be noted that, while the overall bandwidth of both the transmitter output stage and the receiver input stage must be as wide as $B = f_{\max} - f_{\min}$, the system instantaneous bandwidth (and thus, the noise bandwidth) can be basically as narrow as desired, since the signal to be handled at each step is a purely sinusoidal tone. The narrow noise bandwidth and the processing gain inherent in the IFFT are key factors to achieve the large instantaneous dynamic range imposed by the application.

## 1.3 System Challenges

With the rapid development of wireless communications technology and the widespread use of mobile phones and other wireless devices there have been increasing interest in understudying the principles lying behind the interactions of the electromagnetic radiation on the human body. It is worth to remember that studying the reciprocal action of electromagnetic waves with biological tissues is a fundamental step in developing and utilizing medical applications and therapies. In this context, the challenges of designing a system for breast cancer tumor detection mainly arise from the inner nature of the human body tissues and their electromagnetic properties that are here exploited for positive purposes.

Medical statistical studies show that the depth of a typical normal, nonlactating human breast is in the order of 4 cm [29]. This suggests that a mildly-compressed breast would span less than 4 cm between the skin surface and the rib cage. Almost 50 % of all breast tumors occur in the quadrant near the armpit where the breast is less than about 2.5 cm deep [30]. Further, the survival of patients with invasive carcinoma is a inverse function of tumor size, independent of the method of detection [31, 32]. Smallest tumors are in the order of 9-10 mm [31]. Thus, the intended application of the imaging radar requires the system to be able to detect breast tumors with a minimum size of 9-10 mm even when located several centimeters below the skin surface. These requirements translate into challenging system-level specifications for the radar front-end.

First of all, the resolution of the SFCW radar depends on the frequency range and on topological parameters, such as the position and number of the antennas. As highlighted in Fig. 1.4, the achievable resolution in the slant-range, $\Delta r_s$, i.e. in the direction of wave propagation, is directly

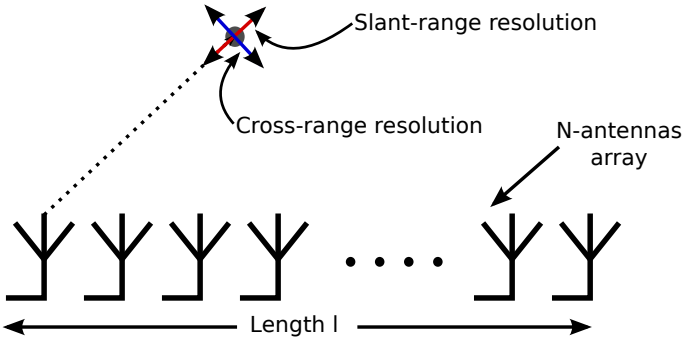


Figure 1.4: Typical arrangement of a N-antennas array for SFCW radar imaging.

related to the overall bandwidth of the system, $B = f_{\max} - f_{\min}$, as

$$\Delta r_s \approx \frac{v}{2B}, \tag{1.1}$$

where $v$ is the wave velocity in the medium. Topological parameters, such as the number of antennas and the antenna-to-antenna distance directly influence the resolution in the cross-range, i.e. on the plane orthogonal to the direction of wave propagation. By placing $N$ equally spaced antennas next to each other, an equivalent synthetic aperture antenna of length $l$ is generated, yielding, in the case of UWB waveforms, a resolution in the cross-range, $\Delta r_c$, of [33,34]

$$\Delta r_c \approx \frac{R}{l}\frac{v}{B}, \tag{1.2}$$

where $R$ is the target range.

The step $\Delta f$ in the frequency sweep determines the maximum unambiguous range $R_{\max}$, i.e. the maximum distance a target can be in order to be reliably detected without spatial aliasing, as

$$R_{\max} = \frac{v}{2\Delta f}. \tag{1.3}$$

For example, the choice of $\Delta f$ =90 MHz step results in a maximum unambiguous range of 0.55 m, more than enough for the intended application, avoiding any issue with spatial aliasing.

To put this in perspective, a bandwidth $B = 14$ GHz allows to achieve a 3 mm slant-range resolution inside the body, enough to detect even the smallest neoplastic enclosures. Taking 2 GHz as minimum frequency to ease some circuit-level implementation issues (i.e. ac-coupling, antenna response, etc.) and maximize the signal penetration depth, the system has to cover a frequency range from 2 to 16 GHz. To obtain a similar resolution in the cross-range, $l$ must be twice the maximum expected range. The depth of a typical normal, non-lactating human breast is in the order of 4 cm [29], such that $l \geq 10$ cm is adequate.

However, achieving the desired spatial resolution is not enough to guarantee a successful detection of the tumors. In fact, attenuation of signals in the GHz range by body tissue is strong, and increases with frequency [19]: as an example, a few cm of tissue are sufficient to attenuate a signal at 10 GHz by more than 80 dB, as clarified in Chapter 2. At the same time, the interface between air and skin, due to the large difference in the dielectric properties of the two media, causes a strong reflection which is subject to much less attenuation with respect to the tumor

response, since in this case the signal path is shorter (from the antenna to the skin and back) and in air. When the time-domain waveform is retrieved, the relatively weak reflection coming from the tumor is buried below the large reflection from the air-skin interface [5, 12]. This implies that the instantaneous dynamic range of the system has to be in excess of 100 dB. The development of custom hardware is instrumental on tackling this challenging issue. The use of matching liquids to reduce the dielectric discontinuity at the skin interface has been proposed [20]. However, this complicates the setup of the system, and the almost unavoidable presence of air gaps hampers the correct imaging operation.

Finally, the signal-to-clutter ratio, and thus, the image quality, are significantly improved by a highly dense antenna array [33, 34]. Unfortunately, when the system is based on the use of a large-bandwidth VNA to implement the radar transceiver, the combination of a large number of antennas and the limited number of ports of the VNA requires to a develop complex electromechanical switching systems to connect the VNA to the antennas through rigid coaxial cables. The switching system introduces losses, reducing the ability to couple the signal deeper inside the breast. Moreover, the size of the switching system and its bulky interconnects, as well as of the VNA itself, drifts the system away from being portable, dramatically increases the cost of the setup and reduces its ability to be used as a cost-effective solution for follow-up post-treatment cancer surveillance [21]. A radar system leveraging a custom integrated transceiver, as the one proposed here, allows then to eliminate the need of electromechanical switches and of long, high-frequency interconnects, also reducing significantly the size and the cost of the system.

## 1.4 Image Reconstruction Algorithm

Generally talking, the image reconstruction algorithms used in UWB microwave systems for breast cancer detection fall intro three different categories: holographic methods, tomographic methods and confocal radar imaging methods. The confocal imaging algorithms exploit the principle of radar synthetic focusing, which allows to selectively focus the energy of significant backscatters to generate a multidimensional image of the scenario. In fact, it has been widely used in remote sensing, land-mine detection and surveillance.

The quality of the reconstructed image strongly depends on acquiring as many scattered signals as possible at as many view angles as possible of the illuminated scene. A set of $N$ time-domain waveforms is available at the output of a $N$-antenna array and integrated SFCW radar transceivers (or commercial VNAs). The early-time content of each waveform is dominated by the large skin reflection while the late-time content contains the tumor backscatter and clutter signal. Since the skin response has a much greater amplitude than the tumor response, the early-time content needs to be removed without corrupting the useful tumor signal. As proposed in [35], a calibration signal can be generated for each antenna by averaging the time-response of any other antenna. This signal is then subtracted from the raw data. It is clear that this calibration procedure is effective as long as each antenna has the same distance from the skin. If this is not the case, more sophisticated algorithms have been presented to estimate the correct distance and efficiently remove the skin content [7, 36, 37].

Once the skin reflection has been properly removed, the $N$ calibrated waveforms

$$I_i(t), \quad i = 1, \ldots, N \tag{1.4}$$

contain only the tumor response and clutter. The image creation can then be based on a simple delay-multiply-and-sum algorithm [12]. This simple algorithm consists on calculating the intensity of each pixel by properly focusing the received signal on the pixel coordinates. First, the round trip time $\tau_i(x,y,z)$ from the $i$-th antenna to the pixel of coordinates $(x,y,z)$ is calculated. Then, the time-domain signals $I_i(t)$ are time-shifted by the calculated round-trip time $\tau_i(x,y,z)$. In this way, the information on the considered pixel embedded in the various time-domain signals is aligned in time to the point $t = 0$. Finally, the intensity $I(x,y,z)$ of the pixel of coordinates $(x,y,z)$ is calculated by coherently summing the contribution of all the antennas

$$I(x,y,z) = \left[ \sum_{i=1}^{N} I_i(\tau_i(x,y,z)) \right]^2 . \tag{1.5}$$

By iterating the presented procedure for each pixel of the image, a high resolution 2-D or even 3-D dielectric map of the inner breast can be obtained [5, 12].

## 1.5 Conclusions

The key factor in delivering long term survival to breast cancer patients is early time prevention. X-ray mammography is the most used diagnostic technique but shows limitations both on the technical and social profile. In fact, even if it can be considered a well-know technique, a large fraction of patients drastically refuse to expose to ionizing radiations for a screening procedure. In this context, social considerations - that often lie behind the scene in scientific articles, show up and become prominent. There is no scientific evidence that can convince people to screen for breast cancer if they do not feel comfortable in taking part in the exam. And X-ray mammography is without any doubt uncomfortable: breast is strongly compressed while bombed with ionizing radiations. This pushes the X-ray diagnostic tool toward the "invasive region", in which any patient feels some kind of interference with its natural being and thus tries to avoid the test if not strictly necessary. These considerations clearly point out how X-ray cannot be considered a feasible mass screening diagnostic tool, as it cannot certainly convince and reach all the people.

This provides even stronger motivations for the developing of innovative and more performant diagnostic imaging techniques, such as the one based on UWB microwave imaging radar techniques. In this context, the development and realization of a microwave front-end transceiver for breast cancer imaging could represent the enabling technology for future clinical trials with patients, first step toward its integration with the actually used diagnostic techniques. Besides, it is certainly worth to remember that the research on UWB microwave imaging radar transceivers can be considered an important step toward the practical involvement of the microwave field in a meaningful objective, that may be able to provide not only an essential diagnostic tool for breast cancer screening, but also excite future research into equally worth medical diagnostic fields.

The thesis is organized as follows. In Chapter 2, the possible architectures and circuit-level specifications for the targeted SFCW microwave radar transceiver are explored. In Chapter 3, the transceiver architecture is presented. Chapter 4 and 5 illustrate the circuit-level design of the receiver and the whole transceiver along with the electrical measurements. Chapter 6 shows the imaging experiments carried out to assess the functionality of the realized microwave radar

transceiver front-end as an effective imaging element for breast cancer detection. Chapter 7 draws the conclusions.

# System Analysis Part I

# 2 Architectures and Circuit Constraints

In this chapter, a behavioral analysis of two different transceiver architectures for UWB breast cancer imaging employing a SFCW radar system is presented. A mathematical model of the direct conversion and super heterodyne architectures together with a numerical breast phantom are developed. FDTD simulations data are used on the behavioral model to investigate the limits of both architectures from a circuit-level point of view. Insight is given into I/Q phase inaccuracies and their impact on the quality of the final reconstructed images. The result is that the simplicity of the direct conversion makes the receiver more robust towards the critical circuit impairments for this application, that is the random phase mismatches between the TX and RX local oscillators [38, 39].

The chapter is organized as follows. In Section 2.2, the investigated transceiver architectures are presented from a system level point of view. Section 2.3 describes the breast phantom numerical setup and the receiver behavioral model, along with the image-processing algorithm. In Section 2.4, the impact of the relevant circuit-level impairments is explained. The super heterodyne and direct conversion architectures are compared in Section 2.5. Conclusions are summarized in Section 2.6.

## 2.1 Introduction

Based on the motivations highlighted in the previous chapter, we investigate the design of a low cost CMOS integrated circuit (IC) that can be connected to an array of antennas to perform monostatic or bistatic measurements. Each IC acts as a transceiver, generating stepped frequency waveforms and collecting back the scattered signals from the breast. In this chapter, we provide insight into the choice of the possible transceiver architecture through the study of an accurate behavioral model. The performance of the system is evaluated for different values of the circuit level impairments. Transmission power, receiver conversion gain, $IIP_2$, 1 dB compression point, noise figure and baseband filter bandwidth, as well as the ADC resolution are directly set, while the amount of the I/Q phase imbalance, as well as the phase noise are modeled as stochastic processes. The impact of all the relevant circuit-level impairments is then carefully assessed with respect to the signal-to-clutter ratio (SCR) of the final reconstructed breast image. Specifications for the integrated circuit are derived based on the application requirements.

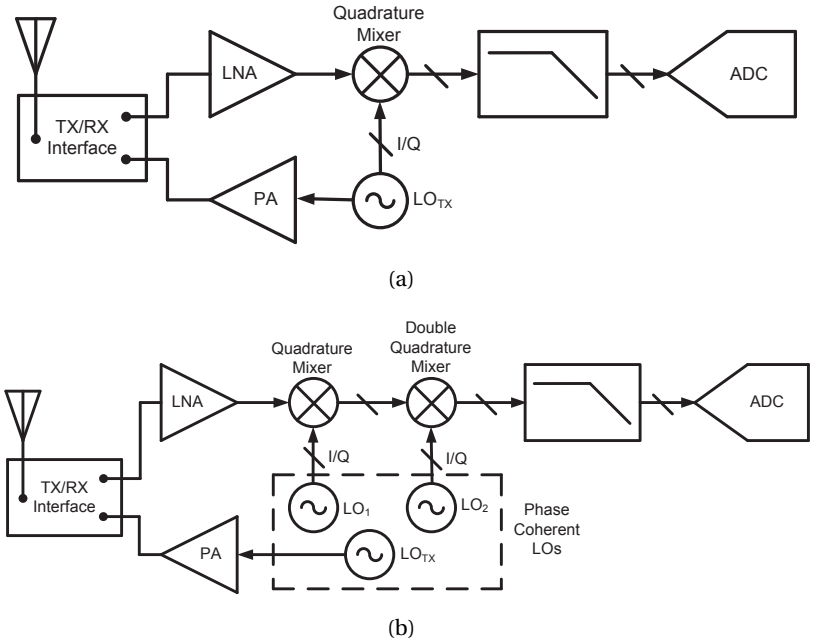


Figure 2.1: Proposed UWB transceiver architectures. 2.1(a) direct conversion. 2.1(b) super heterodyne.

## 2.2 System Description

As detailed out in the Chapter 1, the UWB imaging technique we consider is based on the SFCW radar operation [40, 41], where a set of continuous wave is irradiated over a wide band of frequencies. Narrowband measurements are performed to retrieve the waves that bounce back in presence of objects with different electro-magnetic (EM) properties with respect to the surrounding breast tissue (c.f. Section 1.3). High resolution is obtained by performing the inverse Fourier transform (IFFT) on the collected results, thus generating the time-domain waveforms [26]. From the waveform and the time of flight of the back scattered pulses it is possible to derive a 2-D or even 3-D image of the volume that has been illuminated [5, 12], as anticipated in Section 1.4.

The system block diagram of the investigated UWB stepped frequency transceiver architectures is shown in Fig. 2.1 [42]. The direct conversion is the more compact and straightforward solution. A PLL generates the local oscillator (LO) frequencies in the desired range and feeds them into the mixer and the power amplifier (PA). The LO signal is irradiated through the antenna, which is supposed to be available to work in both transmit/receive modes connected to a TX/RX switch, circulator, or directional coupler. An approach with different TX and RX antennas is also possible, both in monostatic and multistatic form. The details about the physical implementation of the antenna are in Chapter 6. For simplicity, isotropic antennas were assumed. However, the analysis still holds if the antenna has constant gain over a suitable beamwidth to cover the breast surface. In case different TX/RX antennas are employed, sufficient isolation between the two is required, as discussed in Section 2.3.2. The backscattered signal from the breast is collected by the antenna, amplified by the LNA and downconverted by the quadrature mixer. The baseband signal is low-pass filtered and digitized before signal processing (IFFT, imaging) is performed.

As previously discussed, the detection of the cancerous tissues is based on the difference in

their EM properties compared to the healthy breast tissue. However, the breast skin also shows different EM parameters, behaving as an undesired scatterer that produces a large unwanted signal. Signal-wise, this corresponds to a large interferer that cannot be easily separated from the desired signal neither in the frequency, nor in the time domain [5, 7]. Together with the request of high resolution in the ADCs, the presence of the large "in-band" interferer results in a peculiar consequence for the system. Along with the typical circuit impairments of the direct conversion receivers (flicker noise, second-order nonlinearities, dc offsets) there is an image issue related to I/Q mismatches: the image is indeed the signal received in the desired band, but the latter is dominated by the spurious skin backscatter. As such I/Q imbalances are critical.

The issues with I/Q mismatches may be alleviated by a super heterodyne scheme. In this case, the image signals are out-of-band. Given the intended application and the widely available spectral monitoring techniques for the medical screening environment, it is reasonable to assume that the breast imaging is performed in a controlled environment such that out-of-band interferers are nearly absent, thus relaxing the requirements on the I/Q mismatches. On the other hand, the super heterodyne architecture adds complexity to the receiver scheme (see Fig. 2.1(b)). A two-step quadrature downconversion is performed to a low intermediate frequency (IF). To enable possible hardware reuse between the transmitter and the first receiver LO, the first IF is assumed to be around 100 MHz, while the second IF is assumed to be in the 100 kHz range. Note that the high resolution requirement for the ADCs forces to employ a low second IF. The main issue with the frequency generation in the super heterodyne architecture is that all the employed LOs have to be coherent, that is they have to display a fixed and well known phase relationship when the baseband signal is sampled. Such a condition is, on the other hand, guaranteed in the direct conversion transceiver, as the same LO is shared between the transmitter and the receiver.

## 2.3 Simulation Deck and System Modeling

An accurate model of the system is necessary to properly explore possible transceiver architectures for breast cancer imaging, and evaluate them in terms of circuit-level impairments impact on the imaging capabilities of the system. The modeling effort is based on three parts. First, the propagation of the waves in the breast tissues has to be addressed. This has been done by setting up a numerical model of the various breast tissues (skin, normal tissue, malignant tissue) and by performing finite-difference time-domain EM simulations on a numerical breast phantom. The result is a set of transfer functions that relate the transmitted tones and the received backscattered signals for different scenarios (with or without the presence of a tumor, different tumor positions, different antenna configurations). Second, a baseband equivalent model of the receiver including all the circuit-level impairments has been developed, such that the signals at the receiver antenna, obtained by means of the transfer functions describing the propagation through the breast, can be related to the signals output by the receiver. Third, a set of simulated receiver output signals, assumed to come from different antennas in an array, are processed to obtain an image of the breast, such that the impact of the circuit non-idealities on the quality of the image can be readily appreciated.

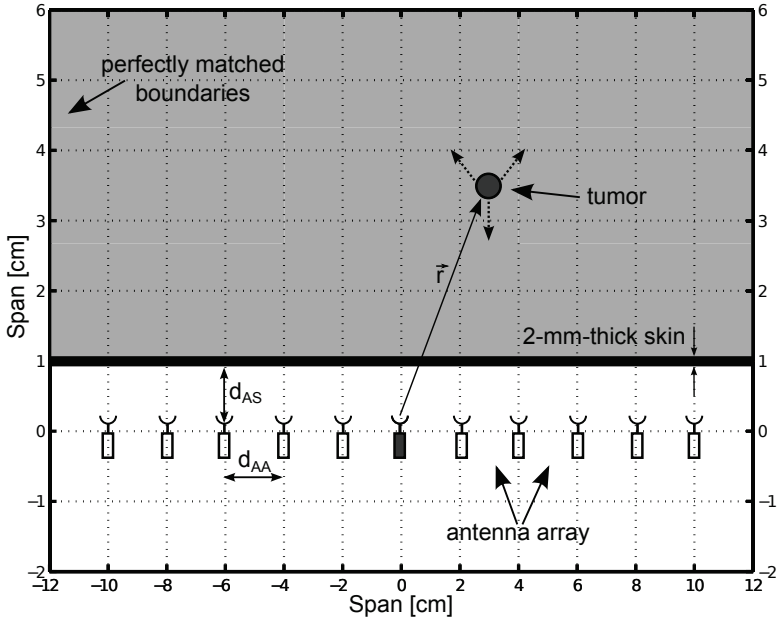


Figure 2.2: 2-D model of the numerical breast phantom together with the antenna array.

### 2.3.1 Numerical Breast Model

In a breast cancer imaging system, the patient orientation leads to two main different system configurations, as anticipated in Chapter 1. In the planar configuration, the patient lies in a supine position, and a planar array of antennas scans the naturally flattened breast [43]. In the cylindrical configuration, the patient is oriented in a prone position with the breast naturally extended in an examination hole. In the latter, a cylindrical array is used to scan the breast [44]. As reported in [5], the two configurations show equivalent properties. Since the focus of this work is on the relative performance of different integrated transceiver architectures, we consider a simple scenario based on a two-dimensional (2-D) configuration, where a linear antenna array is supposed to be placed at the surface of the naturally flattened breast of a patient. The obtained image will of course show a cross-section of the breast. Despite its simplicity, this configuration is realistic in that the propagation of the waves in the breast, as well as the scattering due to the skin and the tumor, are well captured. Moreover, it can be related to more complex scenarios, assuming the antenna array is conformally placed along or around the breast. Figure 2.2 shows the 2-D breast model together with a possible configuration of the antenna array and tumor position. The breast is modeled as a half-space of breast tissue bounded by a thin layer of skin. A linear array of antennas is located at a distance $d_{\mathrm{AS}}$ from the surface of the breast, immersed in air. The antenna-to-antenna distance is $d_{\mathrm{AA}}$.

The antenna array may be a physical one, or a synthetic one, meaning that it can be obtained by mechanical repositioning of one antenna. The array of transceivers can make use of a single antenna (or even an antenna pair for TX and RX) that is moved step-by-step in the correct positions by a mechanical system while being connected to the right transceiver by a matrix of switches. Alternatively, a single transceiver and antenna (or antenna pair) can be moved by a mechanical system to cover all the synthetic aperture length. According to [45], a significant test case is given by a tumor with a diameter of 4 mm, which has thus been selected as a target for the imaging. The thickness of the skin layer is set to 2 mm. The distance vector $\vec{r}$ represents the distance from any antenna to the tumor. The setup enables a flexible configuration of the

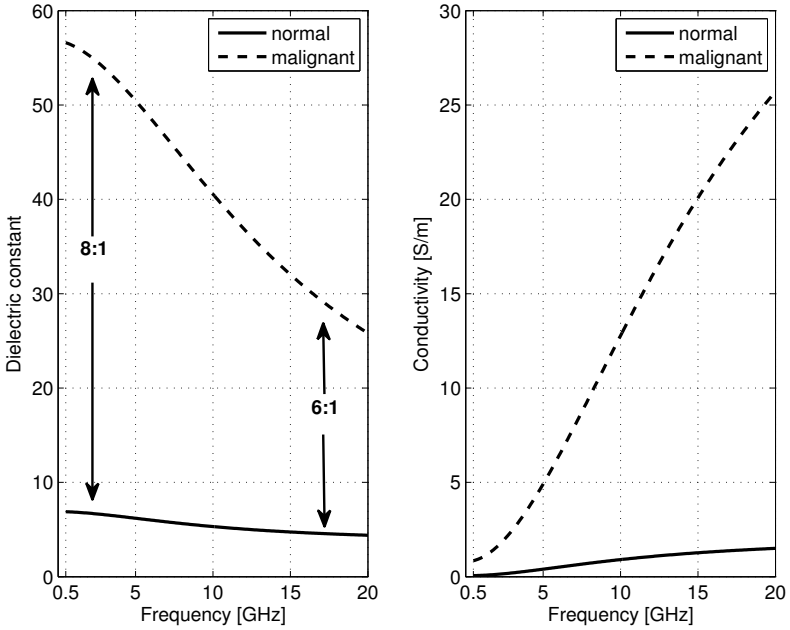


Figure 2.3: Comparison between the Cole-Cole curves of the normal (solid) and malignant (dashed) tissue used in the 2-D numerical breast model.

number of antennas, the antenna-to-antenna distance and the tumor location with respect to the antenna array. The antenna-to-skin $d_{\mathrm{AS}}$ is chosen to be 1 cm. This is a realistic and feasible assumption for the breast screening [5]. Once the length $l$ of the antenna array is chosen, different number of antennas result in different values of $d_{\mathrm{AA}}$. The number of antennas does not have an impact on the resolution (for a fixed $l$). However, a larger number of antennas increases the processing gain of the array while reducing the level of the sidelobes of the beamforming system [34]. At the same time, $d_{\mathrm{AA}} \geq v/(2B)$ is desirable [34], especially if one is constrained by the allowable dimensions of the antenna array. All this taken into account, we chose 11 antennas over a length $l = 20$ cm as a typical test case. The overall accuracy of the numerical breast model is dictated by the approach used to capture the dispersive EM properties of the tissues. Each material in the model was assigned the appropriate frequency-dependent dielectric properties (electrical conductance $\sigma$ and relative dielectric constant $\epsilon_r$) in the range from 2 to 18 GHz as documented in [19], a large scale study on the UWB dielectric properties of normal, benignant and malignant breast tissues from 0.5 to 20 GHz. The dispersive properties of the tissues are incorporated in the model by means of the established four-term one-pole Cole-Cole parametric dispersion model for complex permittivity:

$$\epsilon_r - j\frac{\sigma}{\omega\epsilon_0} = \epsilon_\infty + \sum_{n=1}^{4} \frac{\Delta\epsilon_n}{1 + (j\omega\tau_n)^{(1-\alpha_n)}} - j\frac{\sigma_s}{\omega\epsilon_0}. \tag{2.1}$$

In the model of the normal tissue, adipose-dominated tissue is considered over a glandular-dominated one, as suggested by the histograms of distributions of tissues presented in [19]. The parameters for the adipose-dominated normal tissue ($\epsilon_\infty = 3.581$, $\Delta\epsilon_n = 3.337$, $\tau_n = 15.21$ ps, $\alpha_n = 0.052$, $\sigma_s = 0.053$ S/m) and the malignant tumor ($\epsilon_\infty = 6.749$, $\Delta\epsilon_n = 50.09$, $\tau_n = 10.50$ ps, $\alpha_n = 0.051$, $\sigma_s = 0.794$ S/m) yield the complex permittivity shown in Fig. 2.3. The data in Fig. 2.3 suggests that the contrast between normal adipose-dominated tissue and malignant tissue is ranging from a minimum of 6:1 to a maximum of 8:1, depending on the frequency of interest. The difference of the dielectric constant enables for waves at microwave frequencies to reconstruct

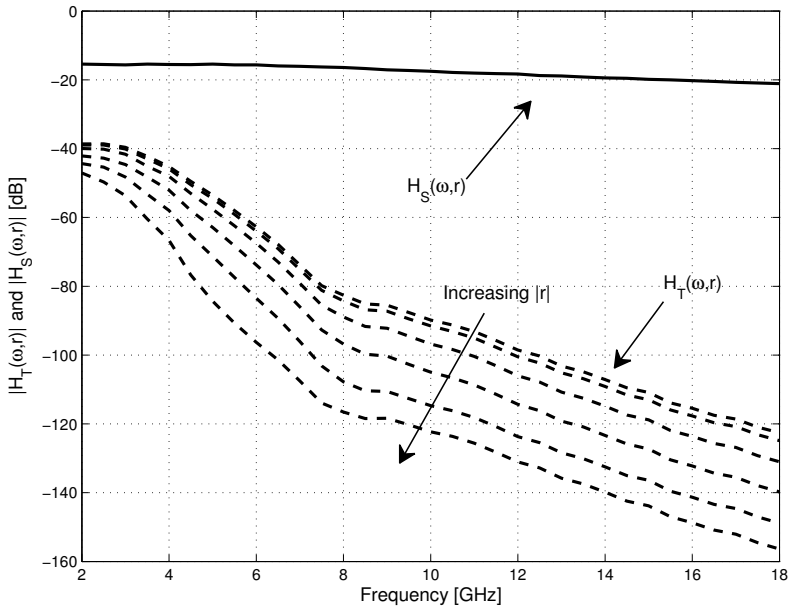


Figure 2.4: Antenna-skin-antenna $H_S(\omega,\vec{r})$ and antenna-tumor-antenna $H_T(\omega,\vec{r})$ path attenuation for $|\vec{r}|$ ranging from 4 cm to 11 cm.

the tumor image with respect to the adipose-dominated tissue around it.

### 2.3.2 Electro-Magnetic Simulations

Electro-magnetic simulations are performed on the numerical breast phantom with the finite-difference time-domain (FDTD) method using Meep, a freely available software package [46]. A monostatic approach is followed, where each antenna in the array sequentially transmits the signal and records the backscatter from the breast model. The EM signal used in the Meep FDTD simulations is a tone generated by a continuous-wave source applied to a isotropic cylindrical antenna with infinite length in the direction perpendicular the plane of Fig. 2.2. The frequency is varied as

$$f_k = f_{\min} + k\Delta f, \quad k = 0,1,\ldots 160 \tag{2.2}$$

By leveraging the linearity of the medium, the setup in Fig. 2.2 is varied as antenna in the air only and setup with and without tumor. This allows to discriminate between forward and reverse waves as well as reflection due to the air-skin interface and that due to the presence of the tumor. Simulations are performed for different relative positions of the tumor and antenna, i.e. different $\vec{r}$. The electric field at the input of the antenna is recorded and the results of the simulations are recast in the form of transfer functions of the paths antenna-skin-antenna $H_S(\omega,\vec{r})$ and antenna-tumor-antenna $H_T(\omega,\vec{r})$. Based on the set of the performed EM simulations, any configuration of the antenna array and tumor position can be reproduced. Once the number of antennas, the antenna-to-antenna distance and tumor positions are set, $H_T(\omega,\vec{r})$ and $H_S(\omega,\vec{r})$ are associated to each antenna based on the required distance $\vec{r}$. As an example, the attenuation experienced by the transmitted signal through the two paths is shown in Fig. 2.4 for a set of $|\vec{r}|$ ranging from 4 cm to 11 cm. Clearly, the radiation bouncing from the skin experiences little attenuation and dispersion, while this is not the case for the tumor response. A first important result is thus that the skin reflection dominates the tumor response. Comparing $|H_S(\omega,\vec{r})|$ and $|H_T(\omega,\vec{r})|$ one can

see that the receiver has to be able to process signals with a large difference in amplitude. The dynamic range may be in excess of 100 dB, depending on the transmitted frequency, suggesting that the ADC resolution has to be in the range of 15 to 18 bits. Another result is that any TX/RX interface that would be used must feature an isolation exceeding the attenuation experienced by the transmitted signal in the antenna-skin-antenna path, which is less than 20 dB. Many commercial devices achieve such a performance, e.g. [47].

### 2.3.3 Receiver Behavioral Model

The developed behavioral model of the receiver is more easily discussed with reference to the super heterodyne architecture. For each frequency step of the measurement scan and for each antenna, the transmitted tone

$$s_{\mathrm{TX,k}}(t) = A_{\mathrm{TX}} \cos(\omega_k t) \tag{2.3}$$

is irradiated through the antenna, where $A_{\mathrm{TX}}$ is the signal amplitude and $\omega_k = 2\pi f_k$ the transmitted frequency. The signal is scattered by both the skin and the tumor back to the receiver, where the superposition of the two effects results in the received signal

$$\begin{aligned} s_{\mathrm{RX,k}}(t) = & A_{\mathrm{TX}} |H_S(\omega_k, \vec{r})| \cos(\omega_k t + \angle H_S(\omega_k, \vec{r})) \\ & + A_{\mathrm{TX}} |H_T(\omega_k, \vec{r})| \cos(\omega_k t + \angle H_T(\omega_k, \vec{r})). \end{aligned} \tag{2.4}$$

The two-step quadrature downconversion shown in Fig. 2.1(b) can be modeled by complex multiplication of the received signal by the complex signals representing the two LOs:

$$s_{\mathrm{LO1}}(t) = \cos(\omega_1 t + \psi_1) - j \sin(\omega_1 t + \psi_2) \tag{2.5}$$

$$s_{\mathrm{LO2}}(t) = \cos(\omega_2 t + \phi_1) - j \sin(\omega_2 t + \phi_2) \tag{2.6}$$

where $\psi_1$ and $\psi_2$ (or $\phi_1$ and $\phi_2$) take into account the phase inaccuracies of the in-phase and quadrature components. $\psi_1$ and $\psi_2$ (or $\phi_1$ and $\phi_2$) can be decomposed in terms of common-mode and differential-mode components: $\psi_{\mathrm{CM}} = (\psi_1 + \psi_2)/2$ and $\psi_{\mathrm{DM}} = \psi_1 - \psi_2$ (and similarly for $\phi_{\mathrm{CM}}$ and $\phi_{\mathrm{DM}}$). As shown in Fig. 2.5(a), the common-mode phase error does not impair the accuracy of the quadrature, but it accounts for a rotation of the LO signals with respect to $s_{\mathrm{TX,k}}$. Therefore, it represents the phase error between the transmitted signal at the antenna and the LO at the mixer port. Such an error may arise from any difference in the two signal paths, or from the lack of precise phase coherence among the LOs, in the case of the super heterodyne architecture (see Fig. 2.1). The common-mode phase error also includes the effect of the phase noise, as it is assumed that the quadrature LO signals are derived from the same source by frequency division or by using a multi-phase oscillator.

On the other hand, the differential-mode phase error quantifies the quadrature error between the I and Q components of the LO, as depicted in Fig. 2.5(b), resulting in a limited image rejection in the receiver. Both $\psi_{\mathrm{CM}}$ and $\psi_{\mathrm{DM}}$ (or $\phi_{\mathrm{CM}}$ and $\phi_{\mathrm{DM}}$) may vary with the frequency of operation $\omega_k$. Therefore, they are modeled as random variables. The common-mode phase error $\psi_{\mathrm{CM}}$ is

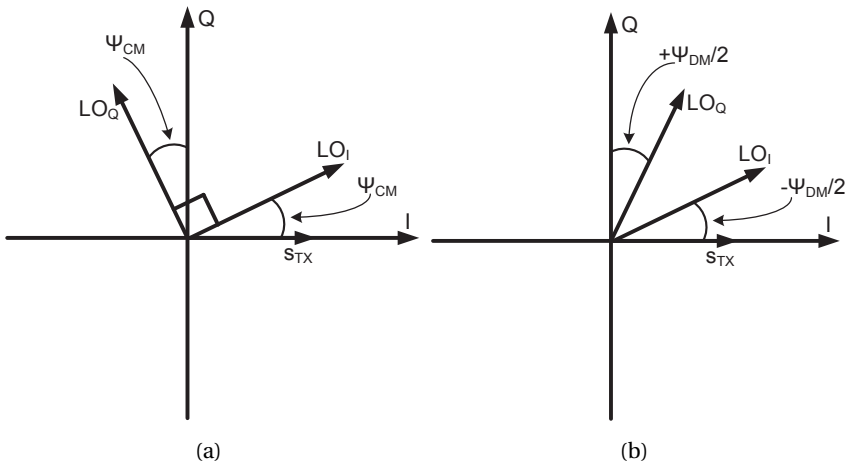


Figure 2.5: Phase inaccuracies of quadrature LO signals: (a) common-mode phase error and (b) differential-mode phase error.

made of a static part ($\Psi_{\mathrm{CM}}$) and the phase noise

$$\Delta\psi = \psi_{\mathrm{CM}}(t) - \psi_{\mathrm{CM}}(t-\tau_{T,k}), \tag{2.7}$$

where $\tau_{T,k} = -\angle H_T(\omega_k,\vec{r})/\omega_k$ is the round trip time delay of the path antenna-tumor-antenna. On the other hand, the common-mode phase error $\phi_{\mathrm{CM}}$ is made of a static part only, because the phase noise of $s_{\mathrm{LO2}}(t)$ is assumed negligible. Note that since the I/Q components are generated from the same oscillator, the phase noise appears as a common-mode phase error. The static components of the phase errors are modeled as gaussian random variables with variance $\sigma^2_{\psi_{\mathrm{CM}}}$ and $\sigma^2_{\psi_{\mathrm{DM}}}$ (or $\sigma^2_{\phi_{\mathrm{CM}}}$ and $\sigma^2_{\phi_{\mathrm{DM}}}$), respectively. The cumulative phase noise $\Delta\psi$ is modeled as a gaussian stochastic process with a variance that can be written as [26]:

$$\sigma^2_{\Delta\psi} = 2B_{\mathrm{filter}}\tau^2_{T,k}(2\pi f_{\mathrm{off}})^2\mathscr{L}(f_{\mathrm{off}}), \tag{2.8}$$

where $\mathscr{L}(f_{\mathrm{off}})$ is the LO phase noise at the frequency offset $f_{\mathrm{off}}$, and $B_{\mathrm{filter}}$ is the bandwidth of the baseband filter. The phase noise of the second LO is neglected as it operates at much lower frequencies.

As previously pointed out, the downconversion can be modeled as a multiplication of $s_{\mathrm{RF,k}}(t)$ by the complex local oscillator signals $s_{\mathrm{LO1}}(t)$ and $s_{\mathrm{LO2}}(t)$. We assume now that $\omega_1 \gg \omega_2$, and, without loss of generality, that $\omega_{\mathrm{RX,k}} > \omega_1 > \omega_2$ and $\omega_{\mathrm{RX,k}} - \omega_1 > \omega_2$, such that the desired intermediate frequency is $\omega_{\mathrm{IF2}} = \omega_{\mathrm{RX,k}} - \omega_1 - \omega_2$ and $\omega_{\mathrm{IF1}} = \omega_{\mathrm{RX,k}} - \omega_1$. The IF signal can be written as:

$$\begin{aligned} s_{\mathrm{IF,k}}(t) = \sum_{i=S,T}\Bigg\{ & \frac{A_{\mathrm{TX}}|H_i(\omega_k,\vec{r})|}{2}e^{-j\omega_k\tau_{i,k}}\Bigg[e^{j\omega_{IF2}t}e^{-j\theta_{\mathrm{CM,S}}}\cos\left(\frac{\psi_{\mathrm{DM}}}{2}\right)\cos\left(\frac{\phi_{\mathrm{DM}}}{2}\right) \\ & + je^{j\omega_{IM1}t}e^{-j\theta_{\mathrm{CM,D}}}\cos\left(\frac{\psi_{\mathrm{DM}}}{2}\right)\sin\left(\frac{\phi_{\mathrm{DM}}}{2}\right) \\ & + je^{j2\omega_k\tau_{i,k}}e^{j\omega_{IM2}t}e^{j\theta_{\mathrm{CM,D}}}\sin\left(\frac{\psi_{\mathrm{DM}}}{2}\right)\cos\left(\frac{\phi_{\mathrm{DM}}}{2}\right) \\ & - e^{j2\omega_k\tau_{i,k}}e^{-j\omega_{IF2}t}e^{j\theta_{\mathrm{CM,S}}}\sin\left(\frac{\psi_{\mathrm{DM}}}{2}\right)\sin\left(\frac{\phi_{\mathrm{DM}}}{2}\right)\Bigg]\Bigg\}, \end{aligned} \tag{2.9}$$

where $\theta_{\mathrm{CM,S}} = \psi_{\mathrm{CM}} + \phi_{\mathrm{CM}}$ and $\theta_{\mathrm{CM,D}} = \psi_{\mathrm{CM}} - \phi_{\mathrm{CM}}$ are the sum and difference of the common-mode phase error while $\omega_{IM1} = \omega_{\mathrm{RX,k}} - \omega_1 + \omega_2$ and $\omega_{IM2} = -\omega_{\mathrm{RX,k}} + \omega_1 - \omega_2$ correspond to the frequency at which the images at frequency $\omega_{\mathrm{RX,k}} - 2\omega_2$ and $-\omega_{\mathrm{RX,k}} + 2\omega_1$ are downconverted, respectively. Further, low-pass filtering is performed on the output (second) IF signal with a pass-band lower than the first IF, i.e. $\omega_{\mathrm{IF1}} = \omega_{\mathrm{RX,k}} - \omega_1$. In this case, the IF signal is written as:

$$\begin{aligned} s_{\mathrm{IF,k}}(t) = \sum_{i=S,T} \Bigg\{ \frac{A_{\mathrm{TX}}|H_i(\omega_k,\vec{r})|}{2} e^{-j\omega_k\tau_{i,k}} \Bigg[ e^{j\omega_{\mathrm{IF2}}t} e^{-j\theta_{\mathrm{CM,S}}} \cos\left(\frac{\psi_{\mathrm{DM}}}{2}\right)\cos\left(\frac{\phi_{\mathrm{DM}}}{2}\right) \\ - e^{j2\omega_k\tau_{i,k}} e^{-j\omega_{\mathrm{IF2}}t} e^{j\theta_{\mathrm{CM,S}}} \sin\left(\frac{\psi_{\mathrm{DM}}}{2}\right)\sin\left(\frac{\phi_{\mathrm{DM}}}{2}\right) \Bigg] \Bigg\}. \end{aligned} \tag{2.10}$$

At this point, it would still be possible to get rid of the second term in (2.10) (the image signal) by means of a complex filter, yielding, in this case

$$s_{\mathrm{IF,k}} \cong \sum_{i=S,T} \left[ \frac{A_{\mathrm{TX}}|H_i(\omega_k,\vec{r})|}{2} e^{-j\omega_k\tau_{i,k}} e^{-j[\Psi_{\mathrm{CM}}+\Delta\psi+\phi_{\mathrm{CM}}]} \cos\left(\frac{\psi_{\mathrm{DM}}}{2}\right)\cos\left(\frac{\phi_{\mathrm{DM}}}{2}\right) \right] \tag{2.11}$$

where $\tau_{S,k}$, similarly to $\tau_{T,k}$, is the round trip time delay associated to the skin, calculated as $\tau_{S,k} = -\angle H_S(\omega_k,\vec{r})/\omega_k$.

In the case of the direct conversion, we only have one LO, set at $\omega_k$ and the signal downconverted to baseband becomes

$$s_{\mathrm{IF,k}} = \sum_{i=S,T} \left\{ \frac{A_{\mathrm{TX}}|H_i(\omega_k,\vec{r})|}{2} e^{-j\omega_k\tau_{k,i}} \left[ e^{-j[\Psi_{\mathrm{CM}}+\Delta\psi]} \cos\left(\frac{\psi_{\mathrm{DM}}}{2}\right) + j e^{j2\omega_k\tau_i} e^{j[\Psi_{\mathrm{CM}}+\Delta\psi]} \sin\left(\frac{\psi_{\mathrm{DM}}}{2}\right) \right] \right\}. \tag{2.12}$$

The non-linearities of the receiver are modeled with a power series approach:

$$s_{\mathrm{BB,k}} = G_1 \cdot |s_{\mathrm{IF,k}}| e^{j\angle s_{\mathrm{IF,k}}} + G_2 \cdot |s_{\mathrm{IF,k}}|^2 (1+j) + G_3 \cdot |s_{\mathrm{IF,k}}|^3 e^{j\angle s_{\mathrm{IF,k}}} \tag{2.13}$$

where $G_1$ is the linear conversion gain of the receiver, $G_2$ is the coefficient of the second-order non-linear term and it is related to $IIP_2$, and $G_3$, the coefficient of the third-order non-linear term, models the gain compression [48, 49]. Furthermore, the amplitude of $s_{\mathrm{BB,k}}$ is hard limited to accommodate the operation beyond the 1 dB compression point. Note that in the super heterodyne case $G_2 = 0$.

The thermal noise of the receiver is modeled as gaussian additive noise, specified by the receiver noise figure, which is added to $s_{\mathrm{BB,k}}$. The operation of the ADC is taken into account by quantizing $s_{\mathrm{BB,k}}$ (plus noise) before the imaging processing is performed:

$$\hat{s}_{\mathrm{BB,k}} = [s_{\mathrm{BB,k}} + n_k]_q \tag{2.14}$$

where $\hat{s}_{\mathrm{BB,k}}$ is the quantized signal, $n_k$ is the noise sample, and $[\cdot]_q$ is the quantization operation.

### 2.3.4 Image Reconstruction Procedure

Once the array of $N$ antennas and the tumor position are established, the signal output by the receiver connected to each antenna, $\hat{s}_{\mathrm{BB,k}}$, is calculated as described in Sec. 2.3.3. Consequently,

a set of $N$ signals carrying information in the frequency-domain is available. By taking the inverse Fourier transform (IFFT) of $\hat{s}_{\mathrm{BB,k}}$, time-domain waveforms are generated:

$$\hat{s}_{\mathrm{BB,k}} \xrightarrow{\mathscr{F}^{-1}} p(kT_S, \vec{r}) \tag{2.15}$$

where $T_S = 1/(2f_{\max})$. At this point, the obtained time-domain waveforms include both the skin and tumor backscatters. The early-time content is dominated by the reflection from the skin, whereas the late-time content contains the tumor backscatter and clutter signals, as shown in Figs. 2.6(a) and 2.6(b). Since the skin response has much greater amplitude than the tumor response, as shown in Fig. 2.4, we need to remove the early-time content without corrupting the late-time content. A calibration signal is generated for each antenna by averaging the time response of every other antenna. The signal is then subtracted from the corresponding antenna as in [35]. Since the skin response embedded in the early-time content is almost the same for each antenna, the calibration removes the skin reflection and enhances the tumor response, as shown in Fig. 2.6(b). However, it is clear that this calibration procedure is effective as long as each antenna has the same distance from the skin. If this is not the case, more sophisticated algorithms can be employed to estimate the correct distance and efficiently remove the skin content [7].

At this point, $N$ time-domain waveforms containing only the tumor (plus clutter) response are available. The image creation is based on a simple delay-multiply-and-sum algorithm [12]. It consists on calculating, for each pixel, its intensity. First, the round trip time from each antenna to the considered pixel is calculated. In this calculation, the wave velocities of the different covered mediums (air, skin, healthy breast tissue) are taken into account. Then, the time-domain signals are time-shifted by an amount corresponding to the calculated round-trip times. In this way, the information on the considered pixel embedded in the various time-domain signals is aligned in time to the point $kT_S = 0$. Next, all the possible cross products between the time-shifted waveforms are evaluated, and summed together to obtain the signal $i_{x,y}(kT_S)$. Finally, the intensity $I$ of the pixel of coordinates $(x, y)$ is calculated as

$$I(x,y) = \left( T_S \sum_{k=-w/2}^{w/2} i_{x,y}(kT_S) \right)^2 \tag{2.16}$$

where $wT_S$ is approximately equal to the duration of the expected tumor response.

## 2.4 Impact of the Impairments

The developed behavioral model allows to evaluate the performance of the system for different values of the circuit level impairments. Transmission power, receiver conversion gain, $\mathrm{IIP}_2$, 1 dB compression point, noise figure, baseband filter bandwidth, ADC resolution, variance of the phase errors, as well as the variance of the cumulative phase noise are varied and their impact on the time domain signals processed by the receivers is carefully investigated. We consider the scenario depicted in Fig. 2.2, where the tumor is located 3 cm in depth, since it is the most important test case reported in the medical literature [29, 30]. Insights on the most critical circuit level impairments are given and specifications for the IC design are derived based on the application requirements.

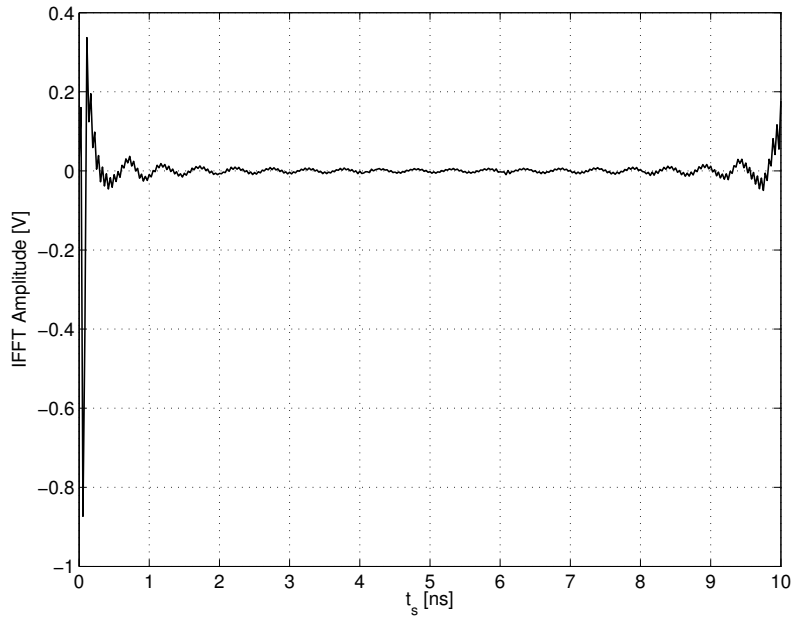


(a)

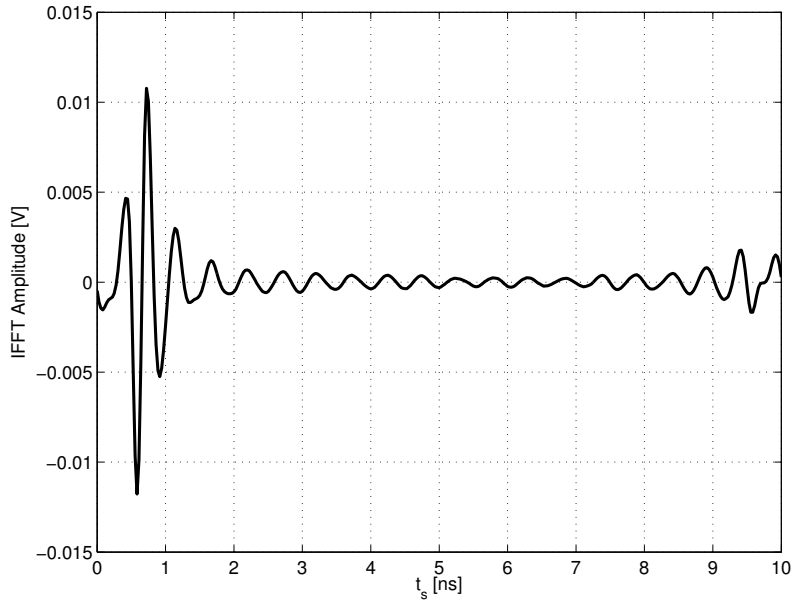


(b)

Figure 2.6: The result of a successful removal of the early-time skin content for the central antenna of the array with a tumor 3 cm in depth. (a) the signal before calibration. (b) the signal after calibration.

### 2.4.1 Gain

Gain flatness specifies how much the receiver conversion gain varies over the specified frequency range. Variations in the gain can cause distortion on the waveforms processed by the system. Despite the high resolution needed by this application, the system shows a good robustness toward ripples in the gain. As we will show in Section 2.5, a peak-to-peak ripple level of 3 dB does not impair the ability of the system to properly detect and enhance the tumor response while introducing a negligible level of degradation on the image quality.

Process spread during the realization of the antennas and the integrated circuits generate gain mismatches among different transceivers that can impair the ability of the system to correctly enhance the tumor response. In fact, if the skin content is not correctly estimated by the calibration algorithm, the residual spurious signal can severely deteriorate the tumor response. In this scenario, complex algorithms can be employed to efficiently estimate and remove the skin content [7]. Alternatively, a single transceiver can be mechanically moved over all the synthetic aperture length of the antenna connected to a single antenna or to an antenna pair for TX and RX. Moreover, calibration can be performed to characterize the gain of the single transceivers. The latter can limit the negative effects of ripples and gain mismatches on the enhancing of the tumor response.

### 2.4.2 Noise

The impact of noise on the image quality is assessed by evaluating the amplitude of the time domain signals $p(kT_S, \vec{r})$ processed by the receivers. Fig. 2.7 shows the IFFT amplitude considering -15 dBm transmitted power, 40 dB conversion gain, 10 dB receiver noise figure, 100 kHz baseband filter bandwidth, $IIP_2 = 20$ dBm, -30 dBm 1dB compression point, 18-bit ADCs. Flicker noise, phase noise and phase inaccuracies have been neglected so far, hence direct conversion and super heterodyne yield the same result. The results reported in Fig. 2.7 show the IFFT amplitude of the received backscatterers from the skin and tumor together. The amplitude of the target-only processed signal lies 60 dB above the noise floor. This gives important insights into the circuit design of the integrated transceiver. Despite the heavy attenuation experimented by the signal in the antenna-tumor-antenna path at higher frequencies (see Fig. 2.4), the receiver is robust towards thermal noise, even if the noise figure is not very low, and even if the transmitted power is moderate. This is due to the SFCW approach, that allows for narrow baseband bandwidths, while preserving synthetic UWB performance at radio frequencies, i.e. high resolution. Moreover, the inherent processing gain of the inverse Fourier transform process allows for enhancing the target response with respect to the receiver noise.

The possibility of relaxing the noise figure specification is favorable especially to the direct conversion approach. In this case, the downconverted spectrum extends to DC and the flicker noise gives a non negligible contribution to the overall system noise. Due to the SFCW approach, a sample of the flicker noise is taken at each frequency step $f_k$ of the measurement, as explained in Sec. 2.3.2. The folding process inherent in the sampling operation flattens the flicker PSD, resulting in a broadband white noise contribution [50]. As such, the immediate effect is to increase the white noise floor depicted in Fig. 2.7. Autozeroing techniques and chopper stabilization can be exploited to mitigate the flicker noise effects. If autozeroing is employed, the low-frequency 1/f noise can be high-pass filtered and thus strongly reduced at the cost of an increased noise floor due to aliasing of the white noise. Chopper stabilization upconverts the frequency range

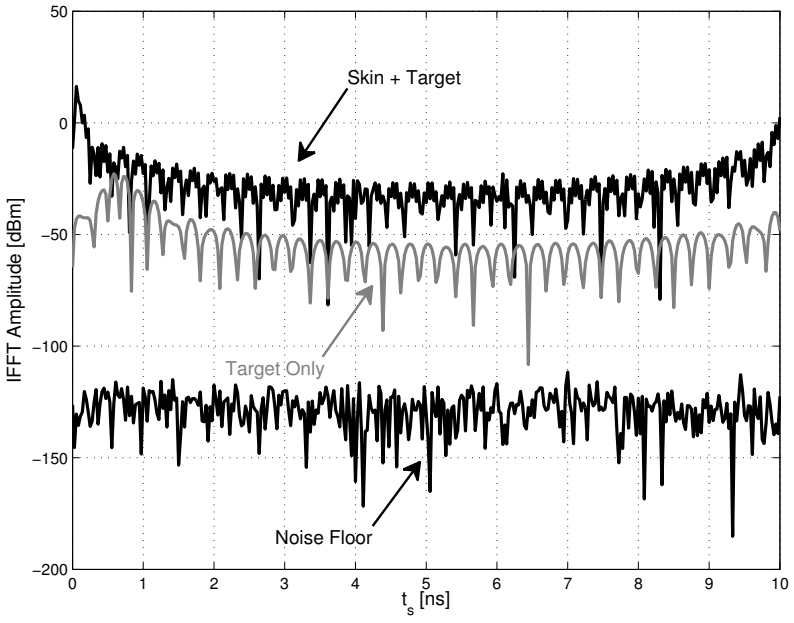


Figure 2.7: IFFT amplitude of skin-and-target, target-only received signals with respect to the noise floor at the output of the receiver. The plot refers to the central antenna of the setup in Fig. 2.2 with the tumor 3cm in depth.

of the input signal to the chopping frequency, where 1/f noise is lower than thermal noise, and then demodulates it back to baseband. Both these techniques allow to decrease the flicker noise PSD to a nearly constant value that tends to the input white noise, reducing its additional power contribution to a negligible level [50].

### 2.4.3 Non-linearities

The non-linear behavior of the receiver is modeled as described in (2.13) to take into account for the high dynamic range required by the system. As previously explained in Section 2.3.3, breast cancer imaging is realistically assumed to be performed in a screened environment, where the interferers' contribution is negligible. Since the spurious reflection due to the skin is much larger than the desired signal, it excites the non linearities the most. For this reason, in both super heterodyne and direct conversion, the 1dB compression point is kept well above the maximum signal level due to the skin reflection. With a transmitted power of -15 dBm, the highest signal level processed by the system is around -33 dBm and the 1dB compression point specification is set to -30 dBm. As counterintuitive as it may sound, the direct conversion receiver appears to be quite immune to second-order nonlinearities. To this regard, the RMS error between the time domain signal $p(kT_S, \vec{r})$ processed by the receiver before and after calibration and the same signals in absence of second order distortion (i.e. $IIP_2 = \infty$) is simulated as a function of $IIP_2$. The RMS error is normalized to half-LSB of a 18-bit ADC with 2V input range. As shown in Fig. 2.8, the error after calibration is at least one order of magnitude less than the error before calibration and its contribution is less than half-LSB for values of $IIP_2$ larger than 10 dBm. That is, since most of the second-order distortion is due to the skin reflection, it results common to all the received signals at the antennas of the array and it is effectively removed by the calibration algorithm.

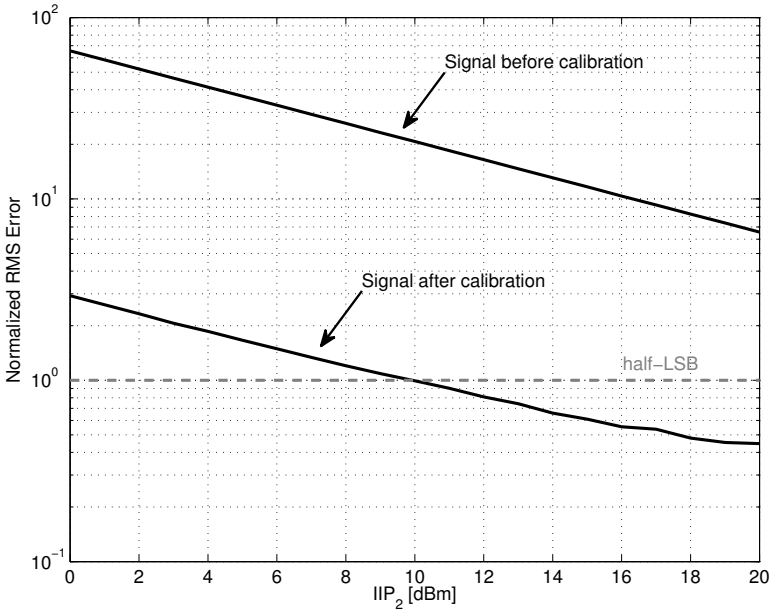


Figure 2.8: Normalized RMS error of the time domain signal $p(kT_S, \vec{r})$ before and after calibration as a function of the $IIP_2$ relative to the same signal in absence of second order distortion. The RMS error is normalized to half-LSB of a 18-bit ADC with 2V input range. The plot refers to the central antenna of the setup in Fig. 2.2 with the tumor 3cm in depth.

### 2.4.4 Phase Noise and I/Q Phase Mismatches

A coherent system, in which the phase of the transmitted signal relative to the receiver LOs is well known, is necessary to recover the difference in phase of the received backscatter relative to the transmitted signal and compute the range-delay of the target. For this reason, the I/Q phase mismatches are critical in receivers designed for this application. It is useful to get more insight on their impact on the received time-domain waveforms $p(kT_S, \vec{r})$.

The received signal $s_{\mathrm{IF,k}}$ consists on the sum of two terms: the first is related to the tumor response while the second one to the skin spurious backscatterer. In fact, if no phase inaccuracies are taken into account, (2.11) and (2.12) become

$$s_{\mathrm{IF,k}} = \frac{A_{\mathrm{TX}}}{2}\left[|H_{S,k}|e^{-j\omega_k\tau_{S,k}} + |H_{T,k}|e^{-j\omega_k\tau_{T,k}}\right], \tag{2.17}$$

showing that the tumor response is dictated by the term $|H_{T,k}|$ while the skin by $|H_{S,k}|$, that is at least 20 dB greater in magnitude, as suggested by Fig. 2.4. The distortion introduced on the received signal $s_{\mathrm{IF,k}}$ by phase inaccuracies is weighted by $|H_{T,k}|$ and $|H_{S,k}|$ as well. The net result is that, from the received signal $s_{\mathrm{IF,k}}$ point of view, the distortion introduced by the skin term is much larger compared to the target one. Hence, through the action of the spurious skin backscatterer, even a small distortion generated by I/Q phase inaccuracies and/or phase noise couples into the signal processed by the receiver. Since the set of phase inaccuracies is different for each receiver connected to the antennas, the skin content response is different as well. The calibration signal generated by averaging the contribution of each antenna results noisy and uncorrelated to the actual skin content, adversely affecting the ability of the system to enhance the tumor response during the calibration procedure. Let's now investigate the impact of common-mode, $\psi_{\mathrm{CM}}$, and differential-mode, $\psi_{\mathrm{DM}}$, mismatches as static errors (i.e.

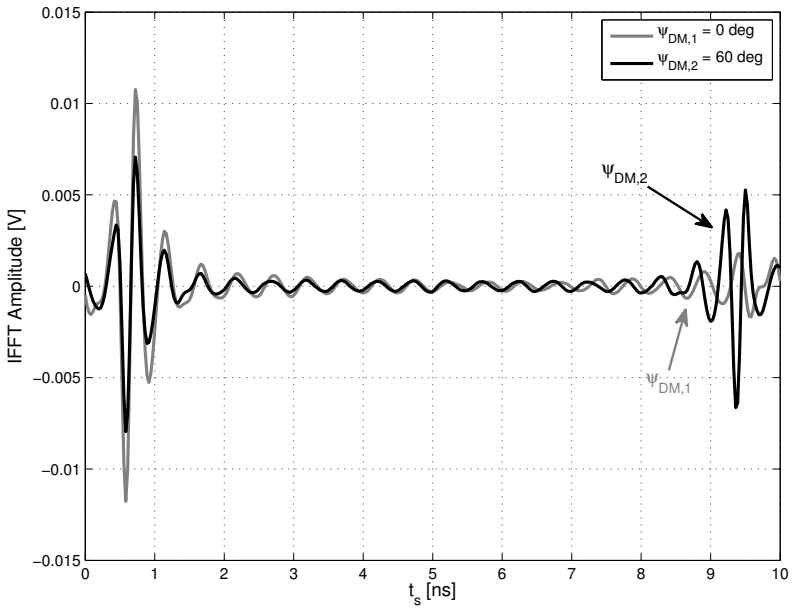


(a)

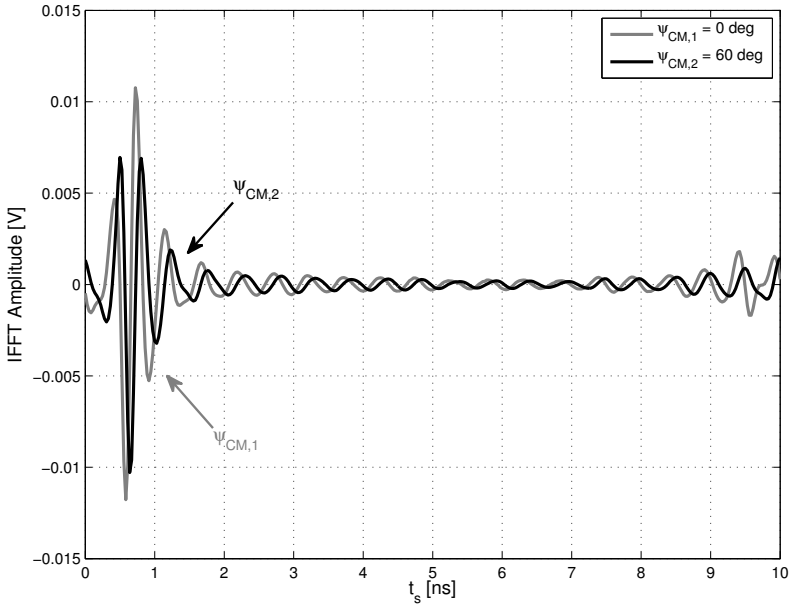


(b)

Figure 2.9: Amplitude of $p(kT_S, \vec{r})$ after calibration in presence of phase mismatches modeled as static errors: (a) differential-mode mismatches, (b) common-mode mismatches. Plots refer to the central antenna of the setup in Fig. 2.2 with the tumor 3 cm in depth.

their values are set and do not depend on frequency) on the received time-domain waveforms $p(kT_S, \vec{r})$ after calibration. To this end, we consider a one-step downconversion and very high level of phase inaccuracies, to better appreciate the results from a qualitative point of view. The situation is depicted in Fig. 2.9. For the differential-mode mismatches, the relative power of the second term in (2.12) increases with $\psi_{DM}$. While the true tumor response decreases, a ghost image of the tumor is folded at $\tau_T$ from the maximum unambiguous range of the radar, as shown in Fig. 2.9(a). However, the presence of a ghost tumor image is not a problem since the information carried in the (very) late-time response is not useful for the localization of tumors in normal-dimension breasts. Additionally, the tumor signal phase is hard-shifted by a term proportional to $\psi_{\mathrm{DM}}$, yielding a constant error in the evaluation of the tumor position. This second effect is experienced in presence of common-mode mismatches, too. In this case, the phase is shifted by a term proportional to $\psi_{\mathrm{CM}}$ that leads to a larger fixed error in the evaluation of the tumor position, as shown in Fig. 2.9(b). It is clear that mismatches due to a static errors are not critical for the tumor detection, although leading to errors in the evaluation of the correct tumor position.

In general, due to the frequency dependent nature of device mismatches and the way I/Q components are generated by integrated frequency synthesizers, common-mode and differential-mode phase mismatches are expected to be frequency dependent. To properly capture this effect, $\psi_{\mathrm{CM}}$ and $\psi_{\mathrm{DM}}$ are modeled as gaussian variables with zero mean and variance $\sigma^2_{\psi_{\mathrm{CM}}}$ and $\sigma^2_{\psi_{\mathrm{DM}}}$, respectively. The tumor response undergoes a decrease in amplitude while the clutter level increases elsewhere, as illustrated in Fig. 2.10, where the value of the variance of the common-mode phase mismatch is set large to underline this effect. If differential-mode instead of common-mode phase mismatches were considered, waveforms similar to the one in Fig. 2.10 would be obtained from the simulation. To better understand the strong impact of random errors even for small variance values, the RMS error of the time domain signal $p(kT_S, \vec{r})$ after calibration relative to the same signal in absence of any mismatch was calculated as a function of the standard deviation $\sigma_{\psi_{\mathrm{DM}}}$ and $\sigma_{\psi_{\mathrm{CM}}}$. Fig. 2.11 shows the RMS error normalized to half-LSB of a 18-bit ADC with 2V input range. Even for small values of $\sigma_{\psi_{\mathrm{CM}}}$ (or $\sigma_{\psi_{\mathrm{DM}}}$), the RMS error quickly reaches values comparable to half-LSB. Moreover, the error generated by common-mode mismatches grows twice as fast as the one given by the differential-mode mismatches. Since the clutter is close to the tumor response and comparable in magnitude, a serious reduction in the ability of the system to detect and locate the tumor is experienced. In addition to the random I/Q phase mismatches, the phase noise has to be considered. As shown by (2.11) and (2.12), the effect of the phase noise is the same of the common-mode phase mismatches and the variance of the cumulative phase noise can be calculated using (2.8). As such, the considerations made for the common-mode phase mismatches directly apply to the phase noise case as well.

To summarize, frequency-independent phase errors are not critical for the tumor detection. They lead to errors in the evaluation of the tumor position but not in its size and detection. The ghost tumor image is not a problem since the information carried in the late-time response is not useful for the image reconstruction. On the other hand, frequency dependent phase mismatches and phase noise are critical even for small variance values. They enhance the clutter level with respect to the tumor response, leading to a possible failure in the detection of the tumor. Therefore, particular attention has to be taken in the IC design, where the standard deviation of the common-mode and differential-mode mismatches has to be kept well below 1.5°, as suggested by Fig. 2.11.

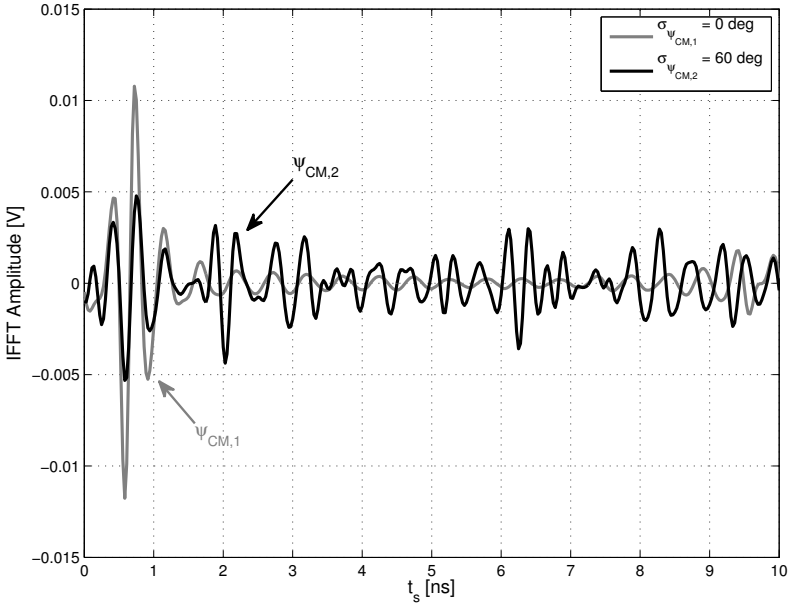


Figure 2.10: Amplitude of $p(kT_S, \vec{r})$ after calibration in presence of common-mode phase mismatch modeled as a gaussian variables with variance $\sigma^2_{\psi_{\mathrm{CM}}}$. The plot refers to the central antenna of the setup in Fig. 2.2 with the tumor 3 cm in depth.

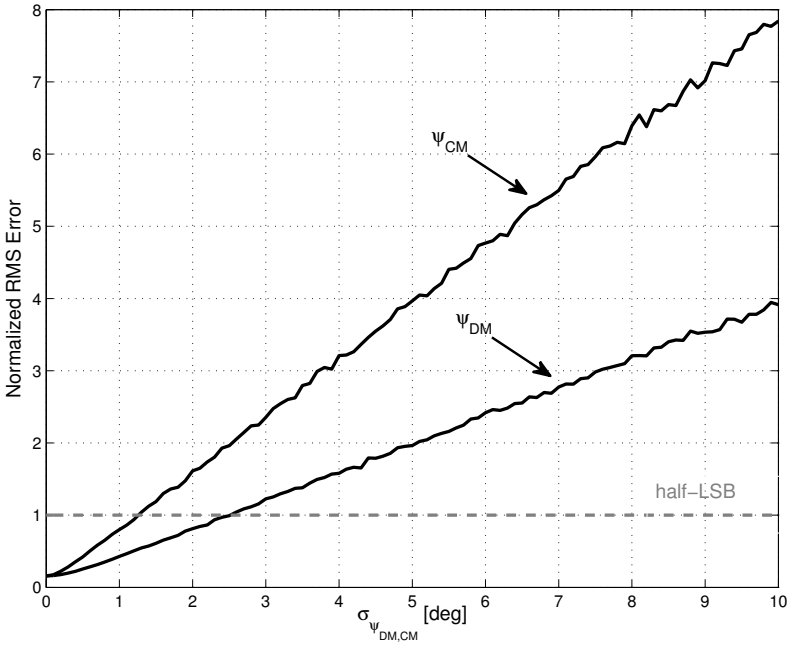


Figure 2.11: Normalized RMS error of the time domain signal $p(kT_S, \vec{r})$ after calibration relative to the same signal in absence of any mismatch as a function of the standard deviation $\sigma_{\psi_{\mathrm{DM}}}$ and $\sigma_{\psi_{\mathrm{CM}}}$: (a) differential-mode phase mismatch, (b) common-mode phase mismatch. The RMS error is normalized to half-LSB of a 18-bit ADC with 2 V input range. The plot refers to the central antenna of the setup in Fig. 2.2 with the tumor 3 cm in depth.

Table 2.1: Receiver Specifications

| | |
|---|---|
| Bandwidth | 2-18 GHz |
| Frequency Step | 100 MHz |
| TX Power | -15 dBm |
| Conversion Gain | 40dB |
| Noise Figure | 10 dB |
| Baseband Filter Bandwidth | 100 kHz |
| $IIP_2$ | 20 dBm |
| 1dB Compression Point | -30 dBm |
| $\sigma_{\psi_{CM}}=\sigma_{\phi_{CM}}=\sigma_{\psi_{DM}}=\sigma_{\phi_{DM}}$ | $\leq 1.5^\circ$ |
| $\mathscr{L}(f_{off})$ | -110 dBc/Hz at $f_{off}$ = 1 MHz |
| ADC resolution | 18-bit |
| ADC input range | 2 V |

### 2.4.5 Receiver Specifications

Based on the impact of the most important circuit-level impairments, we delineate the specifications for the design of the integrated transceiver, summarized in Tab. 2.1. The receiver operation was seen to be robust towards the thermal noise, thus allowing to relax the noise figure requirement to 10 dB. The 1 dB compression point has to be kept at a level of at least -30 dBm to accommodate for the large in-band interferer backscattered from the skin. The $IIP_2$ is set to 20 dBm, to limit the contribution of its RMS error to less than half-LSB, as shown in Fig. 2.8. Frequency dependent phase mismatches where shown to be critical. As such, the standard deviation of the common-mode and differential-mode phase errors is limited to $\sigma_{\psi_{CM}}=\sigma_{\phi_{CM}}=\sigma_{\psi_{DM}}=\sigma_{\phi_{DM}} \leq 1.5^\circ$, as suggested by Fig. 2.11. A value of $\mathscr{L}(f_{off})$ =-110 dBc/Hz at a frequency offset $f_{off}$=1 MHz together with a baseband filter bandwidth of 100 kHz yields a standard deviation of the cumulative phase noise of $\sigma_{\Delta\psi} \cong 0.3^\circ$ for the case of a tumor 4 cm in depth and the last antenna of the array, limiting the contribution of the phase noise to the common-mode phase mismatches.

The specifications summarized in Tab. 2.1 do not change if the tumor is located closer to the skin or deeper in the breast. The noise floor was shown to be well below the desired signal level, while the linearity requirements are set by the large skin reflection and not the tumor location itself. The tight specifications regarding the I/Q phase mismatches were derived based on the RMS error of the waves at the output of the receiver in presence and absence of phase mismatches, that does not depend on the tumor location as well.

If the distance $d_{AS}$ between the antenna array and the skin is changed, the antenna-skin-antenna and antenna-tumor-antenna transfer functions in Fig. 2.4 will both experience an equal rigid translation. This can be compensated by adjusting the transmitted power when designing the overall system.

## 2.5 Architecture Comparison

The direct conversion and super heterodyne receivers are compared by generating the tumor images in the two cases with the same set of circuit impairments. The quality of the generated

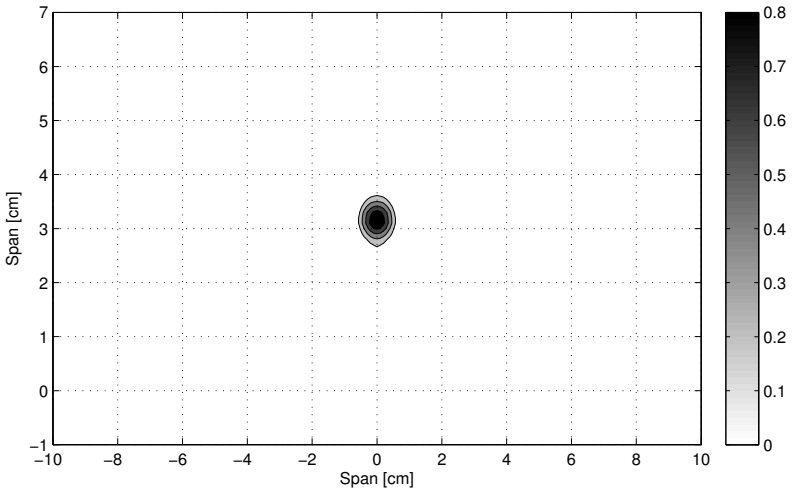


Figure 2.12: Reconstructed tumor image with an ideal receiver. In this image, 11 antenna spacing 2 cm from each other irradiate a tumor 3 cm in depth from the skin.

image is quantified by means of the signal-to-clutter ratio (SCR), defined as the average intensity of the image in the area where the target is located, divided by the average intensity of the image elsewhere

$$\mathrm{SCR} = \frac{\sum_{(x,y)\in A_T} I(x,y)/A_T}{\sum_{(x,y)\in A_T^C} I(x,y)/A_T^C}, \tag{2.18}$$

where $A_T$ is the area containing the target, and $A_T^C$ is the complementary area with respect to the region under consideration. The image of a 4 mm-diameter malignant tumor at 3 cm in depth from the skin obtained with an ideal receiver (no circuit impairments) is shown in Fig. 2.12; the corresponding SCR is 21.5 dB. It shows the quality of the employed imaging algorithm, and it represents the benchmark to assess the impact of all the circuit impairments. In this case, the direct conversion and super heterodyne architecture yield the same result. The two architectures are then compared by generating the images with the same set of impairments, based on the specifications derived in Sec. 2.4.5 and summarized in Tab. 2.1. Figure 2.13(a) shows the result in the direct conversion case considering -15 dBm transmitted power, 40 dB conversion gain, 3 dB gain ripple, 10 dB receiver noise figure, 100 kHz baseband filter bandwidth, $\mathrm{IIP}_2$ = 20 dBm, -30 dBm 1dB compression point, $\sigma_{\psi_{\mathrm{CM}}}$=$\sigma_{\phi_{\mathrm{CM}}}$=$\sigma_{\psi_{\mathrm{DM}}}$=$\sigma_{\phi_{\mathrm{DM}}}$=1.5°, 18-bit ADCs, and a phase noise level of $\mathscr{L}(f_{\mathrm{off}}) = -110$ dBc/Hz at $f_{\mathrm{off}}$ = 1 MHz, while Fig. 2.13(b) shows the super heterodyne case. The SCR reduces to 17.8 dB and 14.5 dB in the direct conversion and super heterodyne cases, respectively. Note that the gain ripple decreases the SCR by only 0.4 dB. As shown in Fig. 2.14, the system reliably detects the tumor even when it is located deeper in the breast or closer to the skin. The SCR decreases as the tumor is located farther from the antennas while the difference between the SCR experienced by the direct conversion and super heterodyne architectures remains within 2 to 3 dB. In Fig. 2.15, the tumor images were generated for different values of the antenna-to-antenna distance $d_{\mathrm{AA}}$ over the same synthetic aperture length $l$. As the total number of antennas decreases to 8 and 5, the SCR decreases as well, as expected from the discussion in Section 2.3.1. The difference in performance between the two architectures does not change with the number of antennas.

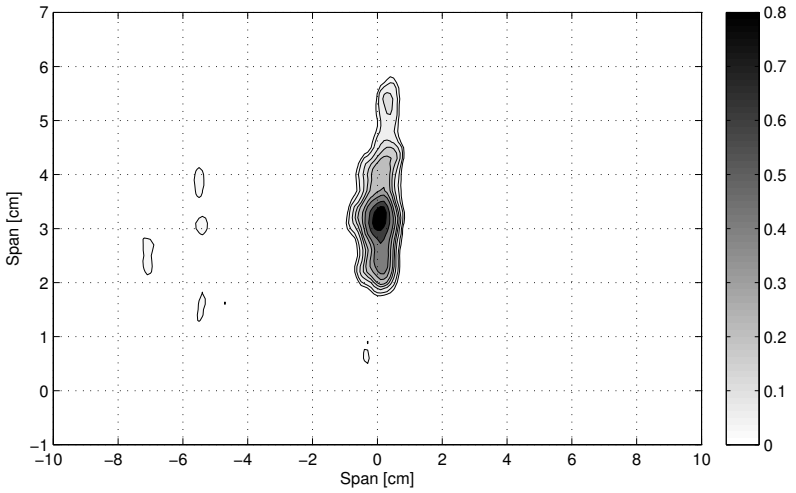


(a) Direct conversion

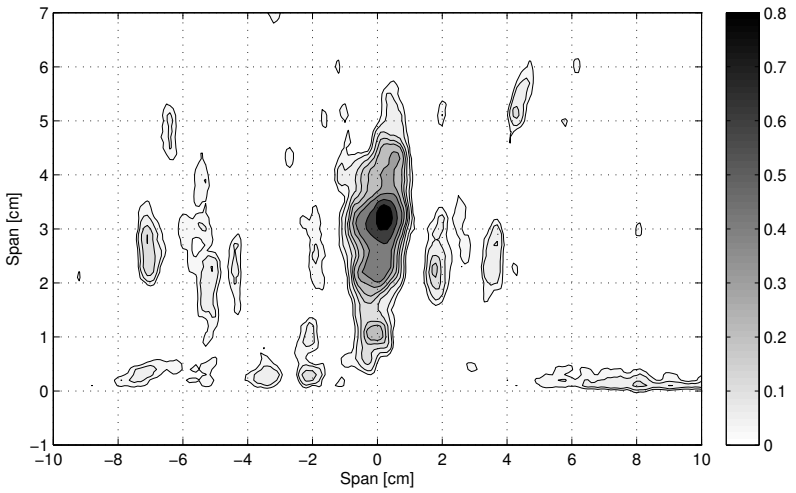


(b) Super heterodyne

Figure 2.13: Reconstructed tumor image with the two architectures and the same set of circuit impairments, summarized in Tab. 2.1.

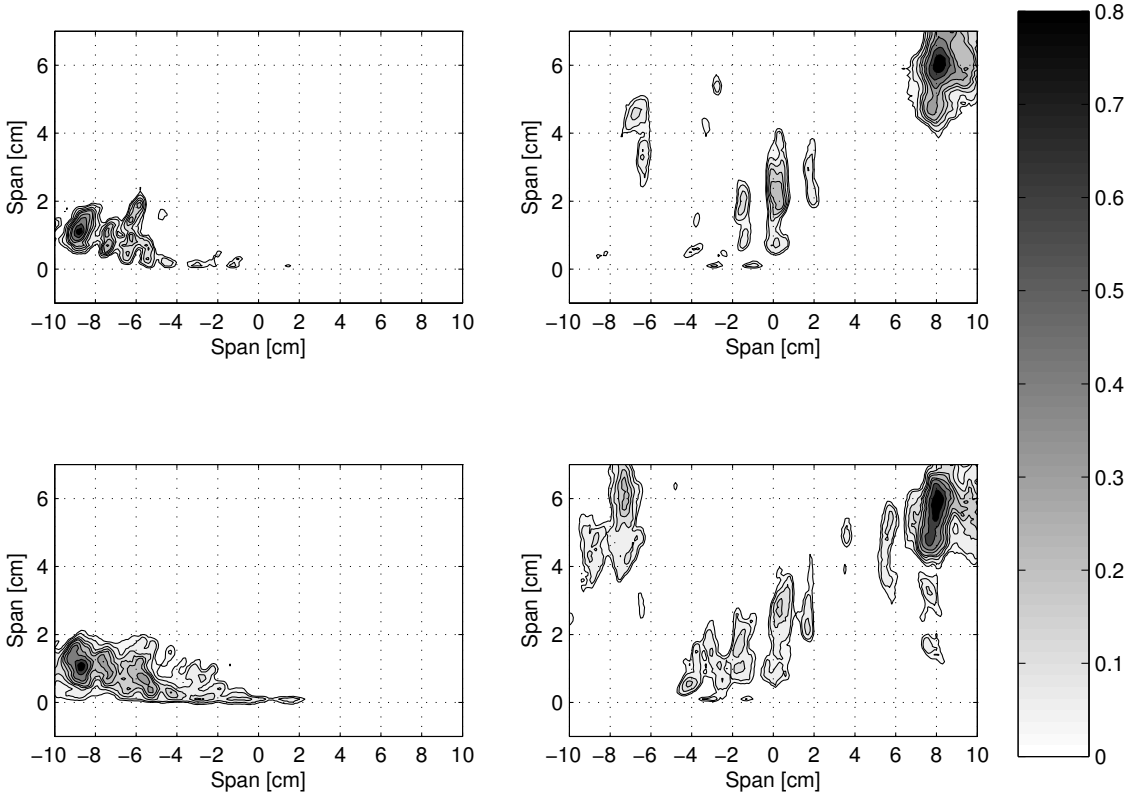


Figure 2.14: Reconstructed tumor image with the direct conversion (top) and super heterodyne (bottom) architectures for the same set of impairments summarized in Tab. 2.1 and different tumor positions. The SCR of the direct conversion is 18.1 dB and 8.9 dB for the tumor placed closer to the skin and deeper in the breast, respectively, while the SCR of the super heterodyne is 15.5 dB and 7.1 dB for the tumor placed closer to the skin and deeper in the breast, respectively.

As discussed in Sec. 2.4.4, the I/Q mismatches are critical to the operation of the receiver. In Fig. 2.16, the different impact of the common-mode and differential-mode impairments on both the architectures is shown. The common-mode mismatches, i.e. the random phase offsets between the TX and RX LOs, are clearly the most critical source of degradation of the image quality. In the super heterodyne architecture, the signal is degraded during both the two downconversion steps while in the direct conversion it undergoes a single step downconversion. To this regard, direct conversion inherently behaves better. On the other hand, super heterodyne shows a good insensitivity to increments of differential-mode mismatches. Since the developed super heterodyne model assumes interferers screening is possible in the application environment, no spectral content is downconverted from the image frequencies at $\omega_k - 2\omega_2$ and $-\omega_k + 2\omega_1$ to baseband, as explained in the Section 2.3.3. Consequently, (2.11), unlike (2.12), does not contain any additional image term. However, if spectral leakage was experimented (e.g. from the skin reflection), terms at $\omega_k - 2\omega_2$, $-\omega_k + 2\omega_1$ and $2\omega_1 + 2\omega_2 - \omega_k$ would grow and super heterodyne would experiment a SCR reduction similar to the direct conversion. In Fig. 2.17, the SCR is reported as a function of $\sigma_{\psi_{\mathrm{CM}}}$=$\sigma_{\phi_{\mathrm{CM}}}$ for $\sigma_{\psi_{\mathrm{DM}}}$=$\sigma_{\phi_{\mathrm{DM}}}$=0° and $\sigma_{\psi_{\mathrm{DM}}}$=$\sigma_{\phi_{\mathrm{DM}}}$=1.5° for both the receiver architectures. As previously explained, the two SCR curves for $\sigma_{\psi_{\mathrm{DM}}}$=$\sigma_{\phi_{\mathrm{DM}}}$=0° and $\sigma_{\psi_{\mathrm{DM}}}$=$\sigma_{\phi_{\mathrm{DM}}}$=1.5° overlap almost entirely in the super heterodyne case, showing a good insensitivity to increments of the differential-mode mismatches. However, when both the actions of differential-mode and common-mode mismatches are considered, the direct conversion architecture seems to be preferable, thanks to its single step downconversion. On the other hand,

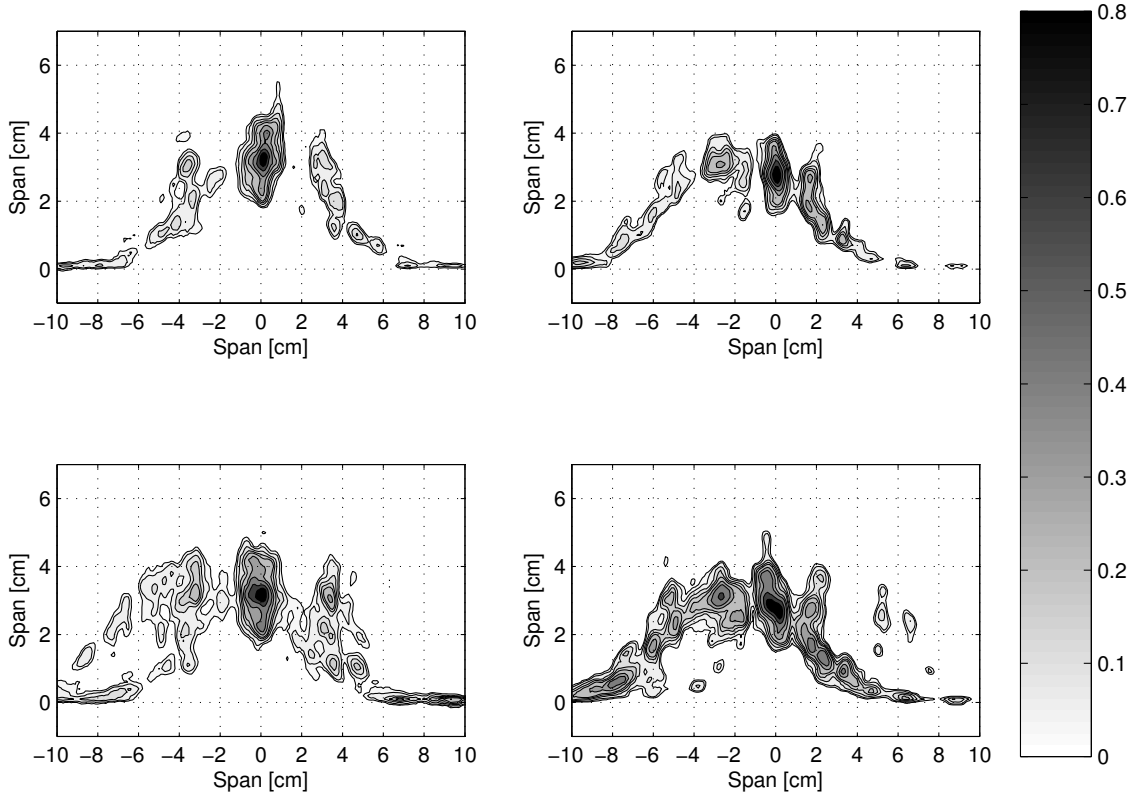


Figure 2.15: Reconstructed tumor image with the direct conversion (top) and super heterodyne (bottom) architectures for the same set of impairments summarized in Tab. 2.1 with 8 (left column) and 5 (right column) antennas covering the same synthetic aperture length $l = 20$ cm. The SCR of the direct conversion is 12.8 dB and 9.2 dB for 8 and 5 antennas, respectively, while the SCR of the super heterodyne is 10.3 dB and 7.4 dB for 8 and 5 antennas, respectively.

if bigger devices are employed in the second downconversion step, a lower level of impairments can be considered for the second LO of the super heterodyne architecture. In the case where half the impairments are supposed for the second LO (i.e. $\sigma_{\phi_{\mathrm{CM}}}$=$\sigma_{\psi_{\mathrm{CM}}}/2$ and $\sigma_{\phi_{\mathrm{DM}}}$=$\sigma_{\psi_{\mathrm{DM}}}/2$), the super heterodyne and the direct conversion architectures show a comparable performance, as shown in Fig. 2.17. By further decreasing $\sigma_{\phi_{\mathrm{CM}}}$ and $\sigma_{\phi_{\mathrm{DM}}}$, the super heterodyne architecture becomes progressively comparable to the direct conversion, as predicted by (2.11) and (2.12). Nevertheless, the requirement of phase coherence among the LOs in the super heterodyne architecture implies a more complex implementation making the direct conversion preferable. Due to the high resolution required by the application (i.e. large bandwidth), a small random phase mismatch dramatically enhances the clutter level and decreases the tumor response amplitude. That is, in a high resolution phase-detection system, random phase offsets between TX and RX LOs are extremely critical and clearly do not enable a correct recovery of the phase difference between irradiated and backscattered signal, leading to errors in the evaluation of the tumor location and detection. From this point of view, direct conversion seems preferable and enjoys a much simpler architecture. In the super heterodyne architecture, I/Q mismatches requirements can be relaxed in the second downconversion step by using bigger devices. However, both the LOs have to be coherent (i.e. their phase relative to the TX signal has to be known), which does not lend itself to easy practical solutions. On the other hand, the same LO can be used to irradiate the breast and downconvert the received backscatterer in the direct conversion architecture. The reduction of the dynamic range due to LO leakage, DC offset voltage and low

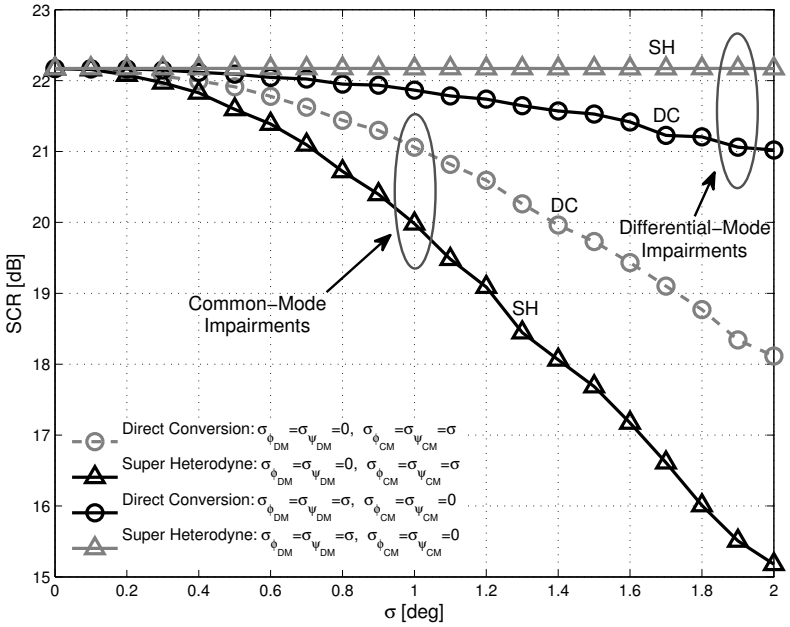


Figure 2.16: Impact of the differential-mode and common-mode mismatches on the SCR for super heterodyne and direct conversion architectures.

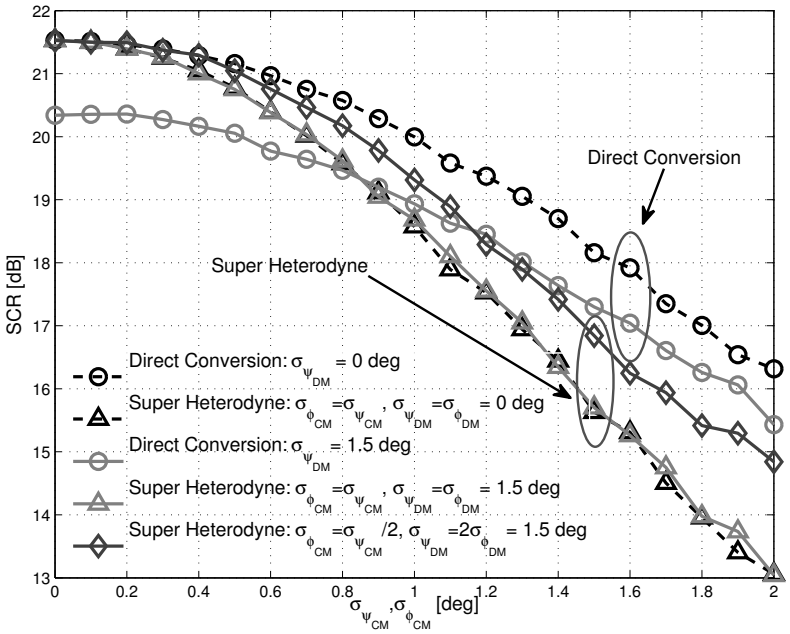


Figure 2.17: SCR for super heterodyne and direct conversion architectures for different levels of I/Q phase imbalance.

frequency $1/f$ noise may be critical in the direct conversion operation. The amplitude of the induced errors has to be kept below half-LSB of the baseband ADC. Adding auto-calibration requires additional hardware and software implementation, complicating the IC design. Auto-zero amplifiers achieve typical input offset of $1\mu V$ with a temperature-related drift of $20nV/C°$, satisfying the requirements of this application to deal with small signals. On the other hand, chopper stabilization technique upconverts $1/f$ noise to the chopping frequency, resulting in a nearly constant baseband noise [50]. Both the techniques can be applied together to satisfy the application requirements. To address the wide tuning range specifications, a PLL can be used to generate the frequencies from 9 to 18 GHz while synthesizing the two lower octaves by means frequency dividers [51]. A possible efficient implementation of the dividers is as injection locked frequency dividers (ILFD) [52, 53]. The low phase noise level of -110 dBc/Hz at $f_{\text{off}}$ = 1 MHz can be achieved by employing a dual-band VCO working in the band from 9 to 18 GHz [54, 55], or covering the band with multiple VCOs. The design of a wideband LNA in the range from 2 to 18 GHz is challenging. A multi section reactive network can be designed to resonate the input impedance over a wide bandwidth to achieve input matching and good noise performances [56]. Alternatively, a common-gate stage together with a noise-canceling architecture can be used to decouple the noise figure from the matching requirement without the need of a global negative feedback [57]. On the other hand, shunt-shunt resistive feedback can enable the design of very compact broadband inductorless LNAs [58]. Finally, careful design techniques have to be used to minimize the coupling of the transmitted signal at the antenna to the LNA input port while preserving the I/Q phase mismatches required level.

## 2.6 Conclusions

Super heterodyne and direct conversion architectures for a SFCW breast cancer detection radar system are compared. Both the architectures exhibit a comparable performance, as shown in Fig. 2.17. However, a marginally higher robustness to phase inaccuracies makes the direct conversion perform slightly better in terms of signal-to-clutter ratio, as reported in Fig. 2.13(a) and 2.13(b). $IIP_2$ issues are shown to be solvable by subtracting the calibration signal from each antenna and widely known solutions allow to properly deal with $1/f$ noise and DC offset issues inherent the direct conversion architecture. Most importantly, super heterodyne complexity does not allow an easy solution to the TX/RX coherence, critical requirement in a high-resolution phase-detection system. This complexity is also likely to result in higher power consumption to achieve the same set of specifications, further emphasizing a preference for the direct conversion solution.

# Circuit Design Part II

# 3 Radar Front-end Architecture

In Chapter 2, a through analysis has been carried out to delineate the circuit-level requirements for the integrated radar transceiver front-end for breast cancer imaging. In this chapter, further insight is given into the mapping of the derived circuit-level constraints into a suitable and effective architecture. The front-end transceiver architecture is then presented from a high-level point of view, along with the steps required to effectively develop the chip in CMOS technology.

## 3.1 Constraints Mapping

In Chapter 2, a realistic numerical breast phantom model was used to derive the circuit-level requirements for the integrated imaging radar. In the numerical breast phantom, the transmitting antenna is supposed to be placed in air at 1 cm distance from the breast skin, and that no coupling media is used, as shown in Fig. 3.1(a). As illustrated in Chapter 2, a monostatic configuration (transmitting and receiving antennas are co-located) is considered for simplicity. The simulated round-trip attenuation of a signal in the antenna-skin-antenna path ($H_S(f)$) is shown in Fig. 3.1(b) as a function of frequency in the wide range from 2 to 18 GHz. Little dispersion is observed, and $|H_S(f)| \approx -20$ dB in the entire frequency range. The transfer function associated to the antenna-tumor-antenna path, $H_T(f)$, is also simulated for various values of the relative distance of the tumor and the antenna from 4 to 11 cm (c.f. Section 2.3.2). The result is also shown in Fig. 3.1(b): the echo due to the 4 mm-diameter tumor target is much smaller than the echo due to the skin, with a relative attenuation that strongly increases with frequency. From the transceiver point of view, the hardware must be capable of simultaneously processing both the large backscatter due to the skin and the weaker backscatter due to the tumor. Hence, a dynamic range in excess of 100 dB is required. As a consequence, an analog-to-digital converter (ADC) with a resolution in excess of 16 bit is needed in the system. An ADC featuring high resolution does not display a high Nyquist frequency. This means that the radar analog front-end must adopt a direct-conversion or a low-IF architecture. A direct-conversion architecture simplifies the frequency generation, and has been thus chosen in the presented integrated radar. With the same motivation, a single conversion architecture is used, despite using multiple frequency conversion steps would have also been a possible option. One of the advantages of using the SFCW approach is that the system noise bandwidth can be as narrow as desired; this is totally compatible with the use of a high resolution ADC with limited band.

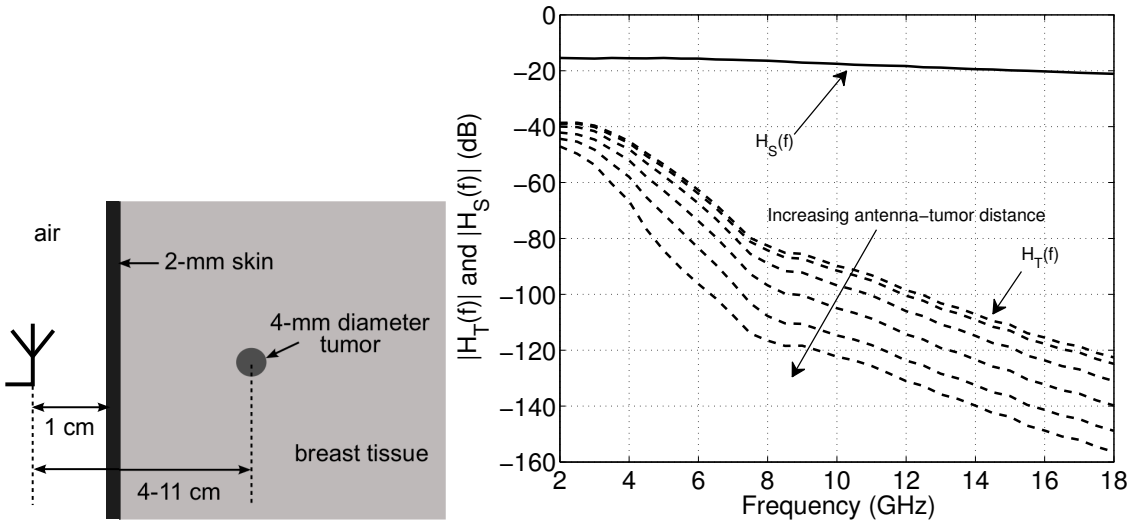


(a) (b)

Figure 3.1: (a) Realistic numerical breast phantom to perform finite-difference time-domain (FDTD) electro-magnetic simulations. (b) The antenna-skin-antenna ($H_S$) and antenna-tumor-antenna ($H_T$) attenuation experienced by a signal radiated by an antenna placed at 1 cm from the skin with a tumor at distances ranging from 4 to 11 cm.

By transmitting -14 dBm, the maximum received input signal is dictated by the skin reflection, and it is thus around -34 dBm. Consequently, the receiver compression point is specified to be higher than -30 dBm. To guarantee a dynamic range in excess of 100 dB with a noise bandwidth of 1 kHz, the receiver must feature a noise figure lower than 10 dB. Notice, however, the strong dispersion shown by $H_T(f)$: the request for a dynamic range in excess of 100 dB only applies to the higher frequencies. Once the synthetic time-domain pulse is recovered by means of IFFT, the signal-to-clutter ratio will be larger because of the higher energy of the tumor scatter at lower frequencies while the receiver noise figure is relatively constant over the band. Moreover, the IFFT operation yields an additional intrinsic processing gain roughly equal to the number of IFFT data points that is beneficial to improve the quality of the obtained image.

As emphasized in the foregoing discussion, the SFCW approach results in a system with peculiar features: the extremely wide bandwidth at RF calls for a broadband transmitter output stage, a broadband receiver low noise amplifier and mixer, along with a broadband local oscillator generation. At the same time, for each frequency step, the transmitted signal is a single tone, such that the receiver can feature a very narrow baseband bandwidth. In a direct conversion architecture, at the output of the receiver the desired signal for each frequency step reduces to a dc signal. As a consequence, the main drawbacks of a direct conversion architecture, namely DC offsets, 1/f noise and second-order distortion may be show-stoppers. In the proposed system, the dc offsets are calibrated out as discussed in Chapter 6, the impact of the 1/f noise is mitigated as described in Section 3.2, while the IIP2 is specified to be greater than 20 dBm, as detailed out in Chapter 2.

In a high resolution imaging system, random phase offsets between I and Q channel are extremely critical and lead to errors in the evaluation of the tumor location and detection. To this regard, the quadrature phase error for the local oscillator generation is specified to be less than

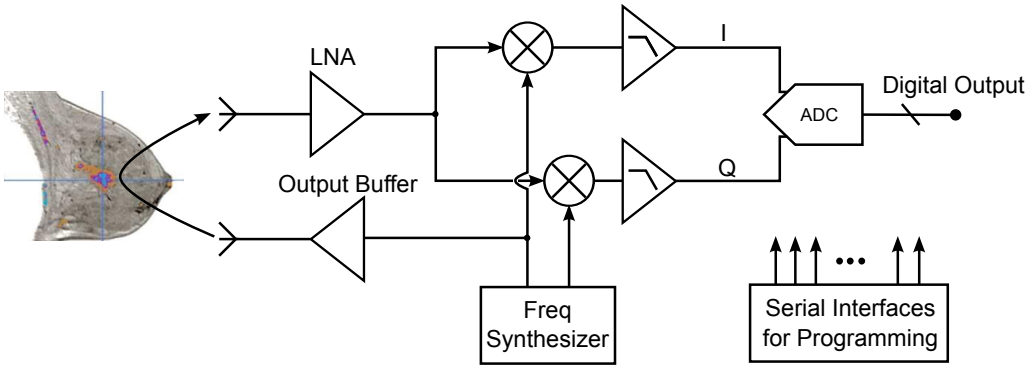


Figure 3.2: High-level block diagram of the proposed radar front-end transceiver for breast cancer diagnostic imaging.

1.5° over more than 3 octaves, as discussed in Chapter 2.

## 3.2 Front-end Transceiver Architecture

The high-level block diagram of the proposed architecture, comprising two wideband antennas, receiver, frequency synthesizer and output buffer is shown in Fig. 3.2. The primary advantage in selecting a SFCW radar approach over a traditional pulse-based UWB transceiver comes from the narrowband continuous wave (CW) nature of the transmitted and received signals. In fact, even if the electronics need to process signals over a wide band of frequencies, at any time only a CW signal passes through the system, which allows the selected frequency to be synthesized in a switched fashion. This is achieved by the frequency synthesizer, that operates over the frequency band from 1.75 to 16 GHz with an appropriate step, selected through the serial interfaces for programming. Accordingly, the receiver path can receive signals in the frequency band ranging from 1.75 to 16 GHz. The received signal, after a low noise amplification (LNA), experiences the frequency translation to DC, where it gets amplified by the baseband amplifier and digitized by the ADC. The mixers are driven by quadrature phases covering the 1.75 to 16 GHz bandwidth. A wideband output buffer irradiates the selected frequency and completes the block diagram.

A more detailed diagram of the implemented transceiver front-end is shown in Fig. 3.3. The receiver signal path is made of a wideband LNA, linearized transconductors, passive current-mode mixers and chopper-stabilized TIAs, that drive an external ADC. The LNA is a 3-stage design, based on the noise-canceling technique [59], and on shunt-peaked loads, to expand the bandwidth. Transconductors linearized by means of local resistive feedback feed passive current-mode mixers through ac-coupling capacitors. This arrangement maximizes the linearity while avoiding the downconverted signal to be corrupted by the 1/f noise of the mixer switches. Current-to-voltage conversion of the baseband quadrature signal is performed by trans-impedance amplifiers (TIAs). To cope with the 1/f noise of the transistors of the TIAs, the chopper stabilization technique is employed.

An accurate and precise frequency generation and distribution is a key challenge for this system. An integer-N PLL synthesizes all the frequencies from 7 to 16 GHz starting from a 22.6 MHz reference. The PLL relies on two VCOs not to impair the phase noise performance for the tuning range. Each VCO is followed by an injection-locked prescaler by 4. A programmable divider, PFD, charge pump and 3$^{rd}$ loop filter close the control loop. A reconfigurable injection-locked

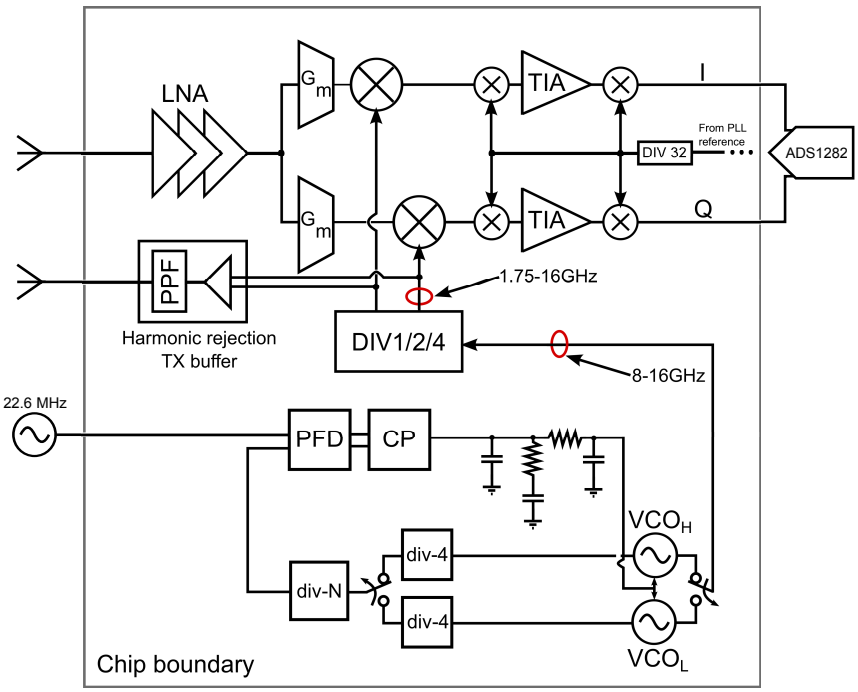


Figure 3.3: Block diagram of the implemented radar front-end transceiver for breast cancer diagnostic imaging.

divider by 1, 2 or 4 generates the quadrature phases over the entire 1.75-16 GHz range and drives the mixers. The divider is interfaced to the PLL and to the mixers by means of injection-locked regenerative buffers. Since both the regenerative buffers and the reconfigurable divider are based on injection-locking on ring oscillators, the obtained locking ranges are very wide [53], such that no calibration or tuning is required. Each injection-locking stage contributes to progressively improve the quadrature accuracy as discussed in [60]. The result is that this arrangement allows to keep the I/Q phase mismatches as low as 1.5°, as required for correct imaging operation.

The SFCW approach requires the transmitted signal to be coherent with the local oscillator. Hence, the signal is tapped at the mixer local oscillator port by a buffer and output to be irradiated. Since the local oscillator signal features a rich harmonic content (its waveform is approximately a square wave), some means of harmonic rejection is required. Implementing a harmonic rejection mixer in the receiver is not a feasible option due to the high frequencies involved. As a consequence, an asymmetric poly-phase filter (PPF) is used as a harmonic rejection filter in the transmitter, due to the different response it shows to the quadrature sequence associated to the first, and to the third harmonic. The quadrature sequence associated to the first harmonic goes through the filter with little attenuation, while the sequence associated to the third harmonic is notched out by the filter transmission zeros. At the output of the filter the quadrature signals are combined in the current domain. The result is that the first harmonic is reinforced, while the second is canceled. By combining the quadrature signals at the output of the PPF, second harmonic cancellation is obtained. The PPF embeds a switch that allows to turn the transmitter off. This feature is useful to perform loopback calibration of dc offsets, local oscillator feedthrough and transmitter-receiver leakage, as described in Section 6.4.1.

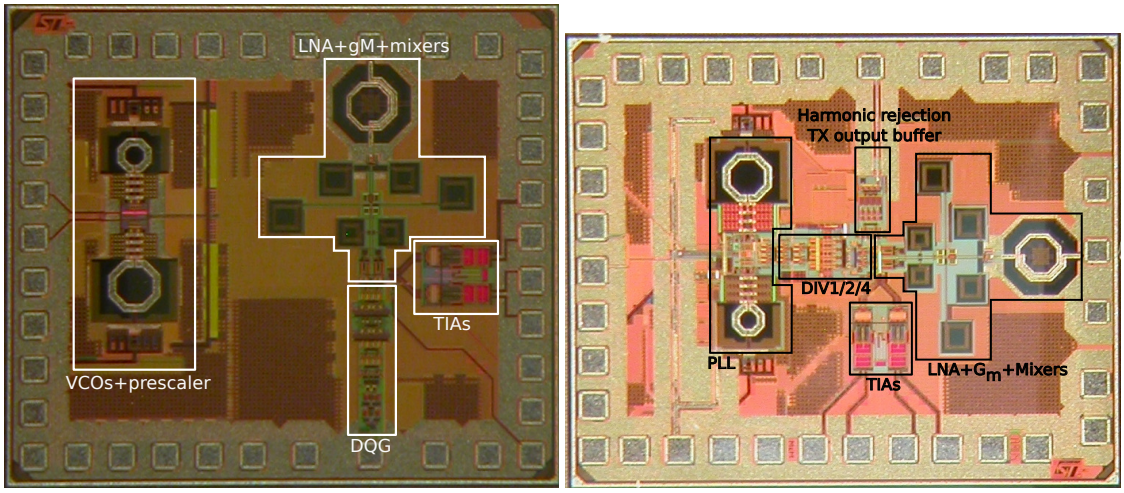


(a) (b)

Figure 3.4: (a) SKuRAD1. (b) SKuRAD2.

## 3.3 Targeting the Chip Design

Temperature and process variations have become key issues in the design of integrated circuits using deep submicron technologies. Modern CMOS manufacturing technologies show large process variations, especially for RF circuitry, in which the variability of transistors and passives has a significant impact on the final circuit behavior. The targeted microwave transceiver front-end for breast cancer imaging proposed in Fig. 3.3 was developed in a two-step design process. The 65 nm CMOS node was chosen for its widely proven reliability.

The first chip, named SKuRAD1 and shown in Fig. 3.4(a), comprises the whole receiver. It includes the wideband LNA, transconductors, mixers, chopper stabilized transimpedance amplifier and a first version of the reconfigurable injection-locked divider by 1, 2 or 4 that generates the quadrature phases for the mixers. In SKuRAD1, the LO driving the reconfigurable divider by 1, 2, or 4 is fed externally through a test buffer. Also, a first design of the two wideband VCOs, each followed by the the injection-locked prescaler by 4 and the programmable divider is included for testing purposes to correctly meet the desired frequency range. The author's main contributions include the design of the wideband LNA, the linearized transconductors and the mixers.

The second chip, named SKuRAD2 and shown in Fig. 3.4(b), is the whole transceiver-front end. In SKuRAD2, a new version of the programmable injection-locked divider by 1, 2 or 4 ensures a better reliability over a wider bandwidth than the one of SKuRAD1. The VCOs, injection-locked prescaler by 4 and the programmable divider are closed in a phase locked loop. The measurements of the SKuRAD1's VCOs were used to properly size the loop. An additional digital loop for coarse tuning was also designed to properly select the desired output frequency. The author contributed by designing the phase locked loop, along with a partial re-design of the VCOs and other minor adjustments on the receiver chain.

The design and measurements of the receiver, including the reconfigurable injection-locked divider by 1, 2 or 4 are presented in Chapter 4, whereas the design and measurements of the phase locked loop are illustrated in Chapter 5.

# 4 Receiver

In this chapter, a 65 nm CMOS receiver tailored for breast cancer diagnostic imaging is demonstrated. The receiver shows 31 dB conversion gain, NF<8.6 dB, $P_{1dB}$ >-28 dBm, IIP3>-12 dBm and IIP2>22 dBm over a band from 1.75 to 15 GHz. A programmable injection-locked divider generates quadrature LO signals with a I/Q phase error <1.5° over 3 octaves without requiring any calibration or tuning. The receiver shows a flicker noise corner as low as 40 Hz, achieving a dynamic range of 106 dB [61].

The chapter is organized as follows. In Section 4.1, the block diagram of the proposed receiver is presented along with the circuit-level design of its main building blocks. Section 4.2 includes the measurements results. Conclusions follow.

## 4.1 Circuit Design

A block diagram of the proposed receiver is shown in Fig. 4.1. The signal path is made of a wideband LNA, linearized transconductors, quadrature current-mode passive mixers, and baseband transimpedance amplifiers (TIAs). A programmable divider/quadrature generator (DQG) provides quadrature signals to the mixers over the entire 1.75 to 15 GHz frequency range out of a LO signal spanning the higher octave (i.e. 7 to 15 GHz).

Compared to wideband receivers for wireless communications, e.g. software-defined radios [62, 63] or WiMedia UWB systems [64, 65], the presented circuit addresses peculiar issues and design challenges. First, it features a bandwidth that is more than two times wider. Second, it requires an extremely high instantaneous dynamic range, because of the strong undesired skin backscatter, which is an in-band signal coexisting with the very weak tumor echo. Consequently, the dynamic range cannot be dealt with by varying the receiver gain, as usually done, for example, in cellular systems. Third, the quadrature accuracy is extremely important, as the imaging process is based on phase measurements. It is vital that the performance is consistent and homogeneous in the entire band without offsets or jumps in the quadrature error for different portions of the covered spectrum. Finally, the narrow baseband bandwidth allowed by the SFCW approach requires a very low flicker noise corner, while CMOS transistors notoriously feature large flicker noise.

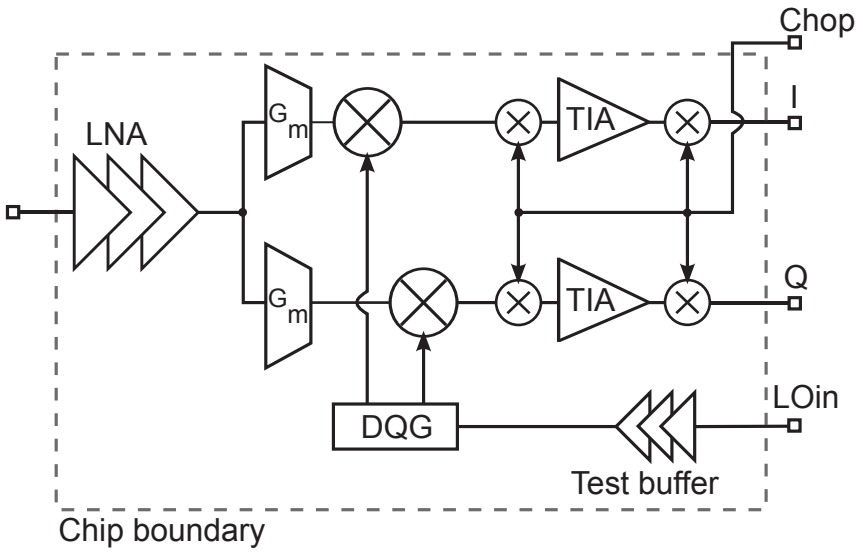


Figure 4.1: Block diagram of the proposed transceiver front-end.

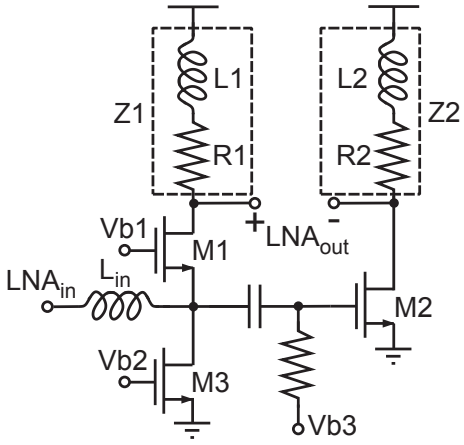


Figure 4.2: Schematic of the first stage of the LNA.

### 4.1.1 Low Noise Amplifier

The LNA must provide wideband input matching and gain, while featuring a low noise figure. To achieve the required performance from 1.75 to 15 GHz a three-stage design is used. The first stage is responsible for the input matching and the noise performance. A multi-section input matching network could have been used as in [56]. However, the combination of a wide fractional bandwidth and a relatively low frequency at the lower edge of the band calls for large inductors, that would be impractical. The employed topology is instead a common-gate/common-source noise canceling amplifier [57, 59], whose schematic is shown in Fig. 4.2. The noise canceling stage allows to decouple the matching requirement from the noise figure performance. The noise generated by the matching device $M_1$ is canceled without impairing the useful signal by setting $|Z_1|/|Z_2| = g_{m2}R_S$, where $R_S$ is the source resistance. The common-gate branch is biased with 2 mA, while the common-source branch is biased with 7 mA. The widths of transistors $M_1$ and $M_2$, both featuring minimum channel length, are 40 $\mu$m and 80 $\mu$m, respectively. Biasing transistor $M_3$ has a higher overdrive voltage ($W_3 = 10\,\mu$m, $L_3 = 0.12\,\mu$m) as compared to $M_2$ to decrease its noise contribution. The combination of the series inductor $L_{in} = 520$ pH and the common-gate stage $M_1$ results in good matching over a wide 1.5 to 20 GHz frequency range.

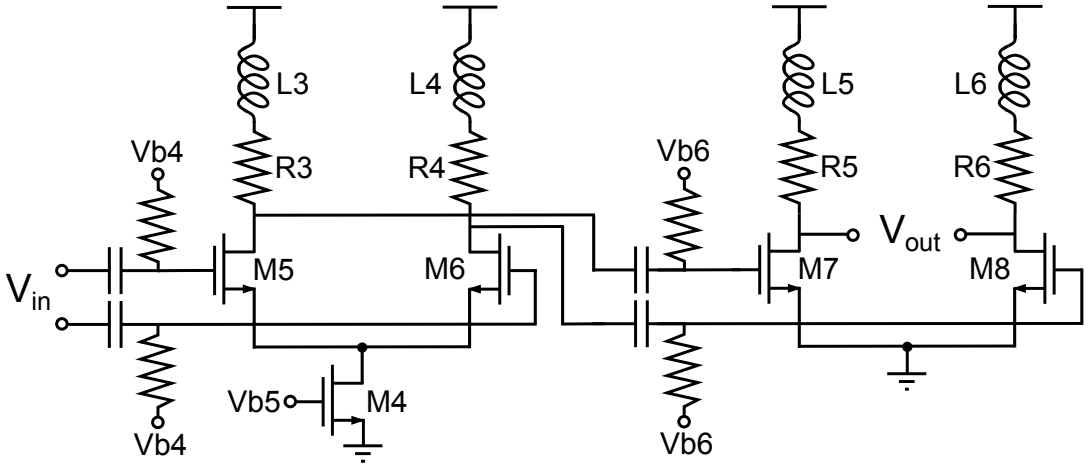


Figure 4.3: Schematic of the second and third stage of the LNA.

Table 4.1: Component values of the LNA shunt-peaked loads.

| | $L_1$ | $L_2$ | $L_3 = L_4$ | $L_5 = L_6$ |
|---|---|---|---|---|
| Inductance [pH] | 900 | 700 | 900 | 550 |
| Area [$\mu$m$^2$] | 56×56 | 50×50 | 56×56 | 42×42 |
| | $R_1$ | $R_2$ | $R_3 = R_4$ | $R_5 = R_6$ |
| Resistance [Ω] | 225 | 75 | 170 | 34 |

The schematic of the second and third stage of the LNA is shown in Fig. 4.3. The second stage of the LNA is biased with 6 mA. It is a fully differential pair to improve the signal balance and add gain. The third stage is biased with 12 mA. It is a pseudo-differential stage for better linearity.

All 3 stages use shunt-peaked loads to expand the bandwidth. The values of the load inductances and resistances are shown in Table 4.1. Since the loads are intrinsically low-$Q$, the inductors are stacked square coils, resulting in a very compact layout, that saves area and minimizes the coupling issues between the LNA stages. The resistance $R_2$ is implemented as a parallel combination of three resistances of value $R_1$ to guarantee good matching for the noise canceling condition, at least at the lower frequencies. The gains of the first and second stage are 13 dB and 7 dB, respectively. The third stage has a relatively low 2 dB gain at lower frequencies, that peaks to 8 dB at about 17 GHz. Such an arrangement is used to equalize the bandwidth roll-off due to the preceding stages, and to expand the overall bandwidth of the LNA. The designed amplifier features a bandwidth that is more than two times wider compared to state-of-the-art noise canceling LNAs, see e.g. [59].

### 4.1.2 Low 1/f Noise Corner Quadrature Downconverter

Resistively-degenerated transconductance ($G_m$) stages are used in the I/Q paths to convert the LNA output voltage into current, as shown in Fig. 4.4. Each $G_m$ stage is biased with 8 mA, and makes use of a $R_{deg} = 46\,\Omega$ degeneration resistor. Self-biased active loads are employed: this configuration avoids the need of an auxiliary common-mode feedback control loop.

Current-mode passive mixers are capacitively coupled to the transconductor outputs (cf. Fig. 4.4). This choice results in both good linearity and good noise performance, preventing the flicker noise of the commutating devices to corrupt the downconverted signal [66]. A large and constant

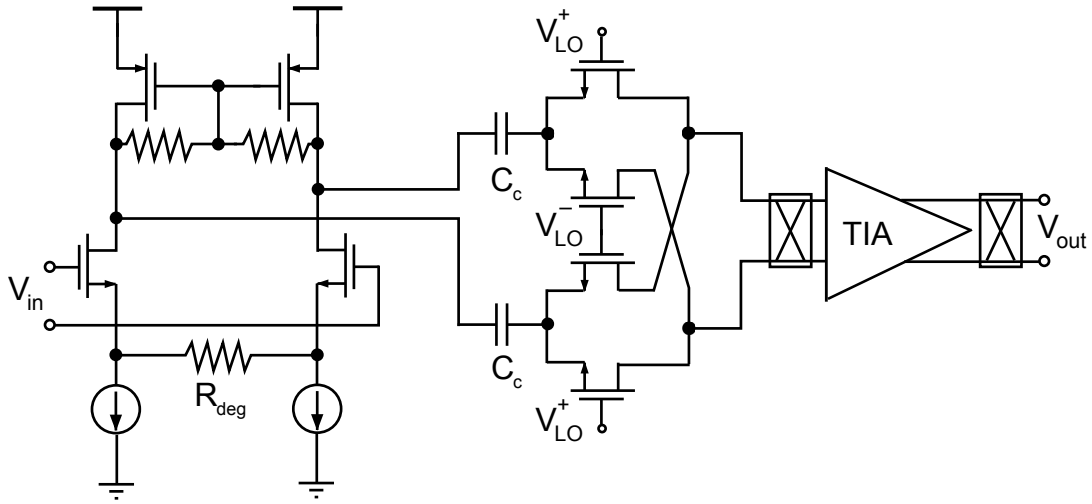


Figure 4.4: Schematic of the I-path downconverter (Q-path is identical).

swing of the LO signal across the band is essential to achieve good mixer performance. The proposed DQG plays a key role in this, as discussed in the following Section 4.1.3.

The use of passive mixers is not sufficient to address the high flicker noise of MOS transistors. Typically, current-mode mixers are loaded by baseband transimpedance amplifiers (TIAs), based either on common-gate stages or on op-amps with resistive feedback. The flicker noise of the devices of the TIAs is not suppressed, ultimately setting the flicker noise corner of the receiver. To overcome this limitation, the chopper stabilization technique is used to reduce the flicker corner below 100 Hz. Chopper stabilization is a widespread technique, usually applied to voltage amplifiers [50, 67–69]. However, to the best of the authors' knowledge, its use with TIAs in a downconversion mixer is unprecedented. The combination of passive current-mode switches and chopper stabilized TIAs results in a highly linear, low noise downconversion mixer with a very low flicker noise corner.

The schematic of the proposed TIA is shown in Fig. 4.5. The amplifier is based on a common-gate stage. Compared to an op-amp with resistive feedback approach, this choice allows to decouple the input and output common-mode voltages. As a consequence, the input common-mode voltage can be kept low, which is beneficial for the mixer switches (nMOS transistors), without impairing the output swing. Local feedback (transistors $M_3$ and $M_8$) is used around the common-gate input stage (transistors $M_2$ and $M_9$) to decrease the differential TIA input resistance, $R_{\text{in,TIA}}$, as

$$R_{\text{in,TIA}} \approx \frac{2}{g_{m2} g_{m3} r_{01}}. \tag{4.1}$$

The input branches of the TIA are biased with 250 $\mu$A each, such that a differential input resistance of 35 $\Omega$ is achieved at a small power consumption. The input currents are mirrored to the output branches. Eventually, resistors $R$ perform the current-to-voltage conversion.

### 4.1.3 Programmable Divider/Quadrature Generator

As discussed, the local oscillator (LO) quadrature accuracy is the most stringent specification for a receiver tailored for stepped-frequency microwave imaging. The quadrature error must be

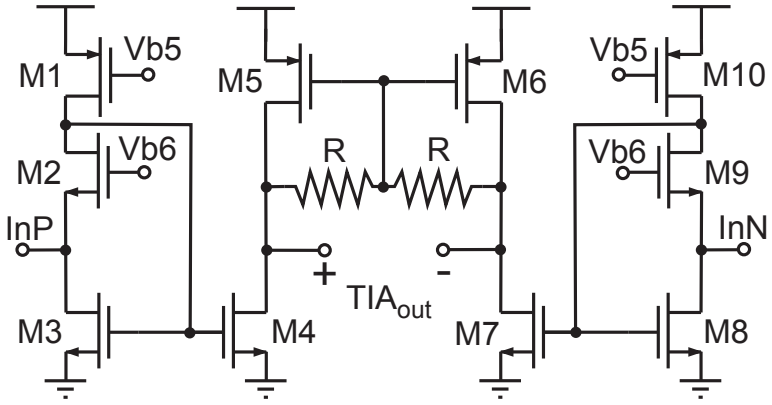


Figure 4.5: Schematic of the TIA.

small, and constant over the entire wide receiver bandwidth. Sudden changes in the I/Q phases cannot be tolerated, even if they occur for few frequencies in the wide covered span.

Accurate generation of quadrature signals over multiple octaves can be achieved by using static frequency dividers by two. However, this technique cannot be used in the proposed radar receiver because of the high frequencies involved. Apart from the power consumption of the divider yielding the frequencies for the higher octave, the generation of the LO signals at twice the frequency, i.e. from 15 to 30 GHz, with extremely low phase noise (also a sensitive specification for the system [39]) and large tuning range, would require many power hungry VCOs to meet the requirements. The use of a polyphase filter to generate the I/Q phases in the higher octave is also a possibility. To meet the required quadrature accuracy over one octave while being robust to process spreads, the filter should feature more than 3 sections, thus introducing more than 18 dB losses. Since a large LO swing is required by the mixer switches, buffers would be needed to drive the polyphase filter and to regenerate the signal after it. Simulations suggest that such buffers would consume as much current as the entire proposed DQG. In addition, the LO signal would be tapped from different points of the circuit to cover the various octaves. As a consequence, the feed to the mixer could be uneven across the band in amplitude and, most importantly, in phase.

To address all the aforementioned issues, we devised an innovative solution, made of a cascade of two programmable injection-locked dividers that can divide by 1 or 2. A PLL (not implemented in this design) is supposed to generate signals over the higher octave, namely from 7.5 to 15 GHz. The DQG is then capable of producing quadrature signals over three octaves starting from the PLL output.

The block diagram of the DQG is shown in Fig. 4.6. Two regenerative buffers (RB), based on injection locked ring oscillators, drive the first programmable divider. An interstage buffer made of two-stage tapered CMOS inverters interfaces the two programmable dividers. The interstage buffer is ac-coupled to the output of the first programmable divider, and the input inverter is biased at its logical threshold by means of replica biasing. A regenerative buffer eventually drives the mixers. The injection locked regenerative buffer intrinsically operates at large output swings, hence providing a large drive to the mixers with minimum amplitude variations across the band. The interface between the LO distribution and the mixers is the same regardless the DQG is dividing by 1, 2, or 4. This avoids discontinuities in the operation of the DQG due to changes in the loading of the LO distribution chain. The architecture of the DQG, made of a

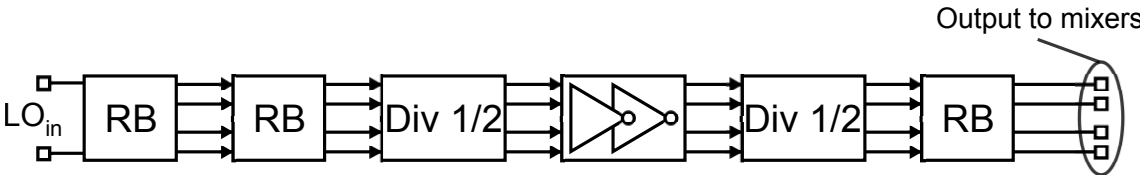


Figure 4.6: Block diagram of the programmable divider/quadrature generator (DQG).

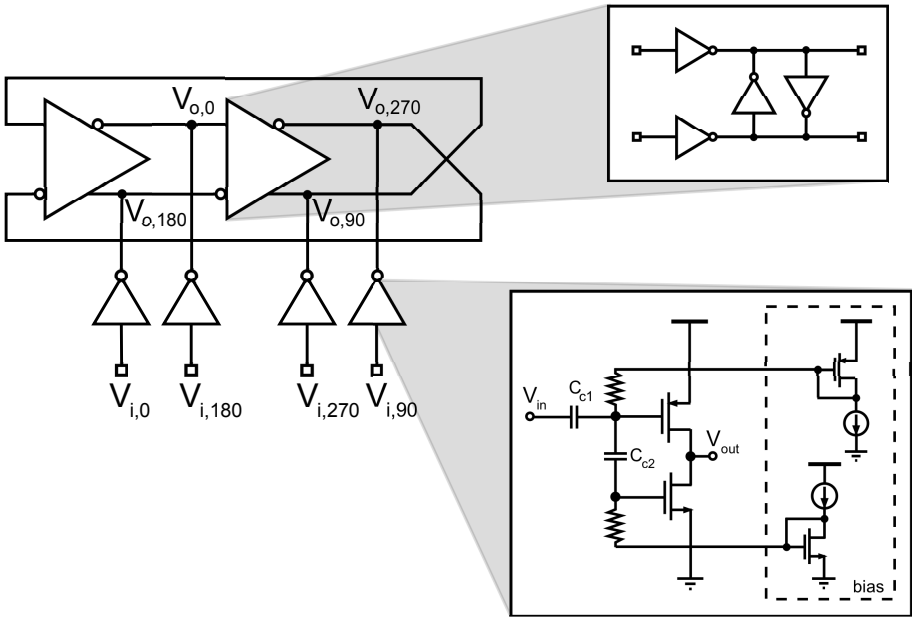


Figure 4.7: Simplified schematic of the regenerative buffer (RB).

cascade of several injection-locked stages, has the advantage of progressively improving the quadrature accuracy [60], such that every stage is contributing to reduce the quadrature error in any used configuration. Moreover, the use of injection locked circuits based on inductorless ring oscillators results in very wide locking ranges [53]. As a consequence, the DQG does not need any calibration nor tuning.

The schematic of the RB is shown in Fig 4.7. The core of the circuit is a two-stage differential ring oscillator in which the delay cells are differential static CMOS latches with input buffers as delay elements. Although the RB is basically a digital circuit in its structure, a full custom design is needed to guarantee the correct operation up to 15 GHz. Analog techniques are also required. An example is given by the injection buffers of the RB, shown in Fig. 4.7. The buffers are essentially CMOS inverters. However, to make them operate correctly in the required frequency range, even in presence of input signals with less than rail-to-rail swing, ac-coupling through capacitors $C_{c1} = 310$ fF and $C_{c2} = 120$ fF is employed, which make the inverters work as analog amplifiers. This is similar to the approach reported in [64]. Note that two *RC* decoupling sections are used in cascade, as opposed to connecting one terminal of both $C_{c1}$ and $C_{c2}$ directly to the input. The chosen arrangement in fact reduces slightly, but effectively, the capacitive loading on the driving stage. Moreover, it allows for a more compact layout since the smaller $C_{c2}$ can be conveniently placed in the neighborhood of the pull-down nMOS, leaving more space for the larger $C_{c1}$. The bias voltages of the nMOS and pMOS transistors are obtained by means of current mirrors, shared among the buffers.

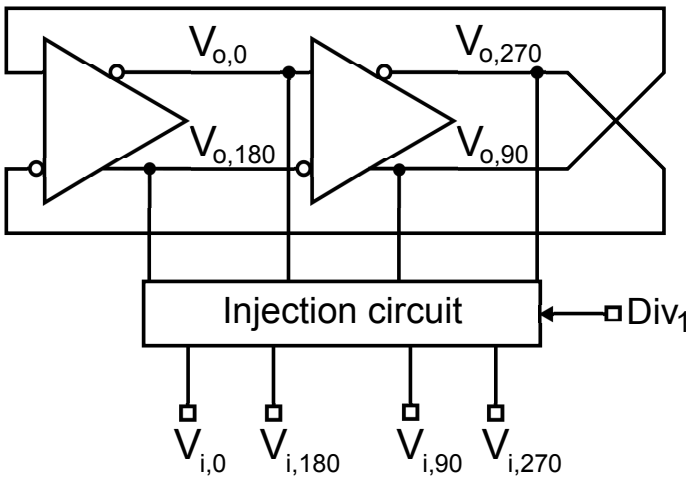


Figure 4.8: Simplified schematic of the programmable frequency divider by 1 or 2.

The schematic of the programmable divider is shown in Fig. 4.8. Similarly to the RB, the programmable divider is built around a two-stage differential ring oscillator. The topology of the delay cell is also similar (cf. Fig. 4.9), although the transistor size is differently optimized in each block. The possibility of having a programmable divider is based on the multi-phase injection locking concept [70]. Depending on the phase progression of the signals fed to the divider, harmonic or super-harmonic injection locking occurs, enabling either division by 1 (same input and output frequency) or frequency division by 2. Different division ratios are hence obtained by reconfiguring the injection network, as shown in Fig. 4.10. In the divide-by-one mode, a complete quadrature sequence (0°, 90°, 180°, and 270°) must be injected at the four nodes of the ring oscillator. Consequently, nodes "A" (cf. Fig. 4.10) are grounded and quadrature phases are injected into the ring oscillator through pseudo-differential pairs. As shown in Fig. 4.9, the pull-up transistors of the delay inverters of the ring oscillator are effectively made larger, as compared to the divide-by-two configuration, to counteract the undesired pull-down effect of the injection devices ($M_{j1}$ through $M_{j4}$) in Fig. 4.10. The latter would in fact tend to decrease the output common mode voltage of the ring oscillator, and in turn the oscillation amplitude. In the divide-by-two mode, nodes "A" in Fig. 4.10 are floating. A signal with 0° phase is fed to both injection devices $M_{j1}$ and $M_{j2}$, that thus operate as a single transistor connected across the output nodes of one of the delay cells of the ring oscillator. Similarly, a signal with 180° phase is fed to injection devices $M_{j3}$ and $M_{j4}$. Such a direct injection arrangement enables superharmonic injection-locking operation [53], and consequently frequency division by 2. The injection devices $M_{j1}$ through $M_{j4}$ are ac-coupled to the phase distribution multiplexers, which are built out of tri-state CMOS gates. The dc bias voltage fed to the injection transistors is tailored for divide-by-1 and divide-by-2 operation. It is important to emphasize, however, that these bias voltages are set by design, and that no tuning is required for the DQG to operate over three frequency octaves.

A test buffer, made of 3 stages of resistively loaded differential pairs, interfaces the differential DQG input to an external single-ended signal, as shown in Fig 4.1. This buffer will be removed once a PLL, directly connected to the DQG, is integrated along with the receiver.

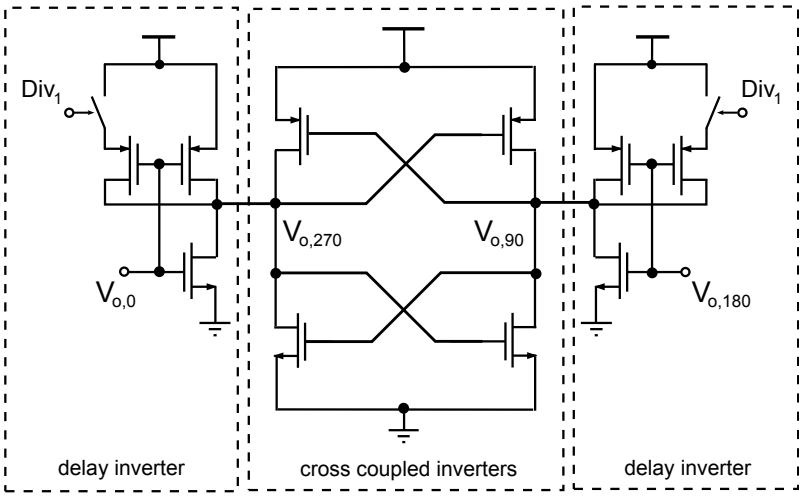


Figure 4.9: Simplified schematic of the delay cell of the programmable divider.

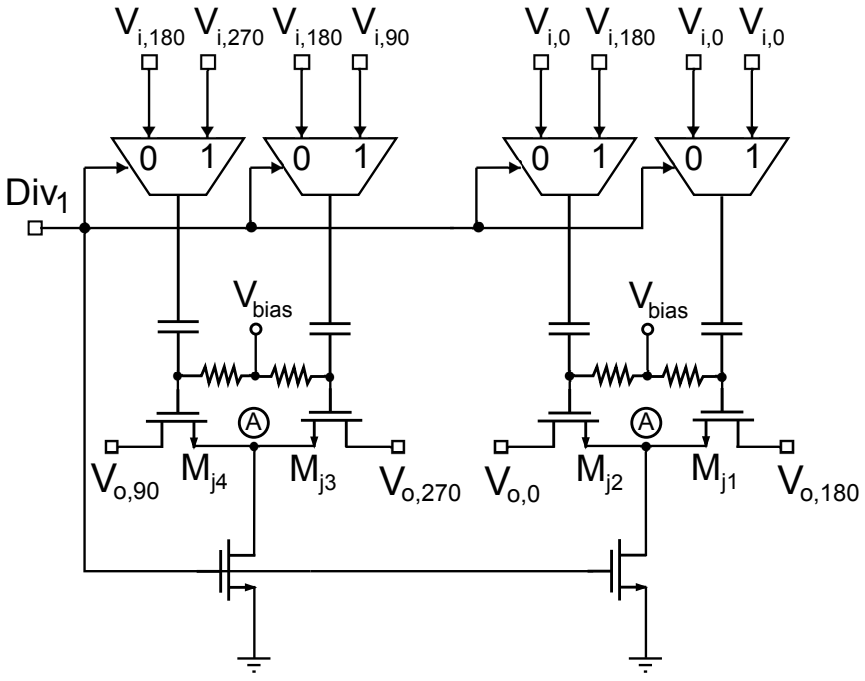


Figure 4.10: Simplified schematic of the injection network of the programmable divider.

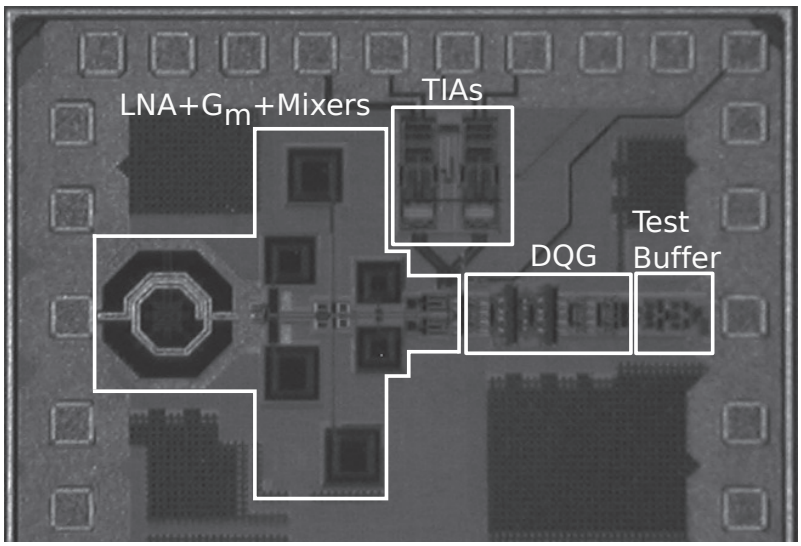


Figure 4.11: Microphotograph of the die. Active area is $870\times550\,\mu m^2$.

## 4.2 Measurement Results

The proposed radar receiver was implemented in a a 65 nm CMOS process. Chip prototypes were fabricated and assembled in chip-on-board fashion for testing. All the pads were wire-bonded with the exception of the input pad of the LNA, which has been probed. A microphotograph of the die is shown in Fig. 4.11, where the various functional blocks are highlighted. The active area is as small as $870\times550\,\mu m^2$.

The supply voltage is 1.2 V. The current drawn from the supply is 34, 16, and 2 mA for the LNA (including bias circuitry), $G_m$ stages, and TIAs, respectively. The DQG draws 51 mA. The overall power consumption of the receiver is thus 124 mW.

The measured conversion gain (CG), LNA input return loss, and receiver NF are reported in Fig. 4.12 across the entire frequency range. The CG is as high as 31 dB, the input matching ($S_{11}$) is lower than -9 dB, and the noise figure ranges from 6.4 to 8.6 dB with an average value of 7.6 dB.

The measured conversion gain as a function of the intermediate frequency is reported in Fig. 4.13 for different values of the LO frequency. The latter are chosen to span the three modes of operation of the DQG. In any case, the baseband bandwidth, limited by the TIA, is 800 kHz.

Several linearity test have been carried out. The measured $P_{1dB}$ is shown in Fig. 4.14. From 2 to 15 GHz it is greater than -28 dBm, well above the -34 dBm maximum received signal that we expect from the analysis in Chapter 2.

Two-tone measurements are performed to assess the intermodulation performance of the receiver. Since, as discussed in Chapter 2, medical imaging is performed in a screened environment, the required third-order intermodulation performance of the receiver is quite relaxed. However, although the desired signal is the only one being received, and although it is a purely sinusoidal tone, still there might be some spurious tones associated with it. Assuming the transmitted signal is generated by an integer-*N* PLL with a reference frequency of some 10 MHz, some reference spurs might be there as undesired interferers. The spurious themselves would be out of the TIA band, and thus be filtered out, but their intermodulation product would corrupt

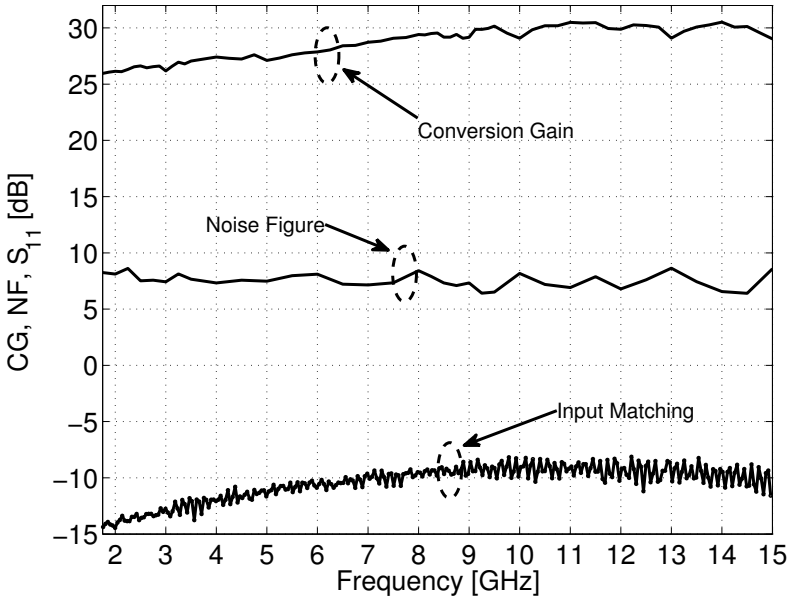


Figure 4.12: Conversion gain (CG), noise figure (NF) and input reflection coefficient ($S_{11}$).

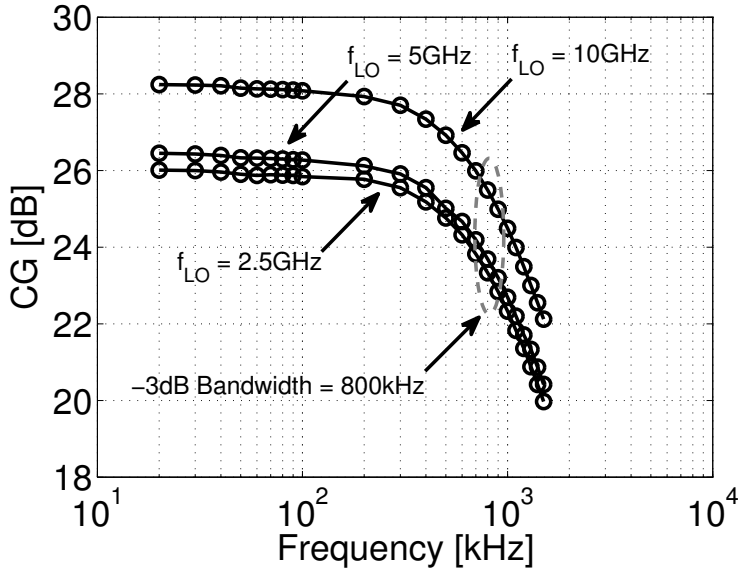


Figure 4.13: Measured conversion gain (CG) as a function of the intermediate frequency for different LO frequencies.

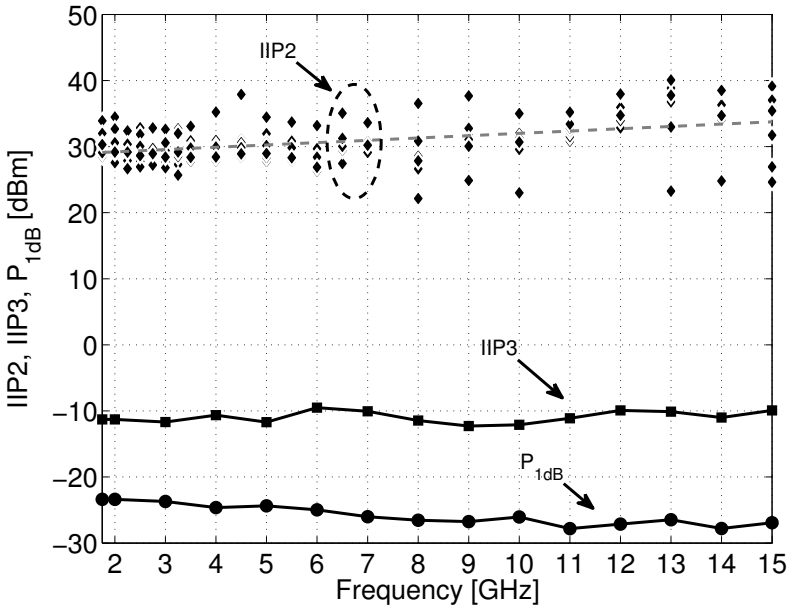


Figure 4.14: Measured $P_{1\text{dB}}$, IIP3 and IIP2; IIP2 is reported for 7 different samples.

the desired signal. To assess this scenario a two-tone test has been carried out with tones at 25 and 50.05 MHz offset from the LO, for various LO frequencies. The IIP3 measured in this condition is reported in Fig. 4.14: it is greater than -12 dBm across the LO frequency range. As a consequence, the maximum relative level of the PLL spurs ($S_l$) that can be tolerated is

$$S_l \leq -\frac{3P_{\text{RX}} - 2\,IIP3 - P_d}{3} = -19\,\text{dBc}, \tag{4.2}$$

where $P_{\text{RX}} = -34$ dBm is the maximum signal we expect to receive, and $P_d = -134$ dBm is the maximum distortion we can tolerate to have a 100 dB dynamic range. Clearly, the third-order intermodulation distortion performance of the proposed radar receiver results in very loose spurious specifications set on the radar transmitter.

As opposed to third-order intermodulation distortion, second-order intermodulation distortion is critical for the proposed direct-conversion receiver, as the skin backscatter acts as a strong in-band interferer (cf. Chapter 2). IIP2 has been measured setting the two tones such that both the tone frequencies and the intermodulation products fall within the TIA band. The result is shown in Fig. 4.14 for 7 chip samples: the median value is 30 dBm while the worst case is 22 dBm. In any case the performance is within the specification singled out in Chapter 2.

The 1/f noise is a potential show-stopper in this system, due to the extremely narrow baseband bandwidth and the direct-conversion architecture. The 1/f noise corner frequency has been measured with the aid of an external ADS1282 ADC. The ADC is an oversampling converter, and it embeds both an anti-alias filter and a decimation filter. Consequently, it sets the noise bandwidth of the receiver to 1 kHz. The chopper frequency has been selected to be 1 MHz to avoid any aliasing (the ADC sampling frequency is 4 MHz), and yet prevent 1/f noise folding. A plot of the measured input-referred noise power density is shown in Fig. 4.15. The flicker noise corner is as low as 40 Hz, an unprecedented result for wireless receivers. The input-referred noise, integrated over the 1 kHz ADC band, and combined with the measured $P_{1\text{dB}}$, gives a dynamic range in excess of 106 dB, showing that the performance of the proposed receiver is

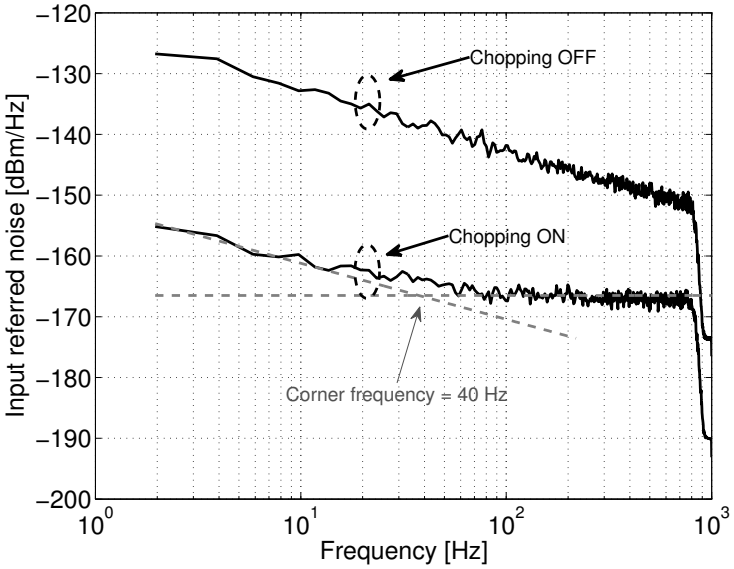


Figure 4.15: Measured input referred noise PSD with the chopper stabilization of the TIA OFF and ON (measurement taken for $f_{LO}$=5 GHz, i.e. DQG in div-2 configuration).

adequate to process simultaneously the strong skin backscatter and the weak echo from the tumor.

In a high resolution imaging system, the quadrature phase and gain mismatches are very critical impairments. The measured I/Q phase and gain mismatches of 7 samples are shown in Fig. 4.16. The quadrature error is less than 1.5° across the band while the gain imbalance is lower than 0.8 dB. In Fig. 4.16, note that a clear systematic gain mismatch is observed. Such a behavior was tracked back to a layout error, resulting in a mismatch in the parasitic resistances of the input traces of the TIAs in the in-phase and quadrature paths. Once the systematic gain error is removed from the data in Fig. 4.16, the residual gain mismatch is limited to few tenths of dB. The good quadrature accuracy achieved over such a wide frequency range confirms that the proposed DQG is capable of excellent performance.

The measured performance of the proposed receiver is summarized in Table 4.2, and compared to that of state-of-the-art wideband wireless receivers. The receiver in [71] is part of a timed-array for radar imaging, e.g it implements the dual approach (time-domain as opposed to frequency-domain) with respect to the proposed receiver. The works in [62, 63] report receivers for software-defined radios, while in [64, 65] receivers for UWB WiMedia radios are presented. Overall, it is not easy to make a fair comparison because of the different applications these broadband receivers are tailored for. However, we note that the proposed receiver features quite a low power consumption while showing a comparable overall performance with respect to the other works. Moreover, it features an unprecedented low 1/f noise frequency corner.

## 4.3 Conclusions

A 65 nm CMOS receiver for breast cancer imaging is presented. The receiver operates from 1.75 to 15 GHz. The large bandwidth together with a dynamic range in excess of 106 dB and I/Q phase mismatches less than 1.5° results in a resolution of 4 mm, adequate to detect even the smallest tumors.

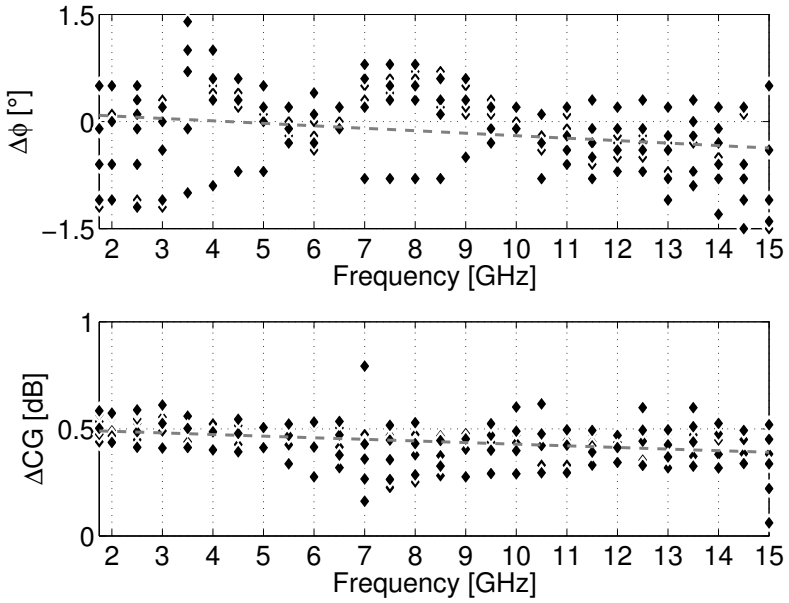


Figure 4.16: Measured quadrature phase error ($\Delta\phi$) and conversion gain mismatches ($\Delta$ CG) for 7 samples.

Table 4.2: Summary of the measured performance and comparison with the state-of-the-art.

| | This work | [71] | [63] | [62] | [64] | [65] |
|---|---|---|---|---|---|---|
| Bandwidth [GHz] | 1.75–15 | 1–15 | 0–6 | 0.1–5 | 3–9 | 3.1–10.6 |
| Tech. | 65 nm CMOS | 130 nm CMOS | 130 nm CMOS | 45 nm CMOS | 65 nm CMOS | 130 nm SiGe BiCMOS |
| $CG$ [dB] | 31 | 24 | 0–68 | -2–82 | >55 | 10-68 |
| $NF$ [dB] | <8.6 | <5.5 | 29$^{\dagger}$ | <6.5 | <7.5 | <5.8 |
| 1/f corner freq. [Hz] | 40 | – | – | – | – | – |
| $P_{1dB}$ [dBm] | >-28 | >-26 | −50 | – | – | -20 |
| $IIP3$ [dBm] | >-12 | – | -48 | >-10 | >-4 | -10 |
| $IIP2$ [dBm] | > 22 | – | 40 | >30 | – | – |
| $\Delta\phi$ [°] | <1.5 | – | – | – | – | – |
| $P_{dc}$ [mW] | 124 | 236 $^{\ddagger}$ | 680 | <115 | 230 | 425* |

$^{\dagger}$Evaluated from reported sensitivity, noise bandwidth, and SNR. $^{\ddagger}$One channel of timed array. *Complete transceiver.

# 5 A Wide-Tuning Range Integer-N Phase-Locked Loop

In this chapter, the design of a a 65 nm CMOS wideband integer-N PLL is discussed. The PLL operates as a frequency synthesizer for the breast cancer diagnostic imaging transceiver front-end. Two VCOs tune from 6.5 to 11.8 GHz and from 11.0 to 18.4 GHz, respectively, yielding an overall PLL fractional tuning range of 85 % with a spur level always better than -48 dBc/Hz. The phase noise at 10 MHz offset from the carrier is lower than -129 dBc/Hz, while the RMS jitter is lower than 680 fs. The PLL consumes 46 mW from a 1.2 V supply.

The chapter is organized as follows. In Section 5.1, the phase domain model of the integer-N PLL is presented. Particular attention is given to the phase noise modeling and simulation. In Section 5.2, 5.3 and 5.4, the noise transfer function in the phase domain along with an accurate noise model of each PLL building block are described. In Section 5.5, some issues related to the spur generation are highlighted. The system-level and circuit-level design of each block of the PLL are treated in Sec. 5.6. Measurements and conclusions close the chapter.

## 5.1 Phase Domain Model

Due to the very small period of the VCO compared to the time required to reach lock, it is very expensive to directly simulate a PLL system in the time domain. This is particularly true when large division ratios $N$ are desired, such as in frequency synthesizers. In fact, the simulation of a large number of cycles at the input of the phase-frequency detector is needed to reach lock, that corresponds to a dramatic number of periods of the VCO. Given that at least 10-20 simulation points are required for each VCO period, this translate to a very long and hence impractical simulation.

This considerations are true when simulating the PLL in the time-domain using voltage-current models. However, it is also possible to formulate models based on the phase of the signals, i.e. phase-domain models. When using these models, signals with large difference in frequency are not present, resulting in a much faster simulation. Additionally, a small-signal model of the closed-loop operation of the PLL can be easily derived, making it easier to study the closed-loop dynamics of the system and noise performance.

A general linear phase-domain model [42] of a phase-locked loop is shown in Fig. 5.1. Note

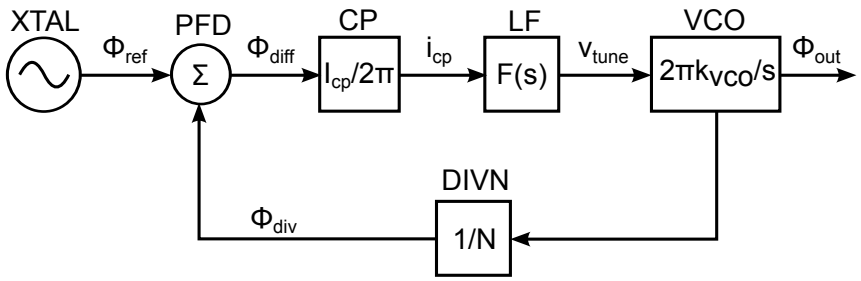


Figure 5.1: Linear time-invariant phase-domain model of a integer-$N$ phase-locked loop.

that all the signals are represented as a phase $\phi$, except the ones at the input of the VCO and loop-filter (LF). In this model, the loop filter transimpedance $F(s)$ converts the charge pump current $i_{cp}$ to the tuning voltage $v_{tune}$ as $v_{tune} = i_{cp}F(s)$. The mapping from voltage to frequency is designed to be linear, so a first-order model is sufficient. In the phase-domain, this translates into the tuning voltage integrated to the output phase through the VCO gain $k_{VCO}$, i.e. $\phi_{out} = (2\pi k_{VCO}/s)v_{tune}$. The output phase $\phi_{out}$ is divided by $N$ in the feedback path and compared to the reference phase $\phi_{ref}$ through the action of the phase-frequency detector (PFD). The error signal generated by the PFD is then used to drive the charge pump (CP), ultimately closing the phase locking loop.

This model can be used to predict the small-signal phase behavior of the loop. To this regard, it is useful to define the following relationships:

$$\begin{aligned} G_{fwd} &= \frac{\phi_{out}}{\phi_{ref}} = \frac{I_{cp}k_{VCO}F(s)}{s} \\ G_{rev} &= \frac{\phi_{div}}{\phi_{out}} = \frac{1}{N} \end{aligned} \tag{5.1}$$

and therefore the loop gain as

$$T = G_{fwd}G_{rev} = \frac{I_{cp}k_{VCO}F(s)}{sN}. \tag{5.2}$$

The loop gain is used to design and explore the stability of the loop. In particular, the phase margin is an important design parameter that dramatically impacts the phase noise or jitter performance of the loop.

Note that if one is not interested in seeing the output harmonic of the VCO, the model can be reduced to the one shown in Fig. 5.2, where the VCO and DIVN have been merged together. Practically speaking, this means building a Verilog-AMS block of the VCO+DIVN. As a result, only harmonics around the reference frequency are present, dramatically increasing the speed of the simulation. It turns out that this model is very useful to predict the behavior of the loop in transient condition. Most importantly, it is used to predict some important loop parameters when the loop is in locked condition, such as the residual phase error $\phi_{diff}$ and the tuning voltage $v_{tune}$. These parameters are critical to correctly predict the phase noise behavior of the PLL.

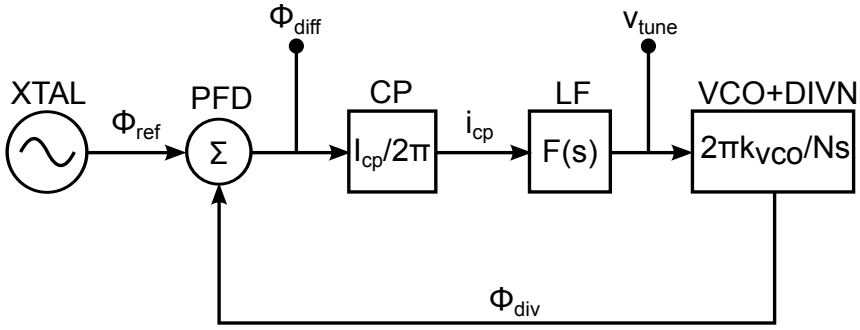


Figure 5.2: Linear time-invariant phase-domain model of a integer-$N$ phase-locked loop.

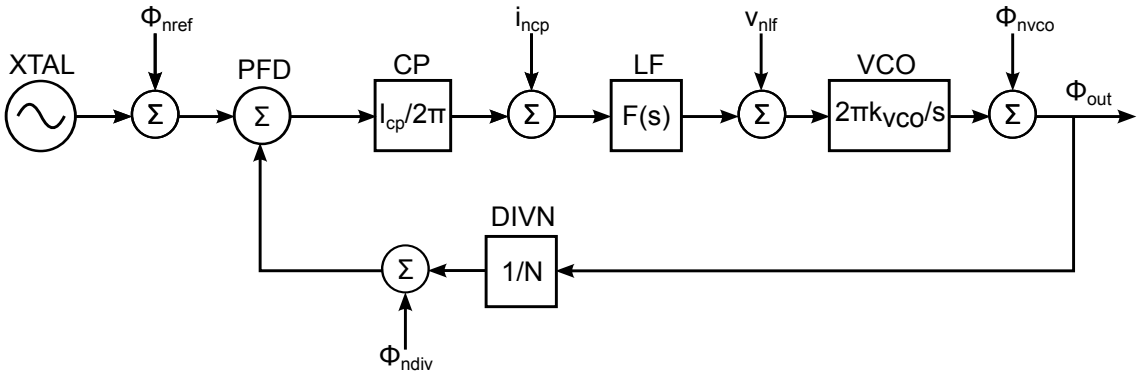


Figure 5.3: Linear time-invariant phase-domain model of a integer-$N$ phase-locked loop with noise sources.

## 5.2 Noise Transfer Functions

Fig. 5.3 shows the linearized phase-domain model of the phase-locked loop in presence of several noise sources [72]. These noise sources represents the noise produces by the blocks (due to thermal, shot and flicker noise sources) or coupled into the blocks from the power supply and the substrate. In this model, $\phi_{nref}$ represents the phase noise injected by the reference, $\phi_{nvco}$ the VCO phase noise and $\phi_{ndiv}$ the phase noise added by the divider in the feedback path. Note that $\phi_{nref}$, $\phi_{nvco}$ and $\phi_{ndiv}$ are phase noise, while $i_{ncp}$ and $v_{nlf}$ represent noise current and voltage injected by the charge pump and loop filter, respectively.

The transfer functions from the various noise sources to the output are

$$\begin{aligned}
G_{nref} &= \frac{\phi_{out}}{\phi_{nref}} = \frac{G_{fwd}}{1+T} = \frac{NG_{fwd}}{N+G_{fwd}}, \\
G_{ndiv} &= -G_{nref} = -\frac{NG_{fwd}}{N+G_{fwd}}, \\
G_{ncp} &= \frac{\phi_{out}}{i_{ncp}} = \frac{2\pi}{I_{cp}} G_{nref}, \\
G_{nlf} &= \frac{\phi_{out}}{v_{nlf}} = \frac{2\pi}{I_{cp}F(s)} G_{nref}, \\
G_{nvco} &= \frac{\phi_{out}}{\phi_{nvco}} = \frac{1}{1+T} = \frac{N}{N+G_{fwd}}.
\end{aligned} \tag{5.3}$$

From the transfer functions derived in (5.3), it is possible to get insight on resulting phase noise

shape at the output of the PLL.

As $s = j\omega \to 0$, $G_{fwd} \to \infty$ because of the integration action of the VCO on the tuning voltage $v_{tune}$. Consequently at DC, $G_{nref}$,$G_{ndiv}$,$G_{ncp} \to N$ and $G_{nvco} \to 0$. This means that at low offset frequency, the noise of the PLL is dominated by the noise injected by the reference oscillator, CP and PFD, loop filter and feedback divider while the phase noise of the oscillator is reduced by the low pass action of the feedback loop.

On the other hand, as $s = j\omega \to \infty$, $G_{fwd} \to 0$. Consequently at frequencies well outside the loop bandwidth, $G_{nref}$,$G_{ndiv}$,$G_{ncp} \to 0$ and $G_{nvco} \to 1$ and the phase noise of the VCO is entirely injected at the output. In fact at high frequencies, the low pass nature of the loop filter blocks the contributions coming from the feedback path.

Note that in both cases attention must be payed to the structure of the loop filter. In fact, depending on its order, different noise sources may inject thermal noise inside the VCO tuning voltage.

## 5.3 Noise Models

The noise of the PLL can be predicted by applying the model described in Fig. 5.3. The first step is to simulate the various noise sources, which usually involves the use of a simulator, such as SpectreRF. Periodic noise analysis is used to record the output noise generated by the crystal oscillator (XTAL), PFD, CP, VCO and DIVN, while AC noise analysis is enough for the noise coming from the LF.

The second step is to code the noise sources into models and simulate them in the closed loop of Fig. 5.3. One way is to build Matlab models of the noise sources, report them at the output using Eq. (5.3) and use a root-mean-square sum to produce the output noise of the PLL. The other way is to build Verilog-AMS models of each block and use simulation to determine the output result. It employs building noisy phase-domain models of each block, where the signals are phase. Once the phase discipline is added to the Verilog-AMS engine, AC Noise simulation can be employed to determine the output. Both these approaches are fast and easy; as such, a description of the model both for Matlab and Verilog-AMS is given along with the setup to simulate the output noise of each block.

### 5.3.1 PFD and CP

Modeling the noise of the PFD and CP is important because they are the main contributors to the PLL noise at low frequency offset from the carrier. The noise current injected by the PFD and CP into the loop filter can be found directly with simulation. This involves driving the PFD and CP with a representative periodic signal and using a PNoise analysis to record the power spectral density of the noise current at the output.

The simulation setup is depicted in Fig. 5.4. Two buffer are used to strongly drive the PFD with the signals coming from the XTAL and DIVN. Based on the difference in phase between the reference signal and the one coming back from the DIVN, two control signals (i.e. UP and DOWN) are generated by the PFD to drive the charge pump. The CP injects current inside the loop filter until lock condition is reached.

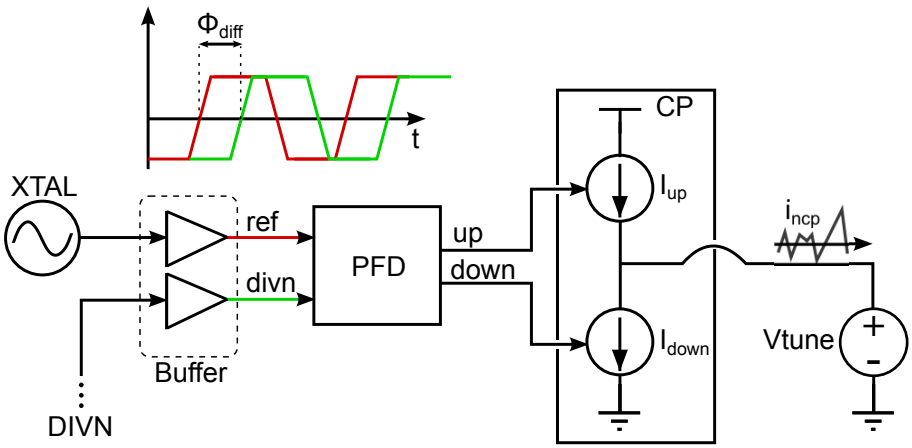


Figure 5.4: Setup for the simulation of the power spectral density of the output noise current $I_{ncp}$ of the PFD and CP.

Two main factors determine the accuracy of the model of noise current $i_{ncp}$ injected into the loop filter in lock condition: First, the static phase error $\phi_{diff}$ of the loop. Second, the average tune voltage $V_{tune}$ at which the loop lies once in lock.

The static phase error $\phi_{diff}$ of a second order loop filter is zero as long as the output resistance of the charge pump is infinite. In practice, this is not the case and the static phase error $\phi_{diff}$ grows as the output resistance decreases. In lock condition, this translates into having the control signals $up$ and $down$ of the charge pump not perfectly aligned and a fix amount of charge injected into the loop filter at each reference cycle. The loop counteracts the injected charge cycle after cycle, determining the average tune voltage at which the loop is locked. However, the bigger the static phase error $\phi_{diff}$, the larger the amount of noise current injected in the loop filter during each reference cycle. Additionally, a larger level of injected charge increases the spur level as well, as it will be delineated later on in this chapter. Since a practical charge pump shows a finite output resistance, this translates into the problem of designing a buffer, PFD and CP with as less noise as possible and a CP with the largest output resistance.

The average tune voltage $V_{tune}$ is the average voltage at which the VCO varactor voltage lies in lock condition. Depending on the desired output frequency and the sub-band behaviour of the VCO, the charge pump often operates at output tune voltages close to the Vdd or ground. Due to the fact that the charging currents $I_{up}$ and $I_{down}$ are generated by a pMOS and nMOS device, respectively and the channel modulation effect is prominent in deep submicron technologies, the charging and discharging currents will be different depending on the output tune voltage $V_{tune}$. If $V_{tune}$ is greater than $V_{dd}/2$, the charging current will be smaller than the discharging current. Similarly to the action of the finite static phase error, this translates into an additional amount of charge and noise injected into the loop filter at each reference cycle, degrading both the noise and spur performance of the loop.

To properly simulate the worst-case noise current behaviour of the PFD and CP in lock condition we need to know both the static phase error of the loop and the maximum (minimum) voltage at which the loop tune voltage could lie. The latter can be calculated from the sub-band behaviour of the VCO and the minimum frequency step of the desired integer-N PLL. The former can be simulated in the time-domain by using the equivalent model presented in Fig. 5.2, where the only non-ideal block consists on the merged Verilog-AMS model of the VCO and DIVN.

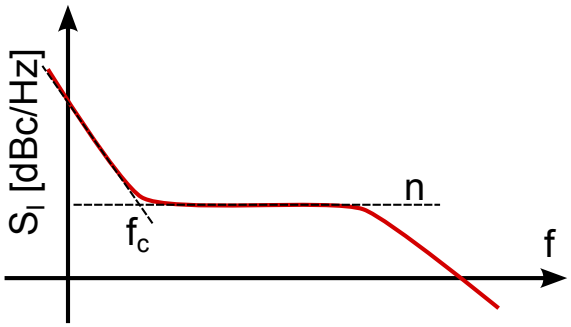


Figure 5.5: Typical power spectral density $S_{I_{PFD+CP}}$ of the noise current generated by the PFD and CP.

Generally, the power spectral density of the output noise current $I_{ncp}$ appears as in Fig. 5.5, in which case the noise is parameterized by $n$ and $f_c$, where $n$ is the white noise floor and $f_c$ the flicker noise corner. This corresponds to a power spectral density

$$S_{I_{PFD+CP}}(\Delta f) = n\left(\frac{f_c}{\Delta f}+1\right), \tag{5.4}$$

where $\Delta f$ is the offset frequency from the XTAL reference frequency.

The corresponding Verilog-AMS block can be modeled as

```
1  // VerilogA for Buffer+PFD+CP
2
3  `include
4  `include
5  `include
6
7  module v_pfd(pin,nin,out);
8  input pin, nin; output out;
9  phase pin, nin;
10 electrical out;
11 parameter real gain = 500e-6 from (0:inf); // transfer gain (A/cycle)
12 parameter real n = 4e-25 from [0:inf); // white output current noise (A2/Hz
       )
13 parameter real fc = 201e3 from [0:inf); // flicker noise corner frequency (
       Hz)
14 analog begin
15 I(out) <+ -gain*Theta(pin,nin) / (2*`M_PI);
16 I(out) <+ white_noise(n,      ) + flicker_noise(n*fc, 1,      );
17 end
18
19 endmodule
```

### 5.3.2 LF

Even in the phase domain model of the PLL, the loop filter remains in the voltage domain. Consequently, the loop filter is represented by a full circuit-level model, where the noise sources are naturally included in the resistors' model. Because of the integrating action of the VCO on the tune voltage, the voltage noise generated by the LF appears at the output as phase noise. As such, particular attention has to be paid on the choice of the filter order and element values

during the design. Generally speaking, the noise generated by the loop filter passive network can be modeled as a noisy current source in parallel with the filter admittance $Y(s)$. The power spectral density of the equivalent current noise generator can be expressed as

$$S_{I_{LF}}(s) = 4k_B T\Re\{Y(s)\}, \tag{5.5}$$

where $k_B$ is the Boltzmann's constant and T the absolute temperature in Kelvin. The Verilog-AMS block model for the third-order loop filter can be written as

```
// VerilogA for Third-Order LF

`include
`include
`include

module v_loopfilter(n,o,agnd);
electrical n;
electrical o;
electrical agnd;
parameter real c1 = 1.7e-12 from (0:inf);
parameter real c2 = 40.2e-12 from (0:inf);
parameter real c3 = 0.607e-12 from (0:inf);
parameter real r2 = 16.3e3 from (0:inf);
parameter real r3 = 30.6e3 from (0:inf);
electrical int;
capacitor #(.c(c1)) C1(n, agnd);
capacitor #(.c(c2)) C2(int, agnd);
resistor #(.r(r2)) R2(n, int);
resistor #(.r(r3)) R3(n, o);
capacitor #(.c(c3)) C3(o, agnd);


endmodule
```

### 5.3.3 VCO

Oscillators are responsible for most of the noise at the output of the majority of the well-designed frequency synthesizers. This is because of the oscillators inherently amplifies noise found near the oscillation frequency and any of its harmonics. In fact, oscillators tend to convert perturbations from any source into a phase variation at their output with an amplification that varies with $1/\Delta f$. Assuming that the perturbation consists of white noise and flicker noise, the phase noise of the oscillator can be modeled as

$$S_{\phi_{VCO}}(\Delta f) = n\left(\frac{1}{\Delta f^2} + \frac{f_c}{\Delta f^3}\right), \tag{5.6}$$

where $\Delta f$ is the offset frequency from the carrier, $n$ is the portion of $S_{\phi_{VCO}}$ attributable to the white noise sources alone at 1 Hz and $f_c$ is the flicker noise corner frequency, as detailed out in Fig. 5.6.

The corresponding Verilog-AMS block can be modeled as

```
// VerilogA for VCO

```

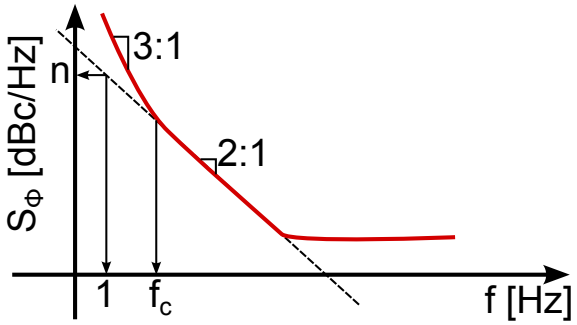


Figure 5.6: Typical phase noise $S_\phi$ behavior of an oscillator circuit.

```
3  `include
4  `include
5  `include
6
7  module v_vco(in,out);
8  input in; output out;
9  voltage in;
10 phase out;
11 parameter real gain = 225e6 from (0:inf); // VCO gain, Kvco (Hz/V)
12 parameter real n = 2.63; // white output phase noise at 1 Hz (rad2/Hz)
13 parameter real fc = 8e4 from [0:inf); // flicker noise corner frequency (Hz
     )
14 analog begin
15 Theta(out) <+ 2*`M_PI*gain*idt(V(in));
16 Theta(out) <+ flicker_noise(n, 2,      ) + flicker_noise(n*fc, 3,      );
17 end
18
19 endmodule
```

## 5.4 PLL Phase Noise Spectrum

The overall noise at the output of the PLL can be visualized either in Cadence, using the proposed phase-domain models, or in Matlab. In both the cases, since the noise sources are uncorrelated, the noise spectra of each PLL block must be added to obtain the overall noise spectrum of the PLL at the output:

$$S_{OUT}(s) = S_{XTAL}|G_{nref}|^2 + S_{I_{PFD+CP}}|G_{ncp}|^2 + S_{I_{LF}}|F(s)G_{nlf}|^2 + S_{\phi_{VCO}}|G_{nvco}|^2, \tag{5.7}$$

where $S_{XTAL}$ is a generic model for the XTAL oscillator, usually derived from its datasheet or measurements. The RMS phase error at the output of the PLL is given by

$$\sigma_{\phi,OUT} = \frac{180}{\pi}\sqrt{\int_{fmin}^{fmax} 2S_{OUT}(f)df} \tag{5.8}$$

and the corresponding RMS jitter in seconds is

$$\sigma_{t,OUT} = \frac{1}{f_{OUT}}\frac{\sigma_{\phi,OUT}}{360}, \tag{5.9}$$

where $f_{OUT}$ is the PLL output frequency.

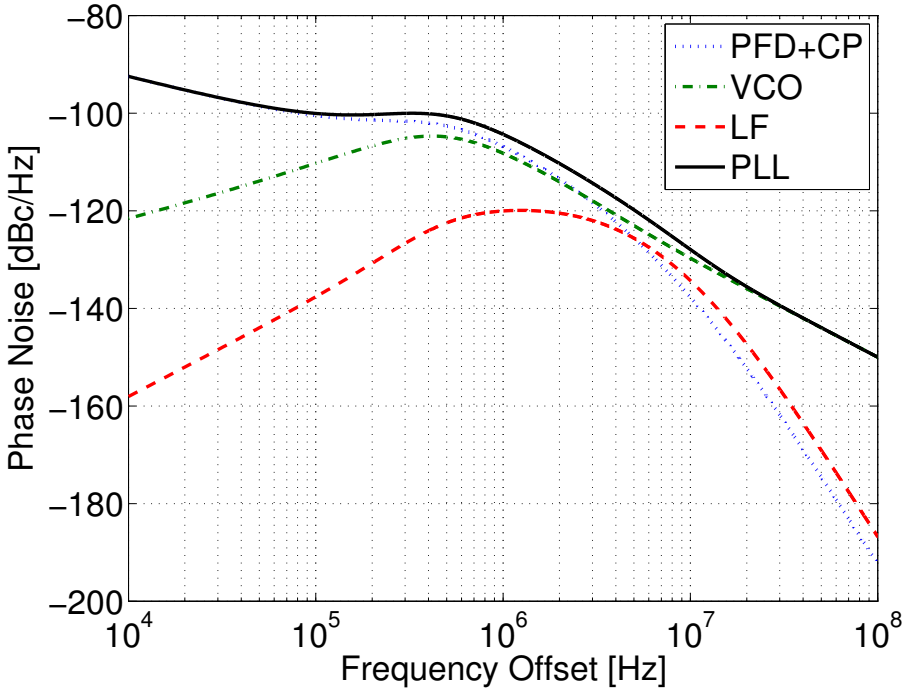


Figure 5.7: Typical behavior of the modeled phase noise spectrum of a PLL.

An example of the typical behavior of the output noise spectrum of a PLL based on the aforementioned noise models is given in Fig. 5.7. The phase noise generated by the VCO was measured with post-layout simulations. Similarly, the current noise injected into the loop by PFD and CP was simulated following the procedure in Sec 5.3.1. The noise of the crystal reference is absent, but can be measured with a spectrum analyzer and added to the simulation using (5.8).

As expected, the VCO noise dominates the phase noise spectrum outside the loop bandwidth, whereas the PFD and CP noise dominate at low offset frequencies. The LP filter contributes to the phase noise with a peaking around the loop bandwidth. Note that the XTAL noise is not present in this simulation. Particular attention has to be given to the design of CMOS buffers that connect the crystal oscillator to the PFD and the ones that connect the DIVN to the PFD. In fact, a large size in the transistors reduces the flicker noise contribution to the PLL output spectrum at low frequency offsets (i.e. less than 100 kHz), but increases the power consumption and probably needs an improved driving capability of the DIVN block.

## 5.5 Charge Pump and Spurs

In PLL frequency synthesizers, there are several types of spurious outputs with many different causes. However, the reference spur is by far the most common type. The existence of this spur is not surprising because many of the PLL's components including the PFD and CP are clocked at the reference frequency $f_{REF}$. Spurs from these sources can be seen in the PLL's output spectrum at an offset of $\pm f_{REF}$ from the PLL's output frequency. The spurs are caused by non-idealities in the PLL components such as mismatched propagation delay in the PFD and CP, charge injection and current mismatches in the CP, and leakage current on the VCO tuning node $V_{tune}$.

In this section, we analyze the impact of a generic voltage $g(t)$ superimposed to tune voltage $V_{tune}$ of the PLL while in lock condition on the reference spur level. The function $g(t)$ is periodic

with $T_{REF}$ and takes into account all the aforementioned issues. Note that thanks to the low-pass action of the loop gain $T$ of the system, the spur level will be better than the one predicted in this calculation. However, the calculation does not take into account leakage from the substrate and the varactor node into the loop filter.

The PLL output voltage can be written as

$$V_o(t) = V_o cos\left[\omega_{FR}t + k_{VCO}\int V_{tune}dt + k_{VCO}\int g(t)dt\right] \tag{5.10}$$

where $V_o$ is the amplitude, $\omega_{FR}$ the free running frequency, $k_{VCO}$ the VCO gain, $V_{tune}$ the tune voltage and $g(t)$ is a generic function that can be effectively approximated by the first coefficient of its Fourier series as

$$g(t) = a_0 + a_1 cos(\omega_{REF}t). \tag{5.11}$$

The output voltage $V_o(t)$ can be approximated as

$$\begin{aligned} v_o(t) \simeq & V_O cos\left[(\omega_{FR} + k_{VCO}V_{tune} + k_{VCO}a_0)t\right] \\ & - \frac{V_o k_{VCO}a_1}{\omega_{REF}} sin\left[(\omega_{FR} + k_{VCO}V_{tune} + k_{VCO}a_0)t\right] sin\left[\omega_{REF}t\right] \end{aligned} \tag{5.12}$$

and therefore

$$\begin{aligned} v_o(t) \simeq & V_O cos\left[(\omega_{FR} + k_{VCO}V_{tune} + k_{VCO}a_0)t\right] \\ & - \frac{V_o k_{VCO}a_1}{2\omega_{REF}} cos\left[(\omega_{FR} + k_{VCO}V_{tune} + k_{VCO}a_0 - \omega_{REF})t\right] \\ & + \frac{V_o k_{VCO}a_1}{2\omega_{REF}} cos\left[(\omega_{FR} + k_{VCO}V_{tune} + k_{VCO}a_0 + \omega_{REF})t\right]. \end{aligned} \tag{5.13}$$

At this point, the spur level determined by the function $g(t)$ superimposed to the tune voltage is given by

$$SpurLevel = 20\log\left(\frac{k_{VCO}a_1}{2\omega_{REF}}\right). \tag{5.14}$$

It is clear that once the function $g(t)$ is known, the first coefficient of its Fourier series $a_1$ can be calculated and hence the spur level. This is done for a generic triangular function shown in Fig. 5.8, that is the most common voltage shape superimposed to the tune voltage.

In the general case, the $k$-th coefficient of the Fourier series of a periodic function $g(t)$ can be

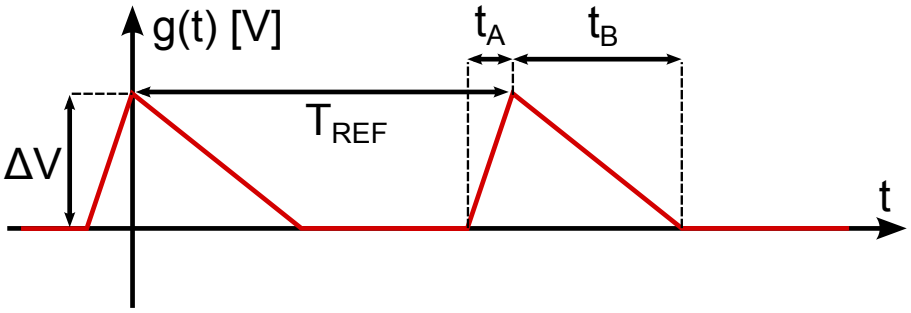


Figure 5.8: A generic triangular function.

calculated as

$$a_k = \frac{2}{T_{REF}} \int_0^{T_{REF}} g(t) \cos\left(\frac{2\pi k t}{T_{REF}}\right) dt. \tag{5.15}$$

In the case of the triangular function shown in Fig. 5.8, it becomes

$$\begin{aligned} a_k =& \frac{2}{T_{REF}} \int_0^{t_B} \left(-\frac{\Delta V}{t_B} + \Delta V\right) \cos\left(\frac{2\pi k t}{T_{REF}}\right) dt \\ &+ \frac{2}{T_{REF}} \int_{T_{REF}-t_A}^{t_{REF}} \left(\frac{\Delta V}{t_A} + \Delta V\right) \cos\left(\frac{2\pi k t}{T_{REF}}\right) dt \\ =& \frac{2}{T_{REF}} \left[\frac{\Delta V T_{REF}}{2\pi k} \sin\left(\frac{2\pi k t}{T_{REF}}\right)\right]_0^{t_B} + \frac{2}{T_{REF}} \left[\frac{\Delta V T_{REF}}{2\pi k} \sin\left(\frac{2\pi k t}{T_{REF}}\right)\right]_{T_{REF}-t_A}^{T_{REF}} \\ &+ \frac{2}{T_{REF}} \left(-\frac{\Delta V}{t_B}\right) \left[\frac{t T_{REF}}{2\pi k} \sin\left(\frac{2\pi k t}{T_{REF}}\right) + \frac{T_{REF}^2}{(2\pi k)^2} \cos\left(\frac{2\pi k t}{T_{REF}}\right)\right]_0^{t_B} \\ &+ \frac{2}{T_{REF}} \left(\frac{\Delta V}{t_A}\right) \left[\frac{t T_{REF}}{2\pi k} \sin\left(\frac{2\pi k t}{T_{REF}}\right) + \frac{T_{REF}^2}{(2\pi k)^2} \cos\left(\frac{2\pi k t}{T_{REF}}\right)\right]_{T_{REF}-t_A}^{TREF}. \end{aligned} \tag{5.16}$$

The average value $a_0$ and the first coefficient $a_1$ can be calculated as

$$a_0 = \frac{(t_A + t_B)\Delta V}{2}, \tag{5.17}$$

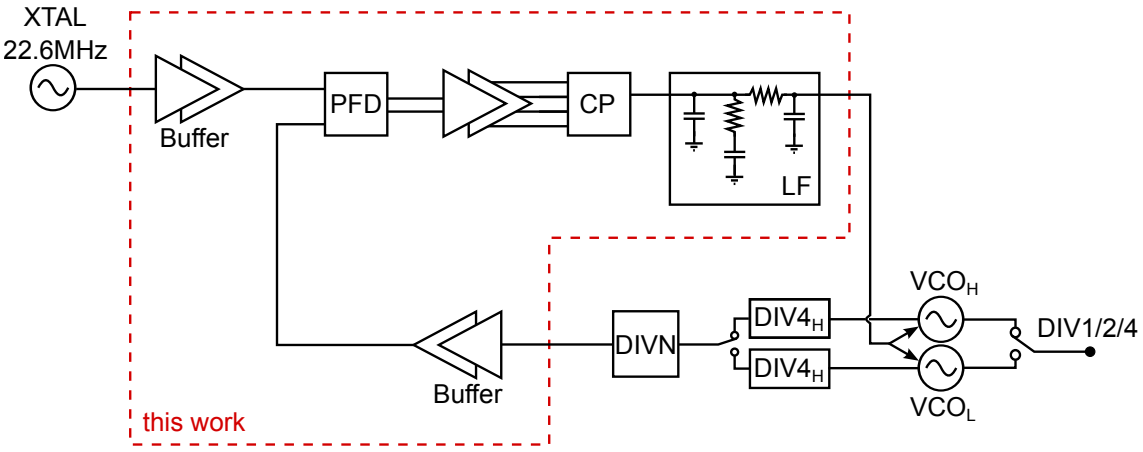


Figure 5.9: Simplified block diagram of the designed integer-N PLL.

and

$$
\begin{aligned}
a_1 = & \frac{2}{T_{REF}} \frac{\Delta V}{\omega_{REF}} \sin(\omega_{REF} t_B) \\
& - \frac{2}{T_{REF}} \frac{\Delta V}{\omega_{REF}} \sin(\omega_{REF}(T_{REF} - t_B)) \\
& - \frac{2}{T_{REF}} \frac{\Delta V}{t_B} \left[ \frac{t_B}{\omega_{REF}} \sin(\omega_{REF} t_B) + \frac{1}{\omega_{REF}^2} \cos(\omega_{REF} t_B) - \frac{1}{\omega_{REF}^2} \right] \\
& + \frac{2}{T_{REF}} \frac{\Delta V}{t_B} \left[ -\frac{T_{REF} - t_A}{\omega_{REF}} \sin(\omega_{REF}(T_{REF} - t_A)) - \frac{1}{\omega_{REF}^2} \cos(\omega_{REF}(T_{REF} - t_A)) + \frac{1}{\omega_{REF}^2} \right].
\end{aligned}
\tag{5.18}
$$

As an example, the reference spur level generated by a triangular wave with $t_A$=$t_B$= 2ns, $f_{REF}$=25 MHz, $\Delta V$=2 mV and $k_{VCO}$=550 MHz/V is -43 dBc.

## 5.6 PLL Circuit Design

The block diagram containing the main blocks of the designed PLL is shown in Fig. 5.9. The PLL relies on two VCOs not to impair the phase noise performance for the tuning range. Each VCO is followed by an injection-locked prescaler by 4 ($DIV4_H$ and $DIV4_L$). The programmable divider by N (DIVN) output is buffered to the PFD together with the crystal oscillator signal from outside the chip. The CP and the third-order loop filter close the loop. Another buffer is placed between the PFD and the CP to driver the CP with strong signals and derive the 4 phases that it requires, as detailed out in Sec. 5.6.3. The two VCOs, the injection-locked prescaler by 4 and the programmable divider by N are part of a previous design. Therefore, the attention here is focused on the system-level design of the PLL and the circuit-level design of the PFD, CP and loop filter.

A detailed block diagram of the designed PLL is sketched in Fig. 5.10, where a set of ancillary circuits is highlighted. The blue blocks are dedicated to buffer outside the chip useful test points, the green ones to force a desired PLL status from the outside in case of malfunctioning, and the

red ones belong to the coarse tuning digital machine.

Starting from the blue circuits, two test points are made available from the PLL. When SEE_DIVN is high, the DIVN buffer is activated and the output of the DIVN is buffered to a divide-by-2 circuit realized with a D-type flip-flop closed in feedback loop. The division is used to make the DIVN signal duty cycle 50%. After division the signal is again buffered to the TST_DIVN pad. The second test point is for the loop tune voltage. When SEE_VTUNE is high, a unity gain buffer op-amp is used to load the VTUNE_OUT pad with the loop tune voltage. The red circuits are dedicated to the coarse tuning digital machine. At the start-up, the DIVN modulus is set by feeding the FREQ_SELECT 8-bit to the divider. This defines the desired PLL output frequency. Once the FREQ_SELECT word is selected, the COARSE_START pulse is given to the coarse tuning machine. The coarse tuning machine forces the tune voltage to 600 mV. Consequently, the TO_HIGH_IMP_CP signal goes high and sets the CP in high impedance configuration (all the switches are open). At this point, the coarse tuning machine works to choose the appropriate VCO between $VCO_H$ and $VCO_L$ and the best capacitor bank code. Then, it releases the tune voltage and the CP, and the PLL loop continues in normal operation until lock condition is reached. The green circuits are used in case of coarse tuning machine malfunctioning. In this case, BYPASS is set high and the VCO_SEL_EXT and VCO_CAP_EXT are used to select the desired VCO and capacitor bank combination. Further, the tune voltage can be set to 600 mV via TO600MV_EXT signal or forced to a desired level from the outside by closing the FORCE_VTUNE switch.

### 5.6.1 System Level Design

The transceiver specifications were carefully derived in Chapter 2. The PLL is required to synthesize the 7-16 GHz frequency range, while the 3.5-8 GHz and 1.75-4 GHz bands are obtained by subsequent divisions, as detailed out in Chapter 4. A 100 MHz step is required as it allows fast settling and results in a maximum unambiguous range of 0.5 m, more than enough for the intended application. The VCO phase noise specification is better than -110 dBc/Hz at 1 MHz offset, while the integrated phase noise error has to be less than 1.5° for all the generated carriers in the 7-16 GHz frequency range.

Given the desired output frequencies and the integrated phase noise requirements, the system level design of a PLL involves the decision of the loop bandwidth, the loop filter order, the phase-margin and the charge pump current [73]. Note that in this system, the locking time is not an issue and can be set as large as needed. However, because of the process spread together with the wide range of frequencies desired at the output, it is challenging to achieve a consistent performance over all the desired output frequencies.

Since the design of the proposed PLL is based on two previously designed VCOs, post layout simulations of the tuning range, VCO gain and phase noise at 1 MHz offset at the two edges of the tuning range are reported in Tab. 5.1. The geometric mean of the VCO gain is 545 MHz, while the geometric mean of the output frequency is 11.7 GHz. These values are meaningful in order to minimize the performance variation over the desired output frequencies. Note that the highest frequency of the tuning range is higher than 18 GHz to take into account for extra parasitics and PVT variations.

The loop bandwidth is one of the most critical parameter. The choice of the loop bandwidth

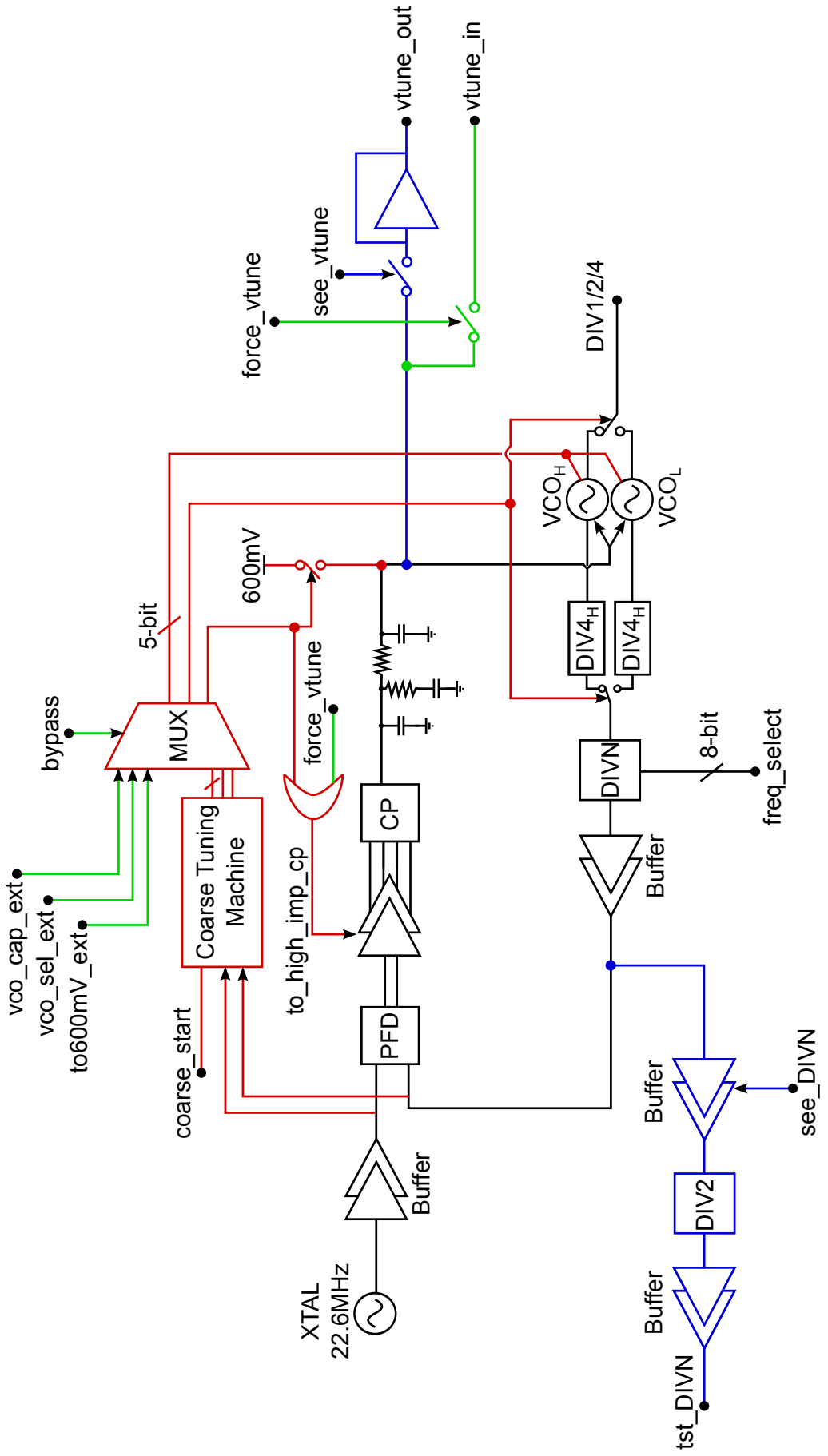


Figure 5.10: Complete block diagram of the designed integer-N PLL.

Table 5.1: VCO tuning range, gain and phase noise.

| VCO | Frequency [GHz] | $K_{VCO}$ [MHz/V] | P.N. @ 1 MHz [dBc/Hz] |
|---|---|---|---|
| $VCO_L$ | 6.7 | 225 | -115 |
| | 12.6 | 1062 | -112 |
| $VCO_H$ | 11.6 | 337 | -108 |
| | 20.14 | 1100 | -110 |

usually involves a trade-off between spur levels and lock time. A smaller loop bandwidth will improve the spur levels at the expense of lock time. However, since lock time and spurs are not a major consideration, the loop bandwidth is chosen to minimize the integrated phase noise. To this regard, note that since the PLL noise tends to be flat while the VCO noise rolls off, there is an offset frequency at which they are equal. Choosing the loop bandwidth as this special offset frequency is a good starting point to design a PLL for minimum integrated phase noise. Given the simulated noise floor of the PFD and CP and the average phase noise performance of the multi-band VCO, the loop bandwidth is set to 1 MHz.

The phase margin has an impact on the integrated phase noise, as well. If the phase margin is too small, there will be peaking in the phase noise response near the loop bandwidth. In general, designing for high phase margin yields the lowest integrated noise because it causes a much flatter response. This is true as long as a longer locking time is not considered an issue. Since this is the case, the loop is design for a phase margin of 60° to obtain a phase noise response as flat as possible and stability in all the frequency range and process corner variations.

The charge pump current is directly related to the amount of in-band phase noise of the PLL and the spur levels. A higher charge pump current promises better phase noise performance but it increases the spur levels. At the same time, the choice of a higher order loop filter can decrease the spurs level. A passive filter architecture is employed, avoiding the use of noisy active devices and extra complexity typical of active filters. A third order loop filter is chosen to further reduce the spur level. A charge pump current $I_{cp}$ of 500 $\mu$A allows to keep the integrated RMS phase error below 2° at the maximum operating frequency.

### 5.6.2 Phase-Frequency Detector

The standard implementation of the PFD is shown in Fig. 5.11. The circuit consists of two edge-triggered resettable D flop-flops (DFFDR) with the D input connected to the logical one and an AND port. The DFFRD is realized in TSPC CMOS logic while the AND port in static CMOS. The parasitic capacitance $C_{par}$ arising from the layout together with the delay introduced by the AND gate are enough to eliminate the dead zone of the PFD.

The CP, as it will be discussed in Sec. 5.6.3, needs the inverse of the UP and DOWN signals as well. These signals are generated by buffering UP and DOWN with two chains of inverters each. In one of the two chains, an inverter is substituted with a transmission gate to obtain the inverted signal at the output. This solution is preferred over taking directly the output QN of the DFFDR because it allows for faster rising and falling edges of the UP, UPN, DOWN, DOWNN signals. Moreover, the signals output by PFD would need buffer anyway so this comes for free.

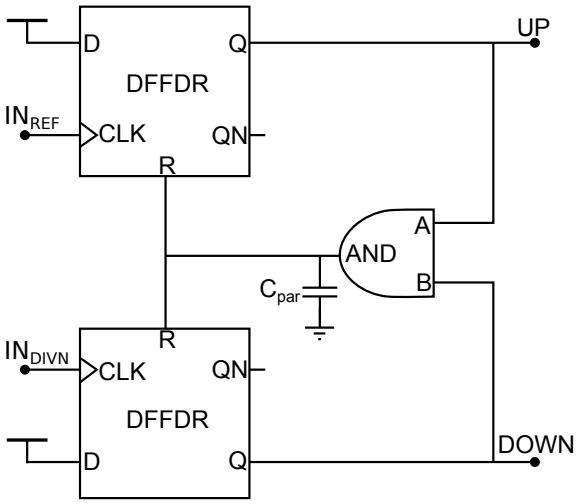


Figure 5.11: Schematic of the phase-frequency detector.

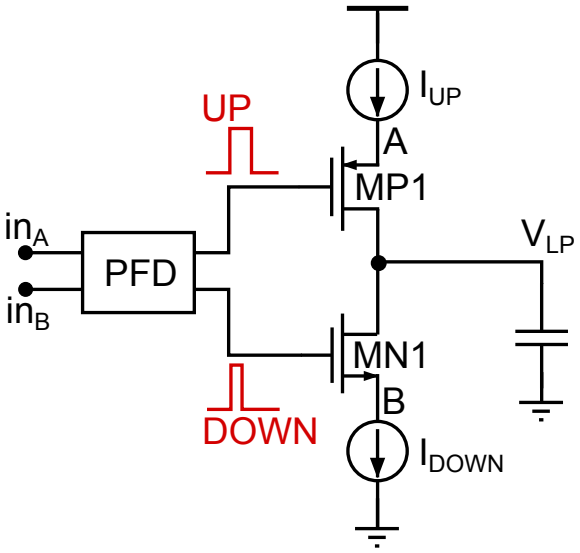


Figure 5.12: Conceptual block diagram of the charge pump.

### 5.6.3 Charge Pump

One of the key elements of the PLL is the design of the CP. A conceptual diagram of the ideal CP is shown in Fig. 5.12. The CP is composed by two current sources, $I_{UP}$ and $I_{DOWN}$ controlled by the switches MP1 and MN1, respectively. By driving the CP with the output of the PFD, a charge is injected into the loop filter until the lock condition is reached. At that point, the PFD still generates UP and DOWN output pulses with the same duration and zero charge is ideally injected into the loop filter.

However, when implemented at circuit level, both the PFD and CP show non idealities that increase the spur levels and degrade the in-band phase noise performance of the PLL. This is mainly due to current mismatches between $I_{UP}$ and $I_{DOWN}$, charge injection, charge sharing and clock feedthrough [4]. Current mismatches are primarily caused by the channel-modulation effect, particularly severe in deep submicron technologies. Depending on the average value of the output voltage $V_{LP}$, the charging current $I_{UP}$ may become different from the discharging current $I_{DOWN}$ due to the effect of the finite output resistance of the MOS transistors MN1

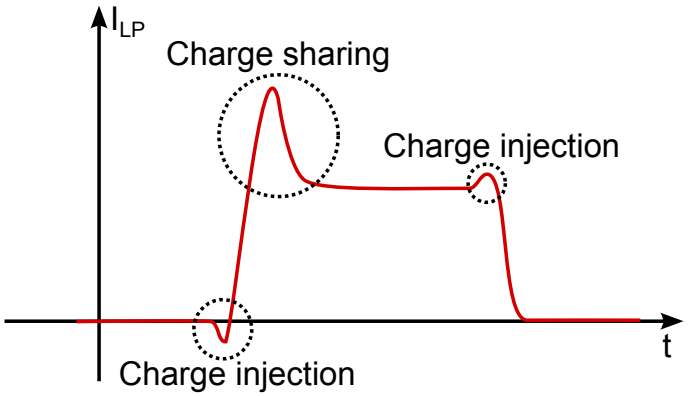


Figure 5.13: Qualitative behavior of a current pulse generated by a non-ideal charge pump [4].

and MP1. This leads to a non-zero charge injected in the filter even when the loop is in lock condition. Additionally, when a MOS switch transistor directly connected to the output is turned off, a portion of the charge hold in its channel will flow in the LF, leading to a charge injection error. Finally, charge sharing through parasitic capacitances may happen between nodes A and B when the MOS switches are turned on, further injecting undesired charge into the loop filter. The effects of the aforementioned non-idealities on a current pulse injected in the LF are qualitatively shown in Fig. 5.13.

The proposed charge pump is depicted in Fig. 5.14. A current steering topology is adopted [74,75]. This topology employs an additional complementary switch branch, driven by the inverse of the signals used to drive the output node switch transistors. The use of two complementary branches allow the charging and discharging currents $I_{UP}$ and $I_{DOWN}$ to continuously flow through the charge pump. Since the current flowing through transistors MP1 and MN1 stays constant, the voltage variations at nodes A and B are minimized. As a consequence, the charge sharing from nodes A and B to the output node $V_{LP}$ is drastically mitigated. A unity gain configuration op-amp is used to hold the voltage of the replica node C at the same level of the output node $V_{LP}$.

To minimize the mismatches between the charging and discharging currents $I_{UP}$ and $I_{DOWN}$, an additional op-amp is employed to ensure that nodes C and D are at the same level. In this way, the amplifier forces the $I_{UP}$ and $I_{DOWN}$ currents to be equal, except for the mismatches between transistors MP6 and MP1 as well as the ones associated with transistors MN6 and MN1. A relatively large capacitor $C_{stab}$ needs to be employed to ensure the stability of the loop. In this design, $C_{stab}$=24.8 pF to ensure a phase margin of 70° in all the PVT corners. The two op-amps are designed for a moderate gain of 20 dB. They are based on a current-mirror error amplifier topology and consume 40 $\mu$A each.

Dummy transistors MP3, MP5, MN2 and MN4 are driven by complementary phases and have source and drain short-circuited. They are designed half-size transistors MP2, MP4, MN3 and MN5, and are employed to capture the charge that would be injected in the LF upon turning-off transistors MP2, MP4, MN3 and MN5, respectively and release the charge required to create the channel during the turning-on.

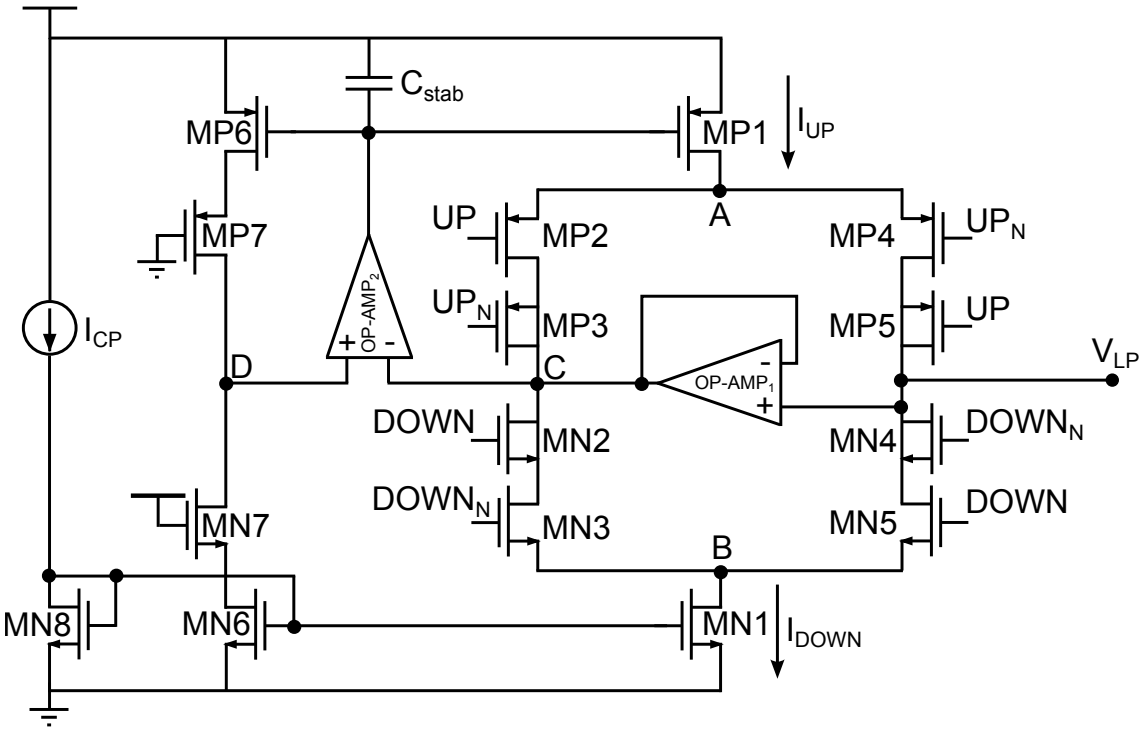


Figure 5.14: Schematic of the charge pump.

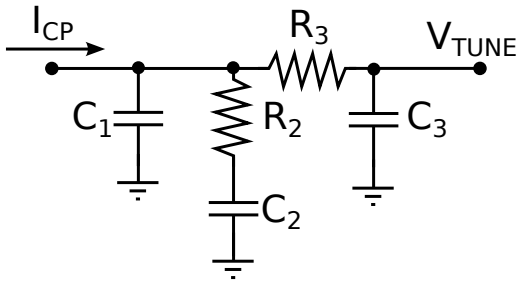


Figure 5.15: Schematic of the third-order loop filter.

### 5.6.4 Loop Filter

The third order loop filter is useful to filter spurs or noise generated by the PLL at offset frequencies of ten times the loop bandwidth or greater. In this design, a third order loop filter is employed, as depicted in Fig. 5.15.

In a second order loop filter, given the loop bandwidth and the phase margin of the system, all the values of the passive elements can be determined in a closed form solution. In the third order loop filter, due to the additional degree of freedom, loop bandwidth and phase margin are not enough to derive the filter values in a close form solution. The ratio of the time constants of the first and third pole of the filter $T31$ needs to be specified together with the desired loop bandwidth and phase margin to calculate the filter element values [73]. If the value of $T31$ is decreased, then the capacitor $C_3$ will become larger and the resistor $R_3$ smaller. This is beneficial because a smaller resistor $R_3$ introduces less thermal noise that can add to the out-of-band noise. Further, a larger capacitor $C_3$ makes the loop less sensitive to the varactor VCO input capacitance (that needs to be at least 5-6 times smaller than $C_3$ for reliable operation). However, the filtering action of the third order loop filter decreases with decreased values of T31, so a

Table 5.2: Third order loop filter element values.

| $C_1$ | $C_2$ | $R_2$ | $C_3$ | $R_3$ |
|---|---|---|---|---|
| 1.8pF | 58.3pF | 11.2kΩ | 660fF | 30kΩ |

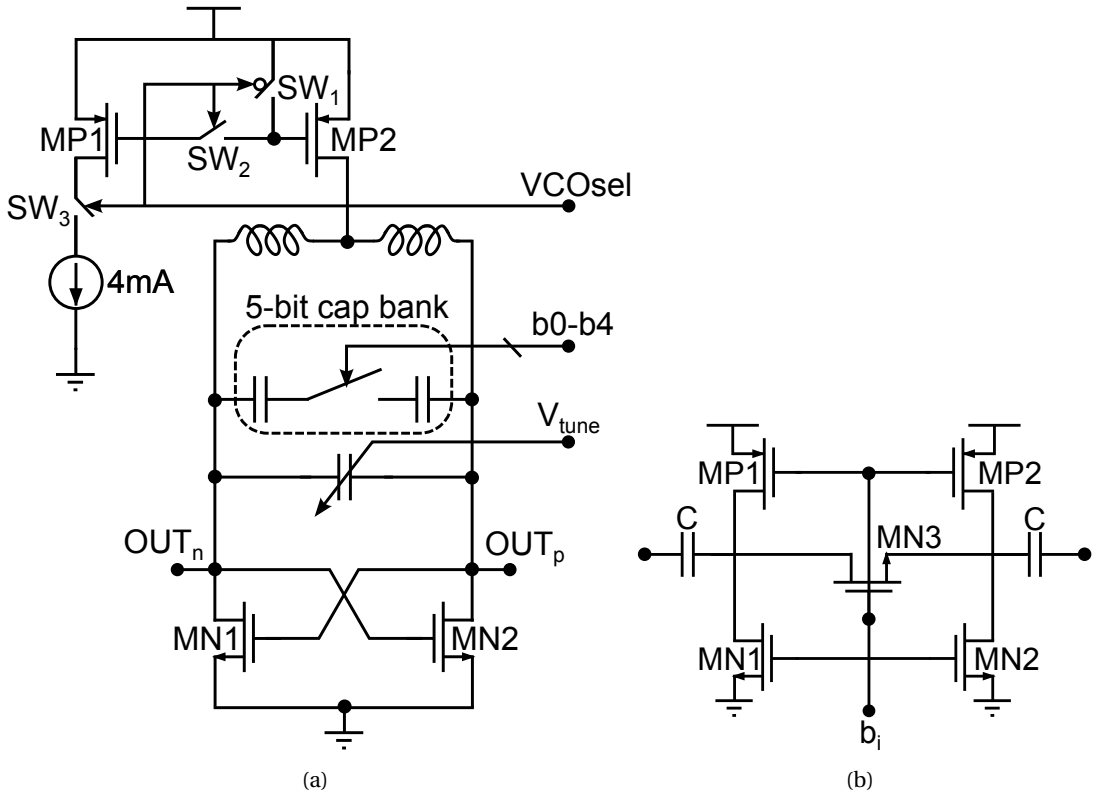


Figure 5.16: Schematic of the VCOs (a) and unity cell capacitance of the capacitor bank (b).

compromise is needed. In this design, a value of T31=0.3 was chosen to design the capacitor $C_3$ sufficiently larger than the VCO input capacitance. This value does not degrade the noise and spur filtering significantly. The values of the designed filter are listed in Tab. 5.2.

### 5.6.5 VCO

The VCO [76] is based on the well known differential LC topology with a cross-coupled nMOS pair. As shown in Fig. 5.16, the bias current source is based on pMOS devices and it is connected to the inductor center tap. As a consequence, the center tap of the inductor sits at a voltage of about $V_{dd}/2$. Moreover, since the parasitic capacitance at the central tap of the inductor is not critical, it can be used to filter out the high frequency noise contribution of the current source MP2. Since at first order the parasitic capacitance of MP2 does not have any negative impact, a longer channel length can be selected for MP2, allowing to reduce the flicker noise generated by the tail source.

The reference current of 4 mA is shared between both the VCOs. In order to allow to turn on just one VCO at a time, control switches were introduces in the bias network. When $VCO_{sel}$ is high, $SW_2$ and $SW_3$ are on and $SW_1$ is off and the bias current is correctly mirrored. When

$VCO_{sel}$ is low, both $SW_2$ and $SW_3$ are off while $SW_1$ is on, forcing the transistor MP2 and thus the VCO in the off-state. When turned on, the current mirror ratio is 3.5 and 5 for $VCO_L$ and $VCO_H$, respectively.

Both VCO inductors are single-turn inductors with octagonal shape. The coil of $VCO_L$ features 350 pH inductance, while the coil of $VCO_H$ 180 pH inductance. The tank capacitance was divided in a 5-bits capacitor bank plus a varactor to allow for continuous tuning. The width of the transistor $M_{SW}$ has been chosen as a compromise between the quality factor of the capacitor bank $Q_C$ and the tuning range. The larger the switch, the higher the quality factor but the lower the the on/off capacitance ratio of the switched capacitor unity cell. Transistors MN1 and MN2 are used to set the DC voltage at the drain and source of $M_{SW}$ to ensure that it turns on appropriately. Consequently, the are designed with minimum channel width and longer than minimum length. Transistors MP1 and MP2 ensure that the drain and source voltage of $M_{SW}$ are at $V_{dd}$ when the cell is in the off state. This minimizes the drain-bulk and source-bulk capacitances of $M_{SW}$, maximizing the $C_{on}/C_{off}$ ratio of the unity cell and thus the tuning range. They are designed with minimum width and channel length.

### 5.6.6 Prescaler

The block diagram of the implemented prescaler is shown in Fig. 5.17(a). The divide-by-four circuit is implemented around a four-stage ring oscillator [76]. Two prescalers $DIV4_L$ and $DIV4_H$ were connected to $VCO_L$ and $VCO_H$, respectively. The size of the injection transistors MN1, MN2, MN3 and MN4 is $5/0.06\,\mu m$ for both prescalers. The schematic of the inverters used to realize the core of the ring is shown in Fig. 5.17(b). The size of the transistor of the inverters is different in the two prescalers, in order to better center the free running frequency of the two ring oscillators with the VCOs' tuning range. The size of the pMOS transistors is the same of the nMOS transistors. The size is $5/0.06\,\mu m$ and $5/0.08\,\mu m$ for the $DIV4_H$ and $DIV4_L$, respectively.

### 5.6.7 Programmable Divider

The programmable divider is based a dual modulus low-power and truly modular architecture [76, 77]. It consists of a modular structure based on a chain of $n$ 2/3 divider cells connected like a ripple counter, as shown in Fig. 5.18. The 2/3 divider cell divides the frequency of the input signal either by 2 or by 3, and outputs the divided clock signal to the next cell in the chain. The $p_i$ and $M_i$ logic levels determine the momentaneous division ratio of the cell. The $M_i$ signal becomes active once in a division cycle. At that moment, the state of the input is checked, and if $p_i = 1$, the 2/3 divider cell is forced to swallow one extra period of the input signal, thus the cell divides by 3. If $p_i = 0$, the cell divides by 2. Regardless of the value of the $p_i$ input, the $M_i$ signal propagates up in the chain upon being reclocked to the preceding cell.

In [77], it is shown that all integer division ratios ranging from $2^n$ (if all $p_i = 0$) to $2^{n+1} - 1$ (if all $p_i = 1$) can be realized. The division range is thus rather limited, amounting to roughly a factor of two between maximum and minimum division ratio. Since the sum of the tuning range of the two VCOs has to be at least one octave, the division range is not enough to cover the required tuning range with some margin for PVT and process variations. In [77], a solution to extend the division range is proposed. By deliberately setting the $M_i$ signal to the logical one,

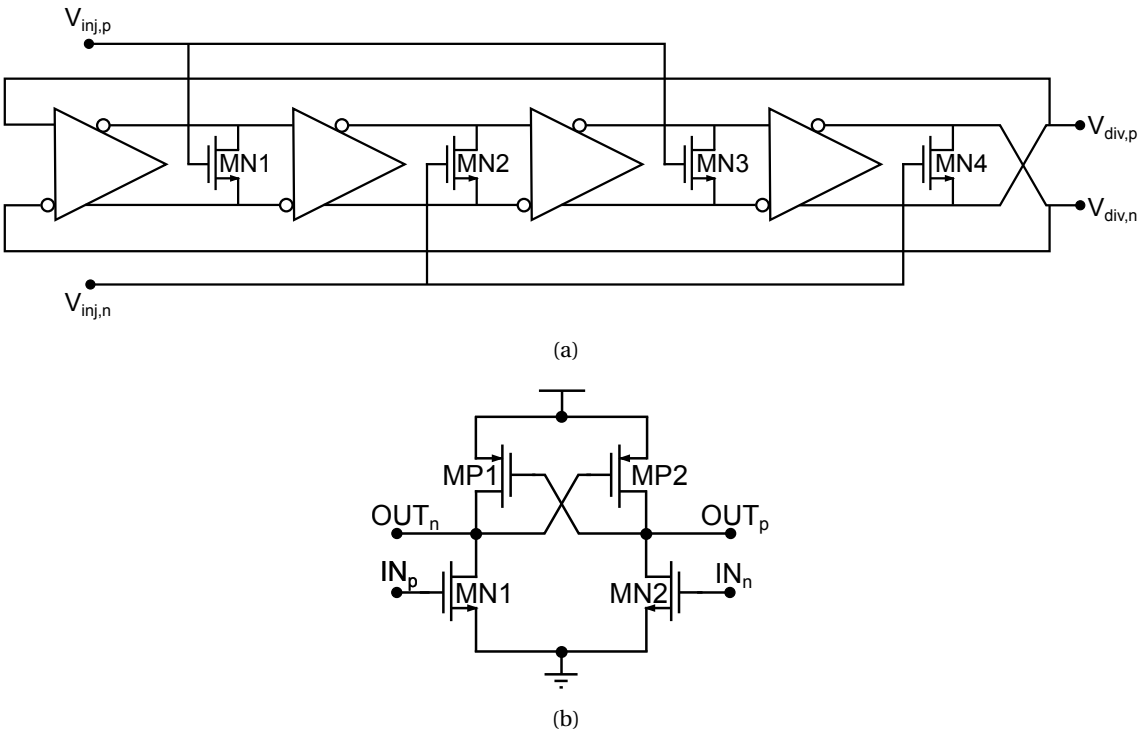


Figure 5.17: Schematic of the injection-locked divide-by-four prescaler (a) and inverter cell (b).

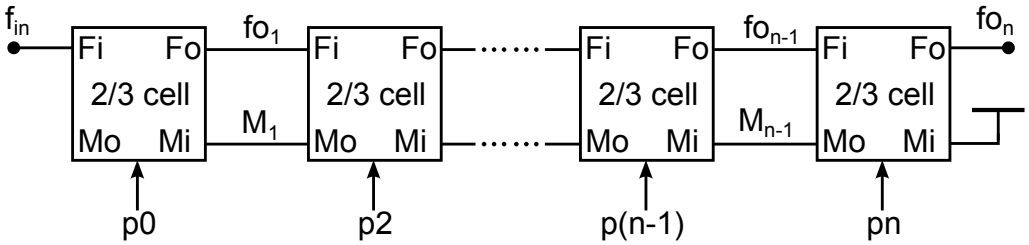


Figure 5.18: Basic architecture of the programmable divider.

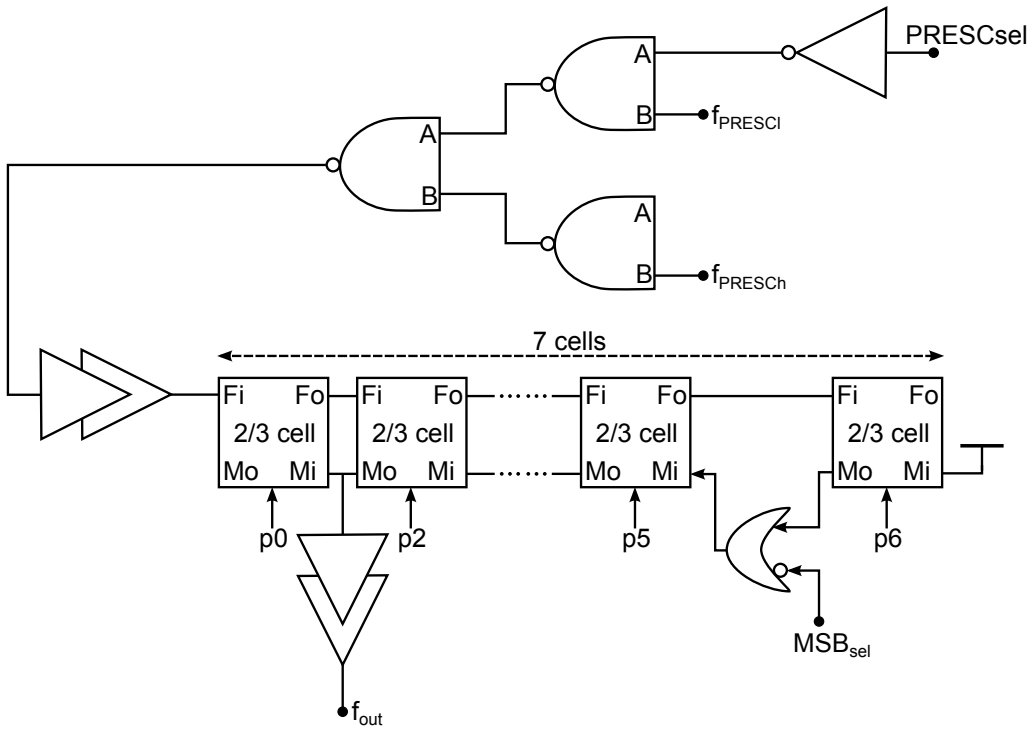


Figure 5.19: Schematic of the implemented programmable divider with extended division range and input buffer.

the influence of all the 2/3 cells to its right can be overwritten. The divider chain behaves as if it has been shortened from $n$ to $n_{min}$ cells, where $n_{min}$ are the number of 2/3 cells that are effectively influencing the division cycle. Only a few extra OR gates are required to adapt $n_{min}$ to the programmed division word. With the additional logic, a division ratio ranging from from $2^{n_{min}}$ (if all $p_i = 0$) to $2^{n+1} - 1$ (if all $p_i = 1$) can be achieved and the maximum and minimum division ratios can be set independently.

The schematic of the realized programmable divider is shown in Fig. 5.19. A multiplexer is added in front of the divider in order to choose between the two prescaler outputs, depending on which VCO is turned on. It is realized as a cascade of NAND gates and an inverter. By choosing $n_{min} = 6$ and $n = 7$, a division factor ranging from $N_{min} = 64$ to $N_{max} = 255$ is obtained. This means that the divider can cover a frequency range of $[4 f_{ref} N_{min} \quad 4 f_{ref} N_{max}] = [5.78\,\text{GHz} \quad 23.05\,\text{GHz}]$, large enough to include both VCO tuning ranges. The schematic of each 2/3 cell is shown in Fig. 5.20. The D flip-flop was realized in TSPC CMOS logic while the logic gates outside the flip-flop were realized in static CMOS logic. In [77], CML logic was used for the 2/3 cell, naturally yielding the inverted signal. In this design, static CMOS logic was used and no inverted signal is available. The TSPC logic allows to avoid additional inverters that would make the design operate at much lower frequencies. The design does not have any long feedback loop and all the feedback loops are enclosed in the 2/3 cell. Also, the frequency of operation decreases from the left to the right of the chain. This simplifies the layout and eases the effective functionality of the divider at higher frequencies of operation.

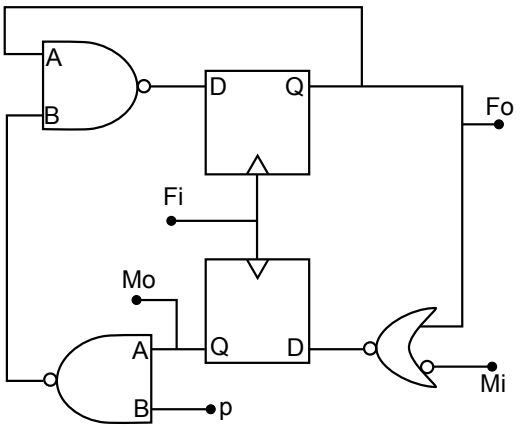


Figure 5.20: Schematic of the 2/3 cell.

### 5.6.8 Coarse Tuning Machine

A coarse tuning machine is necessary to provide a coarse tuning that, based on the desired output frequency, selects the appropriate VCO and VCO capacitor bank control word. As previously shown in Fig. 5.10 at the start-up, the DIVN modulus is set by feeding the FREQ_SELECT 8-bit word to the divider. This defines the desired PLL output frequency. Once the FREQ_SELECT word is selected, the COARSE_START pulse is given to the coarse tuning machine. The coarse tuning machine forces the tune voltage to 600 mV. Consequently, the TO_HIGH_IMP_CP signal goes high and sets the CP in high impedance configuration (all the switches are open). At this point, the coarse tuning machine works to choose the appropriate VCO between $VCO_H$ and $VCO_L$ and the best capacitor bank code. Then, it releases the tune voltage and the CP, and the PLL loop continues in normal operation until analog lock condition is reached.

The coarse tuning machine block diagram is shown in Fig. 5.21. REF and DIV are the signals coming from the external XTAL reference and the DIVN block; CAL_RESET triggers the calibration; INTIAL_VCO sets the VCO from which the calibration starts from; COMP_VAL is the number of periods of the XTAL used to compare how close the REF and DIV signals are; CAP_SEL, VCO_SEL and TO600MV are the digital output signals containing the capacitor bank bit selection, the VCO selection and a signal that unlocks the coarse tuning machine from loop once the calibration is over. The REF and DIV frequency counters count for COMP_VAL periods of the reference signals, accumulating the number of rising edges of the REF and DIV input signals. After COMP_VAL periods, the comparator outputs toggles one of its output signals: if the REF frequency is higher than DIV, REF_FASTER goes high, if the DIV frequency is higher than REF then DIV_FASTER goes high, whereas if DIV and REF have equal frequencies then DIV_REF_EQ goes high. These three signals drive a finite state machine (FSM). The FSM toggles decides which VCO is the right one and select the capacitor bank bit sequence.

To be able to discriminate between two adjacent VCO sub-bands, the frequency counters need to count a minimum number of REF periods $k$. The more the counted periods, the higher the resolution of the coarse tuning machine. As such, the minimum number of periods $k$ needs to be selected based on the closest VCO sub-bands plus some margin. Consequently, a post layout simulation of the two VCOs as a function of the capacitor bank input word was carried out where the tune voltage was set to 600 mV. The result is shown in Fig. 5.22

To properly discriminate between two adjacent sub-bands $f_{VCO1}$ and $f_{VCO2}$, the number of

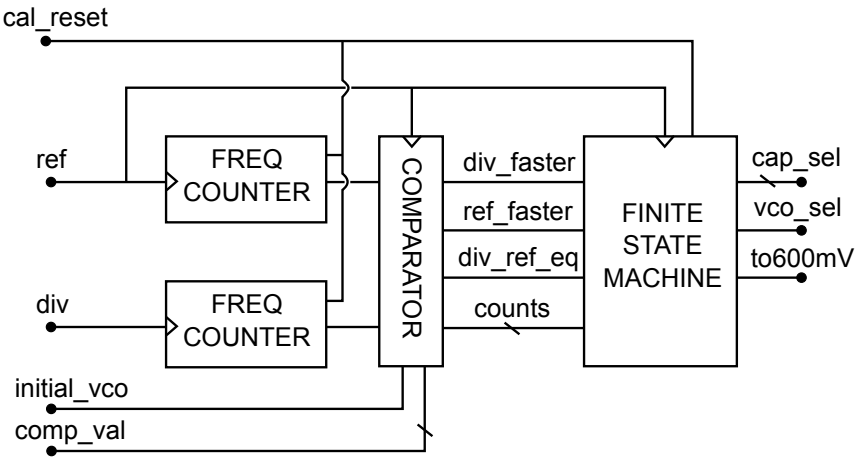


Figure 5.21: Block diagram of the implemented coarse tuning machine.

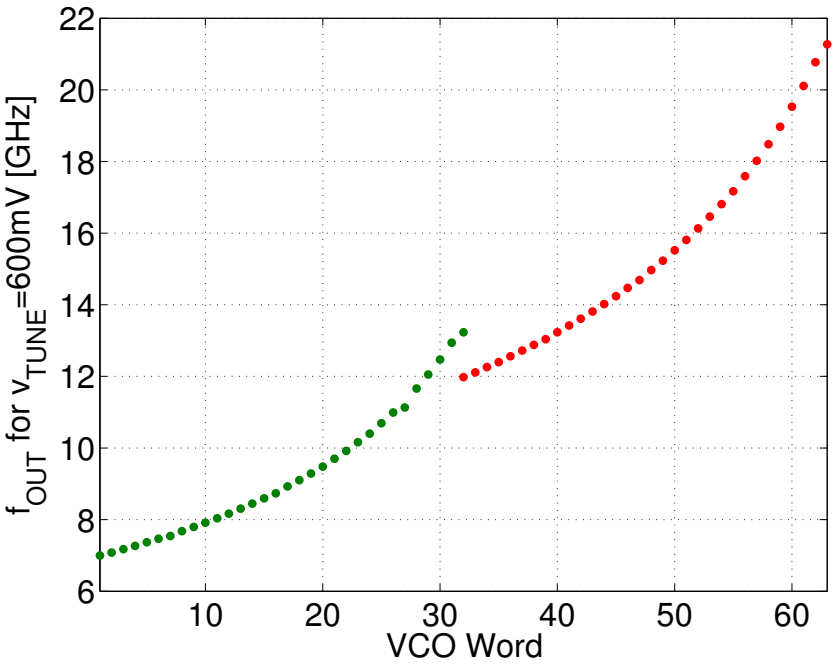


Figure 5.22: Post-layout simulation of the VCOs output frequency as a function of the capacitor bank input word.

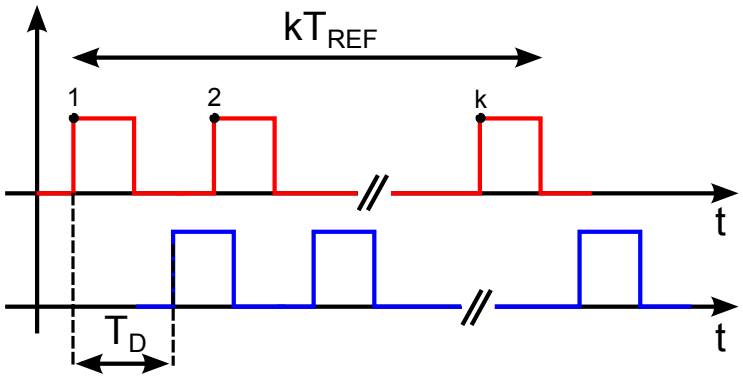


Figure 5.23: Effect of a time delay $T_D$ on the number of counted periods of the DIV and REF signals.

reference periods $k$ needs to be properly chosen. During $kT_{REF}$ periods, the VCO set to the sub-band with frequency $f_{VCO1}$ and $f_{VCO2}$ yield a number of overall frequency counts of

$$\begin{aligned} N_1 &= \frac{kT_{REF}}{4MT_{VCO1}}, \\ N_2 &= \frac{kT_{REF}}{4MT_{VCO2}}, \end{aligned} \tag{5.19}$$

where $M$ is the DIVN modulus for the desired PLL output frequency and 4 represents the operation of the prescaler by 4. To be able to properly discriminate between these two sub-bands, the minimum number of counts $k$ needs to be set such that $|N_2 - N_1| > 1$. Therefore we obtain the condition

$$k > \frac{4M}{T_{REF}} \frac{1}{f_{VCO2} - f_{VCO1}}. \tag{5.20}$$

The minimum number of counts $k$ derived in (5.20) is valid as long as the first rising edge of the DIV signal is aligned to the first rising edge of REF. Of course this is not always true and the first rising edge of the DIV may be late with respect of the first rising edge of the REF by a time $T_D$. In this case, the comparison of two adjacent sub-bands may yield a wrong results, mostly if the REF and DIV signals are close in frequency. The situation, depicted in Fig. 5.23, is equivalent to count for an overall time $kT_{REF} - T_D$ instead of $kT_{REF}$. In the general case, where we have to ensure a minimum number of counts $k^*$ such that $|N_2 - N_1| > 1$ we need to set

$$-\frac{k^* T_{REF} - T_{D1}}{4MT_{VCO1}} + \frac{k^* T_{REF} - T_{D2}}{4MT_{VCO2}} > 1 \tag{5.21}$$

where $T_{D1}$ and $T_{D2}$ are the delay of the rising edge of the DIV signal with respect to the REF signal for the adjacent sub-bands of frequency $f_{VCO1}$ and $f_{VCO2}$. In the worst case, where $T_{D1} = 4MT_{VCO1}$ and $T_{D2} = 0$, the minimum $k^*$ becomes

$$k^* > \frac{4M}{T_{REF}} \frac{1}{f_{VCO2} - f_{VCO1}} + \frac{f_{VCO2} T_{D2} - f_{VCO1} T_{D1}}{T_{REF}(f_{VCO2} - f_{VCO1})} = 2k, \tag{5.22}$$

that translates into a higher requirement of the minimum number of frequency counts. Given the smallest frequency difference between adjacent sub-bands and its corresponding $M$ DIVN

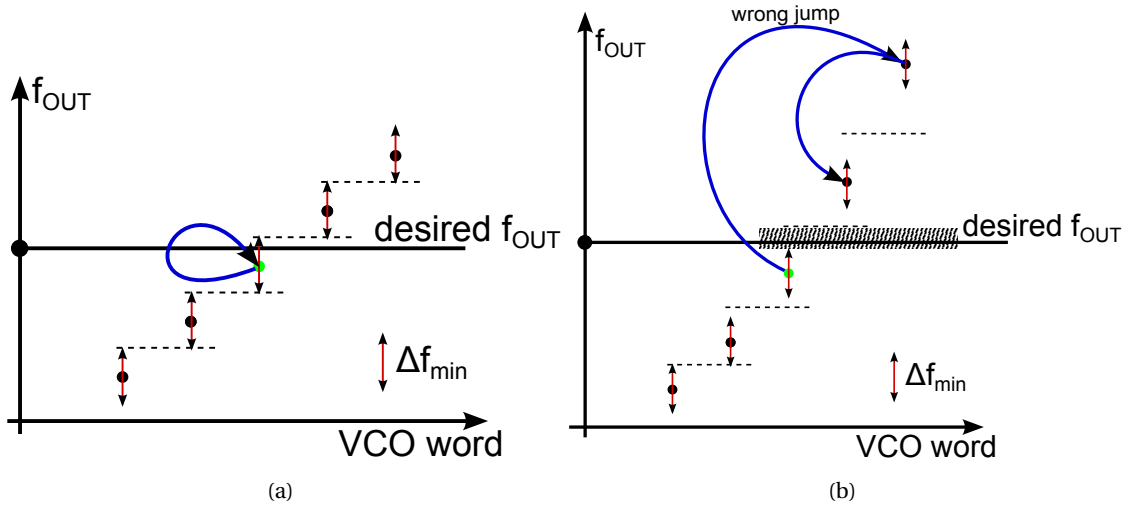


Figure 5.24: Correct operation of the FSM (a) and wrong jump (b) due to the non-linear behavior of the frequency difference between adjacent sub-bands with respect to the input VCO word.

modulus, the minimum $k^*$ for correct operation is about 500.

Another issue related to the coarse tuning is the linearity of the difference in frequency $\Delta f$ between adjacent sub-bands with respect to the input capacitor bank VCO word. As illustrated by Fig. 5.22, $\Delta f$ increases with frequency. Once the desired PLL output frequency is set through the DIVN modulus $M$ and $k^*$ is selected as explained above, the resolution of the algorithm in deciding to jump between different VCO capacitor bank words is $\Delta f_{min}/2$, where $\Delta f_{min}$ is the minimum difference in frequency between adjacent sub-bands. The algorithm implemented by the FSM is a binary search algorithm that starts from the middle of the coarse tuning behavior. The correct operation is shown in Fig. 5.24(a), where the FSM correctly recognizes that the desired output frequency and the currently selected VCO output frequency (the green dot) are below the resolution and hence close enough for the algorithm to converge. Fig. 5.24(b) shows an example where the desired output frequency falls outside the $\Delta f_{min}/2$ region: at the end of $k^*$ reference periods the number of counts of the DIV signal is higher than the one of the REF signal and the FSM does not recognize that the currently selected VCO output frequency (the green dot) is the closest solution to the desired output frequency, making a wrong jump and converging to the wrong VCO word.

To prevent the wrong jump from impairing the correct operation of the coarse tuning machine, at each step of the binary search algorithm, the maximum number of REF periods $\overline{k}$ for the difference between REF and DIV counter to be greater than 1 is recorded together with the corresponding capacitor bank VCO code. When the algorithm converges, the number of counts of the final state $\overline{k}$ is compared to the maximum previously saved. If the latter is greater, then a wrong jump happened and the final state is swapped back to the saved one. In this way, a new method to overcome the non-linear behavior is proposed, particularly useful in PLL where the output frequency range spans a very wide band of frequencies.

A simplified state diagram of the implemented FSM is shown in Fig. 5.25. The FSM is initialized at the state START, where the PLL tune voltage is fixed to 600 mV and the RESET_COUNTERS signal is kept high to prevent the counters from working. In this state, the capacitor bank code is set to the middle of the characteristic show in Fig. 5.22. The next 5 states are waiting states, where the

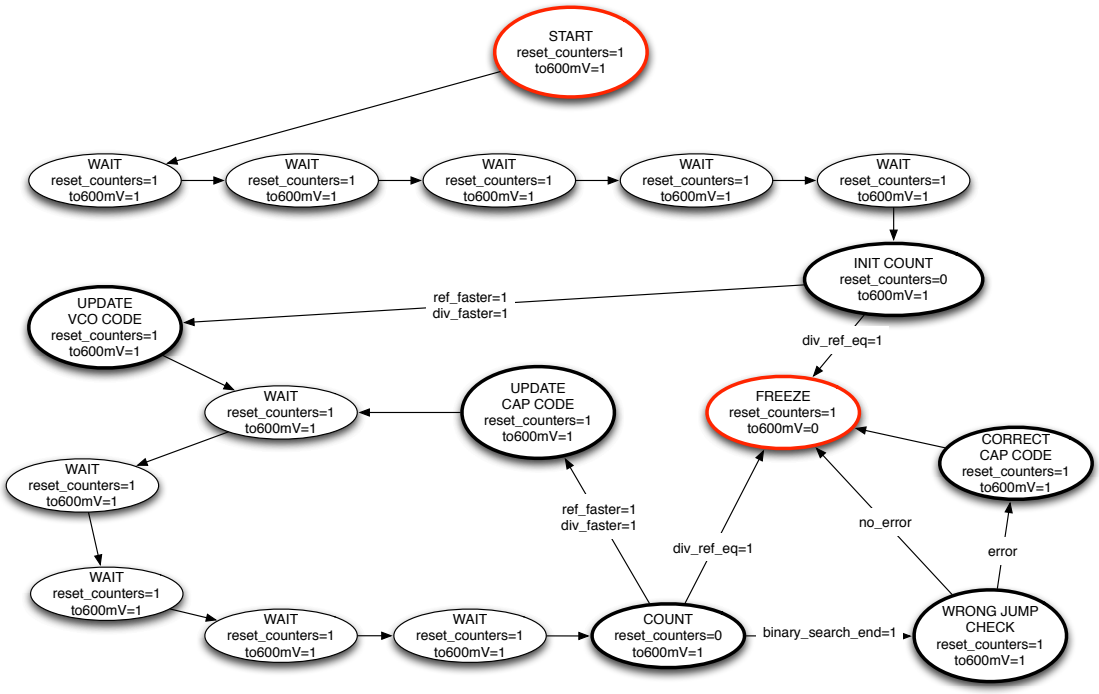


Figure 5.25: State diagram of the implemented finite state machine.

FSM waits for the output of the PLL to be stable. In the INIT_COUNT state, the counters count $k^*$ periods of the reference signal: if the PLL output frequency is correct, the DIV_REF_EQ goes high and the FREEZE is selected, where the counters sleep and the PLL tune voltage is released. Otherwise, the correct VCO bit is selected and the FSM wait 5 reference periods before reaching the state COUNT. The COUNT state first checks if the current VCO word is at the end of the binary search tree. If it is the case, the WRONG_JUMP_CHECK state is selected. If the final state is the correct one, the FSM toggles to the FREEZE state, otherwise the VCO word is corrected before freezing. If the current state is not at the end of the binary search tree, the COUNT state looks at the REF_FASTER, DIV_FASTER and DIV_REF_EQ signals. If the DIV_REF_EQ is high, the FSM toggles to the freeze state; whereas if REF_FASTER or DIV_FASTER are high the VCO capacitor bank word is updated and the FSM loops back to the WAIT states to proceed with the VCO capacitor bank word search.

## 5.7 Measurements

The integer-N PLL frequency synthesizer has been implemented in 65 nm CMOS technology. A microphotograph of the chip containing the PLL structure is shown in Fig. 5.26. The PLL was measured as part of the microwave transceiver for breast cancer imaging. In the realized transceiver, the PLL drives a divider by 1, 2 or 4 and an output buffer that was probed for testing. The PLL was measured using Agilent E4407B spectrum analyzer after it was mounted on a test board realized over a FR-4 substrate and all but the RF pads were bonded. The length of the bonding wire was made as short as possible for minimizing the impedance attenuating the power lines of the PLL. An external crystal provides the reference frequency $f_{REF}$ of 22.5792 MHz.

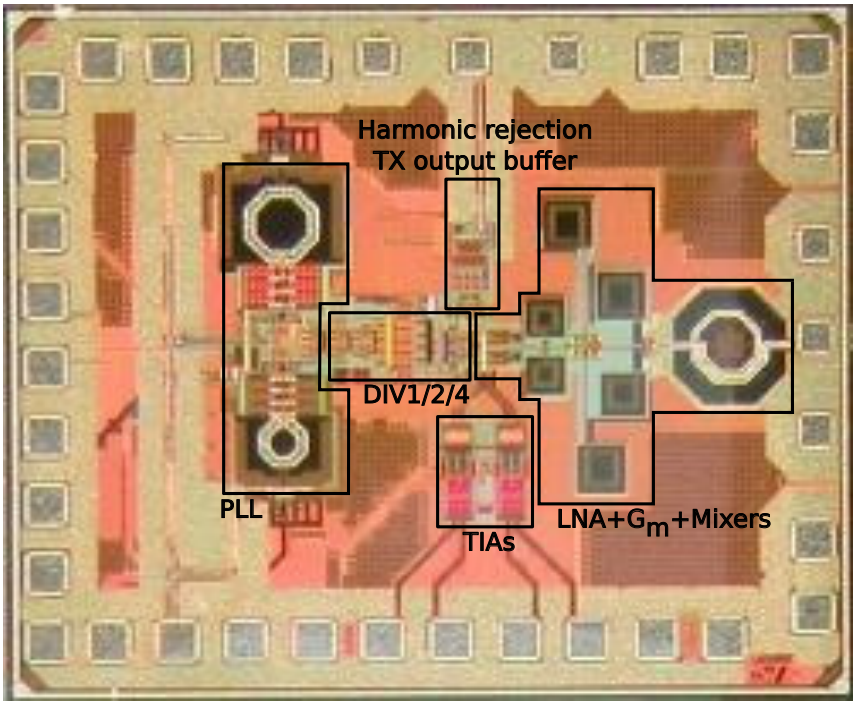


Figure 5.26: A microphotograph of the implemented radar transceiver, including the sideband integer-N PLL frequency synthesizer.

The PLL consumes a total of 46 mW in the worst case. The $VCO_H$ consumes 40 mW, the $VCO_L$ 30 mW, the prescaler by 4 3 mW while the programmable divider, PFD and CP 3 mW, which is in good agreement with the simulations.

Fig. 5.27 shows the measured tuning range of the $VCO_H$ and $VCO_L$. The two VCOs tune from 6.5 to 11.8 GHz, and from 11 to 18.4 GHz, covering the desired frequency range with some additional margin. The fractional tuning range is defined as $100(f_{max} - f_{min})/f_{cen}$, where $f_{max}$ and $f_{min}$ are the maximum and minimum frequency of operation and $f_{cen} = f_{min} + (f_{max} - f_{min})/2$. The measured fractional tuning range is therefore 95.6%.

Fig. 5.28 shows the phase noise measured with the aid of Agilent E4407B spectrum analyzer of two stand-alone VCOs at 10 MHz offset. The phase noise at 1MHz offset is always <-109 dBc/Hz in the frequency range of interest. Fig. 5.29 shows the phase noise from a 9 and 13 GHz locked carrier, generated from $VCO_H$ and $VCO_L$, respectively. The phase noise of the 9 GHz carrier is -95 dBc/Hz at 200 kHz offset and -131 dBc/Hz at 10 MHz offset. The phase noise of the 13 GHz carrier is -90 dBc/Hz at 200 kHz offset and -129 dBc/Hz at 10 MHz offset. The RMS jitter integrated from 1 kHz to 100 MHz is 0.68 ps (2.2°) and 0.52 ps (2.4°) for the carrier at 9 and 13 GHz, respectively. The RMS integrated jitter is lower at 13 GHz because of the reduced loop bandwidth due to the decreased $k_{VCO}$ at 13 GHz.

An example of the output power spectrum at 12.7 GHz is reported in Fig. 5.30. The reference spur level is better than -48 dBc.

The transient of the tune voltage is shown in Fig. 5.31. The PLL reaches lock condition in approximately 2 $\mu$s. The PLL output frequency is 12.7 GHz.

Table 5.7, reports a performance comparison of recently published PLL circuits. In terms of

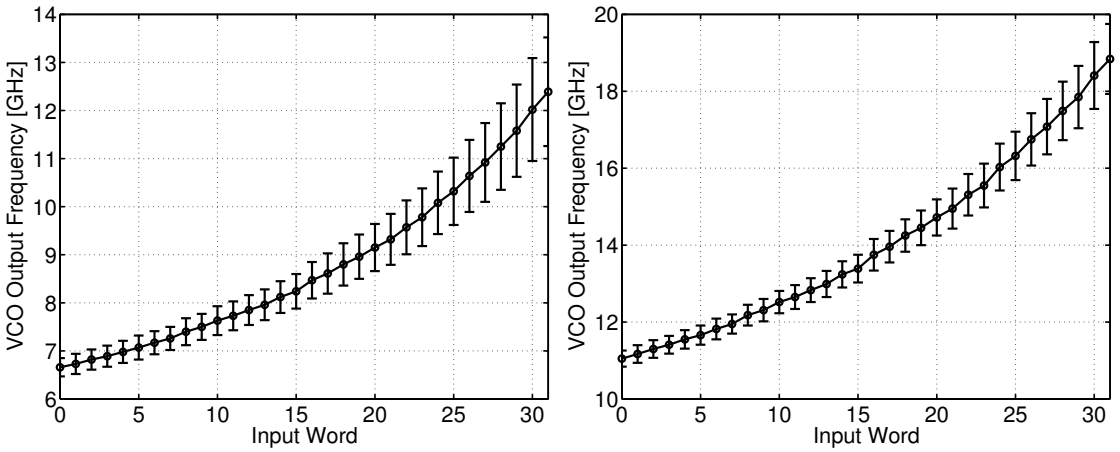


(a) (b)

Figure 5.27: Measured tuning range of $VCO_L$ and $VCO_H$.

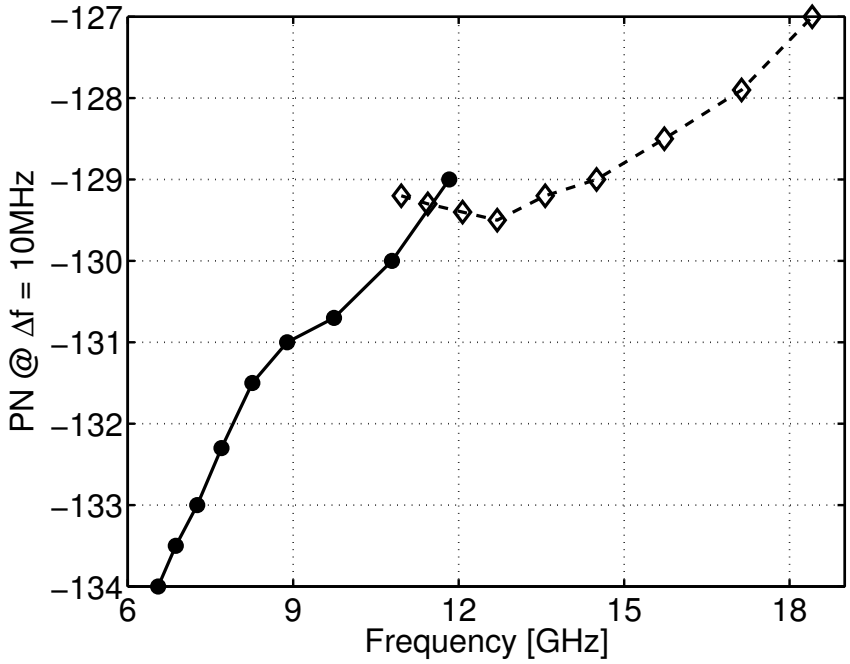


Figure 5.28: Measured phase noise of $VCO_L$ and $VCO_H$ at 10 MHz offset from the carrier.

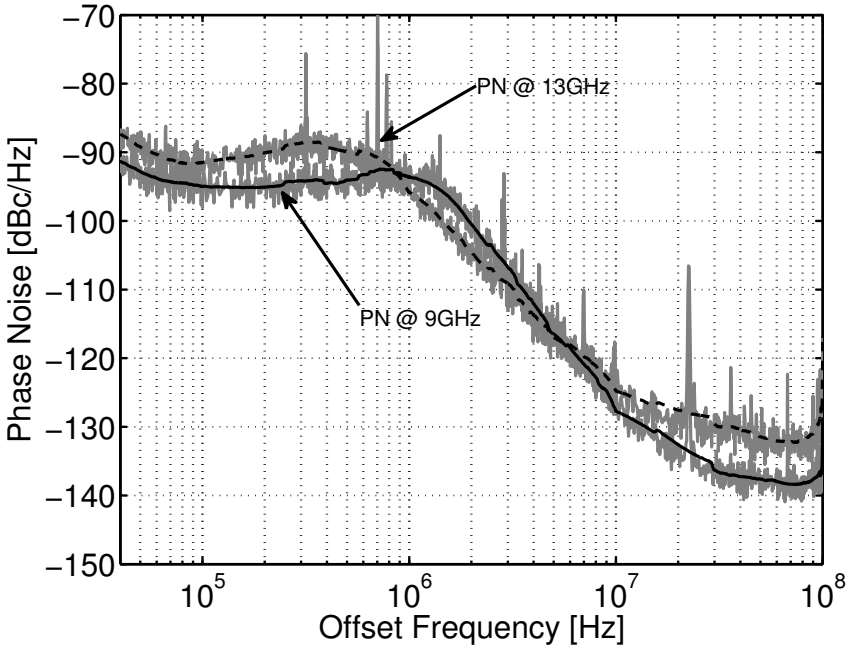


Figure 5.29: Measured phase noise of the PLL from a 9 and 13 GHz locked carrier.

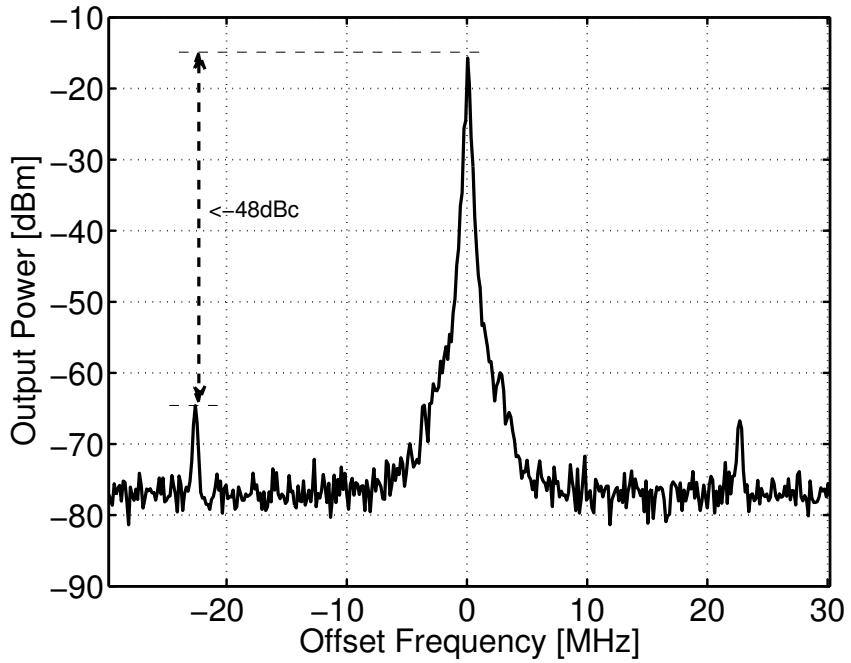


Figure 5.30: Measured PLL output spectrum at 12.7 GHz.

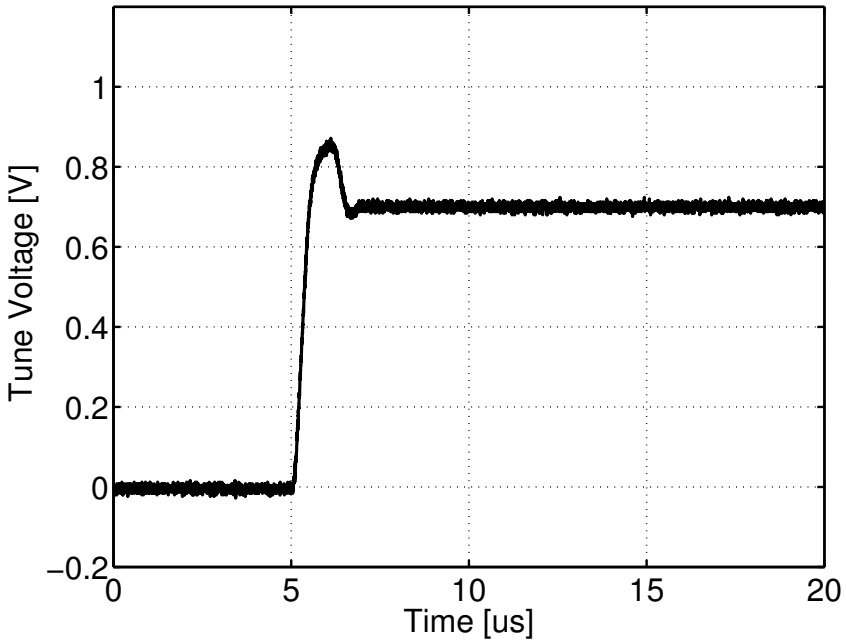


Figure 5.31: Measured PLL transient tune voltage.

fractional tuning range, the presented PLL shows a state-of-the-art performance, overtaken only by [78] that however shows a much higher integrated RMS jitter. The phase noise and its integrated quantities show values comparable to the other reported works, while still consuming only 46 mW.

| | This Work | [79] | [80] | [81] | [82] | [83] | [84] | [85] | [78] |
|---|---|---|---|---|---|---|---|---|---|
| Technology | 65 nm CMOS | 45 nm CMOS SOI | 45 nm CMOS digital | 0.25 $\mu$m SiGe:C BiCMOS | 0.25um SiGe:C BiCMOS | 65nm CMOS | 0.13 $\mu$m SiGe:C BiCMOS | 45 nm CMOS | 0.13 $\mu$m CMOS |
| Type | Analog | Analog | Digital | Analog | Analog | Analog | Analog | Analog | Analog |
| Freq. [GHz] | 6.5-18.4 GHz | 7.3-17.5 GHz | 5.5-12 GHz | 14.25-16 GHz | 20-28 GHz | 19.5-20.94 GHz | 15-18 GHz | 21.7-27.8 GHz | 0.05-10 GHz[1] |
| BW | 1 MHz | 9.5 MHz | 0.2-2 MHz | 3 MHz | 100-200 kHz | - | 2 MHz | 1 MHz | - |
| Frac. TR | 95.6% | 82% | 74% | 11% | 33% | - | 18% | 24.6% | 198% |
| Spurs | <-48 dBc | <-50 dBc | <-48 dBc | <-42 dBc | - | <-50 dBc | <-60 dBc | <-40 dBc | - |
| Phase Noise In-Band [dBc/Hz] | -93 @ 200 kHz ($f_c$=9 GHz)<br>-87 @ 200 kHz ($f_c$=13 GHz) | -104 @ 1 MHz ($f_c$=7.3 GHz)<br>-93 @ 1 MHz ($f_c$=17.5 GHz) | -90 ($f_c$=7 GHz)<br>-104 @ 1 MHz ($f_c$=12 GHz) | -87 @ 600 kHz ($f_c$=16 GHz) | -80 ($f_c$=24 GHz) | -55 ($f_c$=20.88 GHz) | -90<br>- | -88 ($f_c$=23.32 GHz) | -85 ($f_c$=10 GHz)<br>-78 ($f_c$=19 GHz) |
| Phase Noise Out-of-Band [dBc/Hz] | -131 @ 10MHz ($f_c$=9 GHz)<br>129 @ 10MHz ($f_c$=13 GHz) | -<br>- | -138 @ 10MHz ($f_c$=7 GHz) | -107 @ 10 MHz ($f_c$=16 GHz) | -122 @ 10 MHz ($f_c$=24 GHz) | -124 @ 10 MHz ($f_c$=20.88 GHz) | -123 @ 10 MHz ($f_c$=17.14 GHz) | -124 @ 10 MHz ($f_c$=23.32 GHz)<br>-120 @ 10 MHz | -122 @ 10 MHz ($f_c$=10 GHz)<br>($f_c$=19 GHz) |
| RMS Jitter | 0.68 ps ($f_c$=9 GHz)<br>0.52 ps ($f_c$=13 GHz) | 1.96 ps ($f_c$=9.93 GHz) | 0.56 ps ($f_c$=7 GHz) | - | 0.38 ps ($f_c$=7 GHz) | - | 0.17 ps[2] | 0.31 ps ($f_c$=23 GHz) | 1.3 ps ($f_c$=10 GHz)<br>1.1 ps ($f_c$=19 GHz) |
| Power | 46 mW | 32 mW | 30 mW | 287 mW | 680 mW | 80 mW | 145 mW | 40 mW | 80 mW |

Table 5.3: Performance comparison of recently published PLL circuits.

[1] Additional outputs at 19-22 GHz and 38-44 GHz through x2 and x3

[2] From 1 MHz-1 GHz integration

## 5.8 Conclusions

The chapter presents an analog integer-*N* PLL able to generate carriers in the wide frequency range of 6.5-18.4 GHz. The PLL consumes a 46 mW from a 1.2 V supply with a maximum integrated RMS jitter of 0.8 ps at 13 GHz. The spurs level is always better than -48 dBc. These performances enable the PLL to be effectively used as a frequency synthesizer in a microwave imaging transceiver front-end for breast cancer diagnostic imaging.

# Experiments Part III

# 6 Imaging Experiments

The realized microwave radar front-end transceiver is proposed together with a pair of patch antennas as a basic module for an imaging antenna array. To demonstrate the capabilities of the proposed imaging module structure, several imaging experiments are presented. Further, a realistic breast phantom mimicking the electric properties of a real breast is implemented to show that the system is effectively capable of detecting two tumor enclosures buried inside the breast. The experimental results show that the system is capable of achieving a resolution of 3 mm inside the human body, clearly showing that the proposed system can replace commercial laboratory equipment with advantages in terms of performance, size, and cost of the imaging setup [86, 87].

The chapter is organized as follows. In Section 6.1, the key features and electrical performances of the proposed microwave radar transceiver front-end are summarized. Section 6.2 reports the design of the wideband patch antenna used in the imaging experiments, detailed out in Section 6.4.

## 6.1 Radar Transceiver

The measured electrical performances of the stand alone receiver (i.e. SKuRAD1) and the complete transceiver (i.e. SKuRAD2) are reported in detail in Chapter 4 and 5, respectively. However, it is worth to note that compared to the results presented in Chapter 4, SKuRAD2 shows a higher conversion gain and a more efficient injection-locked programmable divider by 1, 2 or 4 chain.

The proposed integrated radar transceiver was fabricated in 65 nm CMOS technology. A microphotograph of the SKuRAD2 chip is shown in Fig. 5.26. The occupied area is 1.3 by 1 $mm^2$ including the pads. The overall power consumption is 203 mW from a 1.2 V supply.

The measured key features are summarized in Tab. 6.1. The receiver input matching is lower than -9 dB over the entire 2-16 GHz bandwidth. The receiver conversion gain and average noise figure are 36 dB and 7 dB, respectively. The 1/f noise corner is 30 Hz, showing the effectiveness of the chopper-stabilized TIA. The input-referred 1 dB compression point is larger than -29 dBm, the IIP3 larger than -13 dBm, and the IIP2, as measured over 7 samples, larger than 22 dBm

Table 6.1: Transceiver performance summary.

| RX Performance | | TX Performance | |
|---|---|---|---|
| Conversion Gain | 36 dB | Output Power | -14 dBm |
| Bandwidth | 2-16 GHz | Harmonic Rejection | > 40 dBc |
| Input Match | < -9 dB | Phase Noise at 10 MHz Offset | < -129 dBc/Hz |
| Average Noise Figure | 7 dB | RMS Jitter | < 680 fs |
| 1/f Noise Corner Frequency | 30 Hz | | |
| $P_{1dB}$ | > -29 dBm | | |
| IIP3 | > -13 dBm | | |
| IIP2 | > 22 dBm | | |
| I/Q Phase Mismatch | < 1.5° | | |

(median value is 30 dBm). The I/Q phase mismatch, measured over 7 samples, is lower than 1.5° over frequency. The two VCOs tune from 6.5 to 11.8 GHz and from 11.0 to 18.4 GHz, effectively covering the higher octave of operation. The phase noise at 10 MHz offset from the carrier is lower than -129 dBc/Hz, while the RMS jitter is lower than 680 fs.

Additionally, Fig. 6.1 shows the harmonic rejection performance of the TX output buffer. The transmitter average output power is -14 dBm, and the harmonic rejection is in excess to 40 dBc, except for the 4th harmonic, which is however intrinsically rejected by the RX by 48dBc (measured).

Based on the electrical measurements, the proposed SFCW CMOS radar consistently achieves a dynamic range in excess of 107 dB over more than 3 octaves, while the 14 GHz bandwidth allows to resolve a tumor with 3 mm resolution. This performance enables the radar transceiver to be effectively employed as a breast cancer imaging diagnostic tool.

## 6.2 Antenna Design

The design of the antenna structure that complements the integrated radar transceiver is fundamental to assess its functionality as an effective imaging system. Three different antennas were developed. They are all based on planar monopoles antenna structures, typically used in UWB applications. According to the operation principle of these family of antennas [88], it is known that the small feature dimension contributes to the high resonant frequency, whereas the large dimension contributes to the low resonant frequency. As it will be shown in the following, these guidelines are used to extend the bandwidth and the performance of the antenna on the broad desired frequency range.

The design of the first antenna is inspired to the planar inverted cone antenna (PICA), that provides UWB performance with a radiation pattern similar to monopole disk antennas. The antenna, named SMILING PICA can be thought as a single planar element mounted above a ground plane, as shown in Fig. 6.2. The 50 Ω feed is slightly tapered to provide better matching to the semicircular radiating planar structure. The vertical dimension of the main structure (F2+F3/2) is set to $\lambda_L/4$, where $\lambda_L$ is the wavelength of the lowest desired frequency of operation. As suggested by the literature, a semicircular opening in the center of the antenna provides

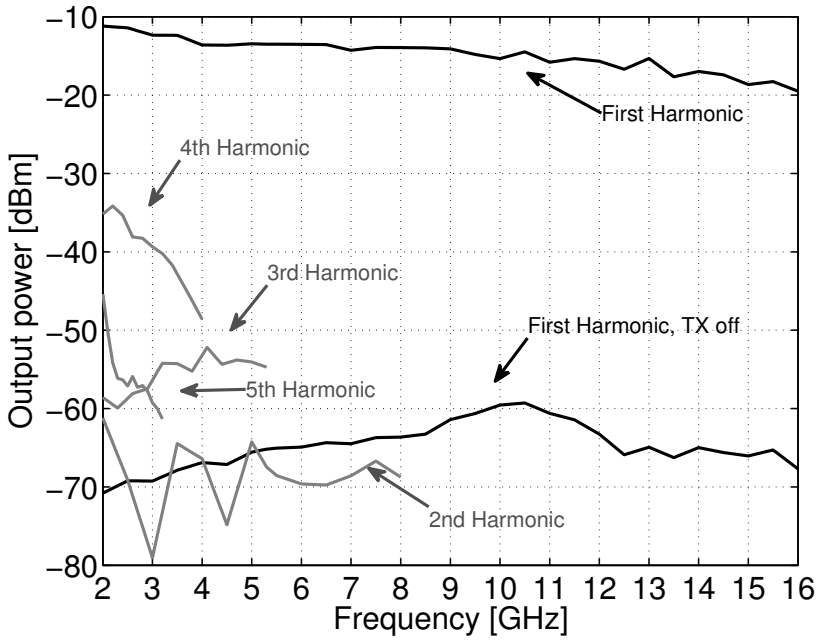


Figure 6.1: Measured TX performance: 1st harmonic output power and harmonic rejection performance (frequency refers to fundamental tone; higher harmonics measured when in-band).

better radiation pattern at high frequency while not impairing the impedance matching [89]. The ground plane on the back of the antenna is limited to the length of the feed not to reduce the radiating capabilities at high frequency. The optimization of all the parameters was performed through simulation employing Ansys HFSS software.

The second design of the antenna is based on the miniaturization principle presented in [90]. The design is based on a circular disc monopole and a 50 Ω tapered microstrip feed line. On the back, a conducting ground plane only covers the section of the microstrip feed line. This symmetrical structure contains all the necessary dimension features for the resonant frequencies. The miniaturized half-structure of the symmetrical circular monopole is show in Fig. 6.3. From its shape it was named AX ANTENNA. It can achieve similar bandwidth and performances of the full-size version while up to 40% of the area can be saved by the miniaturization process, which greatly advantages the antenna to be further integrated. The antenna also contains a small half circular element to produce a high-frequency resonance that improves the matching and radiation pattern.

Prototypes of the SMILING PICA and AX antennas were realized on FR4 substrate with a thickness of 1.8 mm, that typically has a $\epsilon_r$ of 4.7 and a loss tangent of 0.018. The antennas were experimentally characterized by using a two-port Agilent N5320A PNA-L vector network analyzer. The measured and simulated input reflection coefficient is shown in Fig. 6.4. Generally, the antennas are well matched and the simulations are in good agreement with the measurements for frequencies below 8 and 4 GHz for the SMILING PICA and AX antenna, respectively.

Based on the design of the previous two antennas, a final version was realized by the EM group at the Department of Information Engineering, University of Padova. The requirement for each antenna element of operating on the large wideband from 2 to 16 GHz is achieved by means of a combined circular/rectangular shape of the radiating patches, as shown in Fig. 6.5(a). In

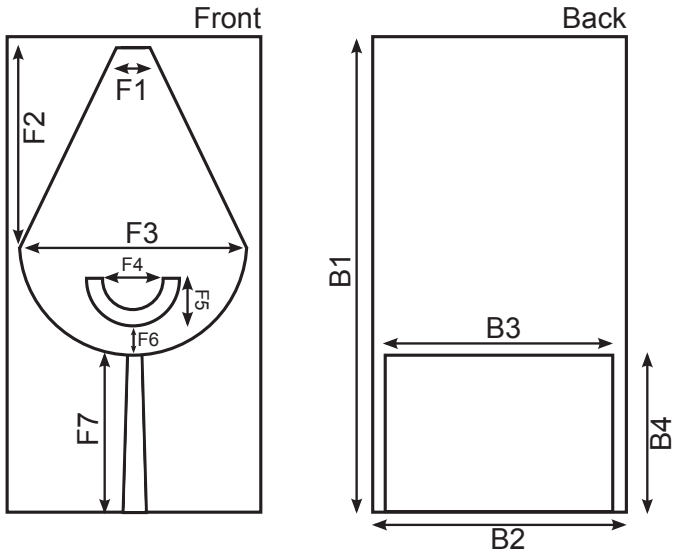


Figure 6.2: Layout of the SMILING PICA antenna structure. Dimensions are: $F1 = 8.4\,\text{mm}$, $F2 = 25\,\text{mm}$, $F3 = 30\,\text{mm}$, $F4 = 8.65\,\text{mm}$, $F5 = 5.35\,\text{mm}$, $F6 = 2\,\text{mm}$, $F7 = 20\,\text{mm}$, $B1 = 70\,\text{mm}$, $B2 = 30\,\text{mm}$, $B3 = 28.5\,\text{mm}$, $B4 = 21.3\,\text{mm}$.

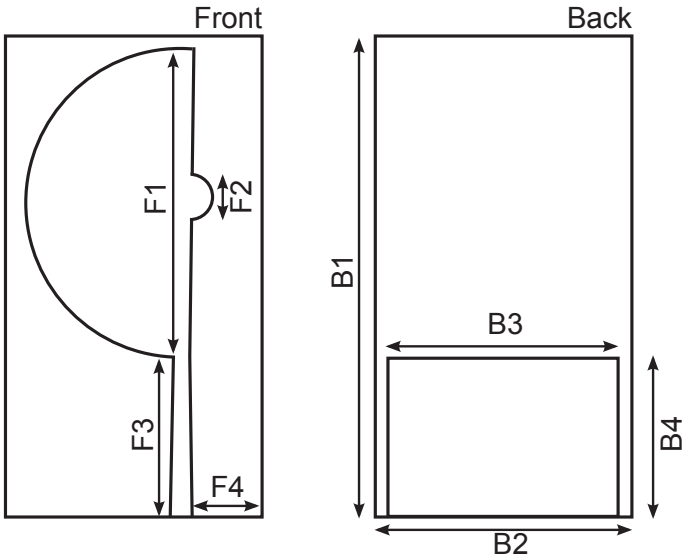


Figure 6.3: Layout of the AX antenna structure. Dimensions are: $F1 = 40\,\text{mm}$, $F2 = 6\,\text{mm}$, $F3 = 20\,\text{mm}$, $F4 = 7\,\text{mm}$, $B1 = 63\,\text{mm}$, $B2 = 36\,\text{mm}$, $B3 = 30\,\text{mm}$, $B4 = 20\,\text{mm}$.

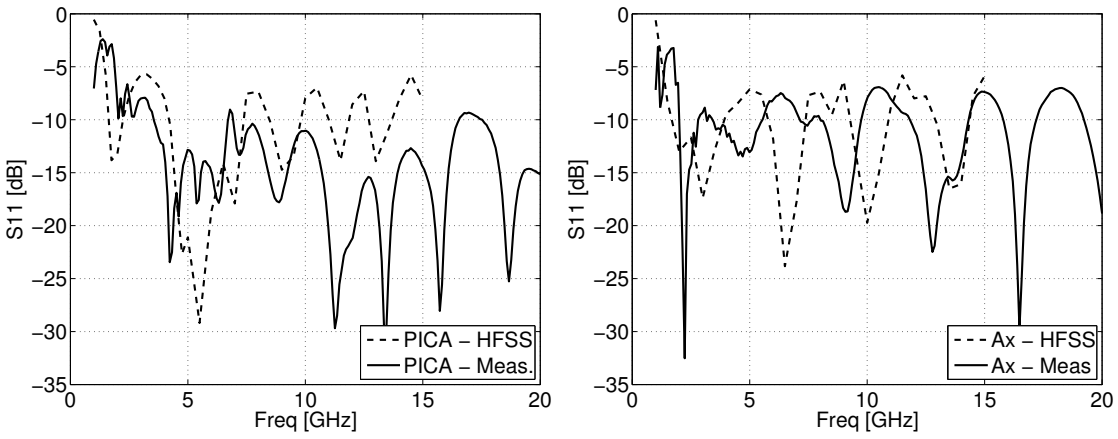


(a) (b)

Figure 6.4: Simulated and measured input reflection coefficient for the realized SMILING PICA (a) and AX antenna (b).

particular, the semi-circular part acts as a tapering section for better impedance matching all over the bandwidth to the 50 Ω microstrip feeding line. In order to obtain a compact design, the two monopoles are placed very close to each other on the same face of the substrate. To minimize the unavoidable mutual coupling between the antennas, a T-shaped decoupling structure is introduced on the back of the laminate, as shown in Fig. 6.5(b). The geometric parameters $wd_1$ and $ld_1$ control the isolation between the two radiating patches in the lower part of the operating band, namely from 2 to 9 GHz, while the geometric parameters $wd_2$ and $ld_2$ control the isolation in the upper part of the spectrum, for frequencies higher than 9 GHz. Optimization of all the parameters was performed through simulation employing the CST Microwave Studio software.

A prototype of the antenna is shown in Fig. 6.6. The prototype was fabricated on a Roger RO4003c laminate, featuring a thickness of 1.524 mm, a dielectric constant of 3.55 and a loss tangent of 0.0027.

The antenna structure was experimentally characterized by using a two-port Agilent N5230A PNA-L network analyzer. The measured reflection and transmission coefficients of the two-element antenna are shown in Fig. 6.7, and compared to simulation results. The agreement between measurement and simulation is very good for frequencies below 8.5 GHz, while at higher frequencies discrepancies due to soldering and fabrication imperfections are clearly visible. In any case, the measured input matching is lower than -10 dB over the entire frequency range of operation with the exception of a small hump at 2.9 GHz ($|S_{11}| = -5$ dB). Moreover, the antenna-to-antenna isolation is greater than 20 dB for frequencies higher than 3.3 GHz, a performance that allows to directly connect the antenna structure to the integrated transceiver. Alternatively, a single antenna could also be used. However, in this case a directional coupler or a circulator would be needed to interface the radiating element to the transceiver.

The simulated antenna radiation pattern on the magnetic plane ($x$-$z$ plane in Fig. 6.5), that is the plane facing the illuminated target, is shown in Fig. 6.8 for several frequencies. The radiation pattern is fairly omnidirectional, as required by the operation of the antenna within the array.

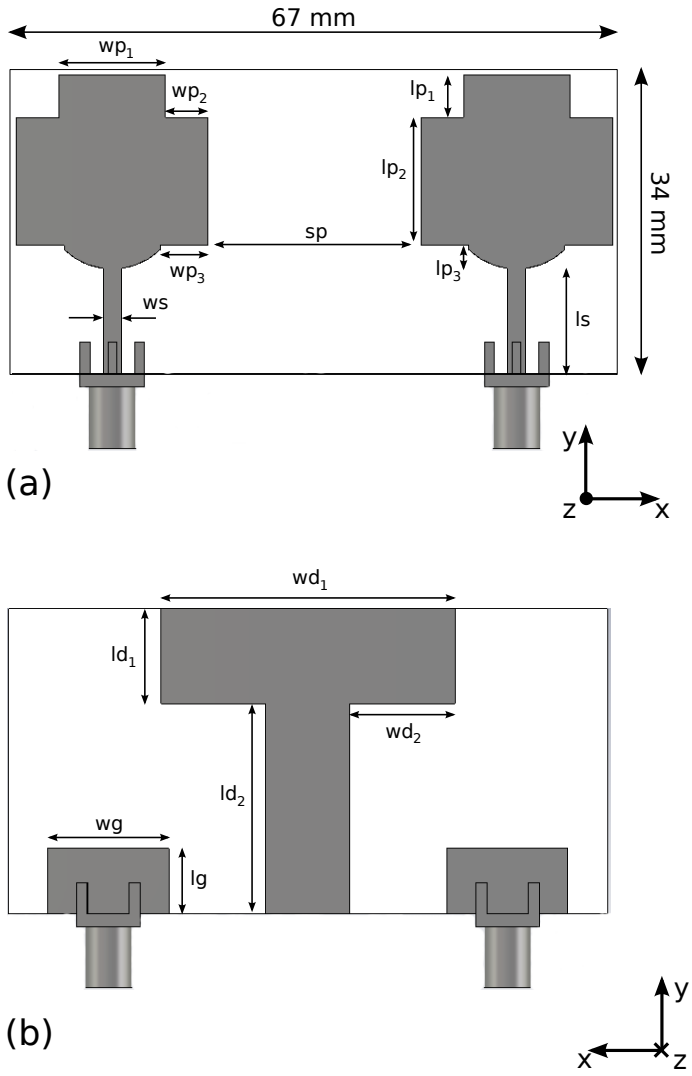


Figure 6.5: Layout of the antenna structure. (a) Top layer with transmitting and receiving radiating elements. (b) Bottom layer with decoupling structure and partial ground plane. Dimensions are: $wp_1 = 10\,\text{mm}$, $wp_2 = 4\,\text{mm}$, $wp_3 = 4\,\text{mm}$, $lp_1 = 4\,\text{mm}$, $lp_2 = 12\,\text{mm}$, $lp_3 = 2.1\,\text{mm}$, $ws = 1.7\,\text{mm}$, $ls = 9.9\,\text{mm}$, $sp = 20\,\text{mm}$, $wg = 11.5\,\text{mm}$, $lg = 6.25\,\text{mm}$, $wd_1 = 28\,\text{mm}$, $wd_2 = 10\,\text{mm}$, $ld_1 = 9\,\text{mm}$, $ld_2 = 20\,\text{mm}$.

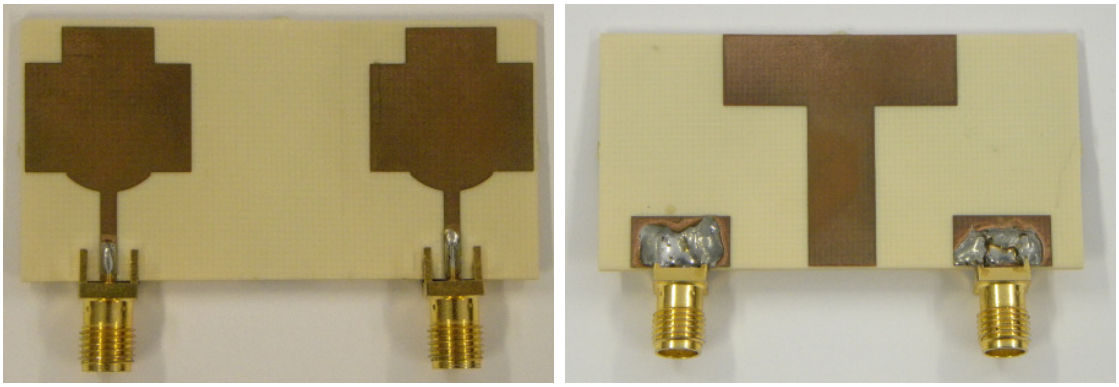

(a) (b)

Figure 6.6: Photograph of the prototype of the antenna structure. (a): Top layer. (b): Bottom layer.

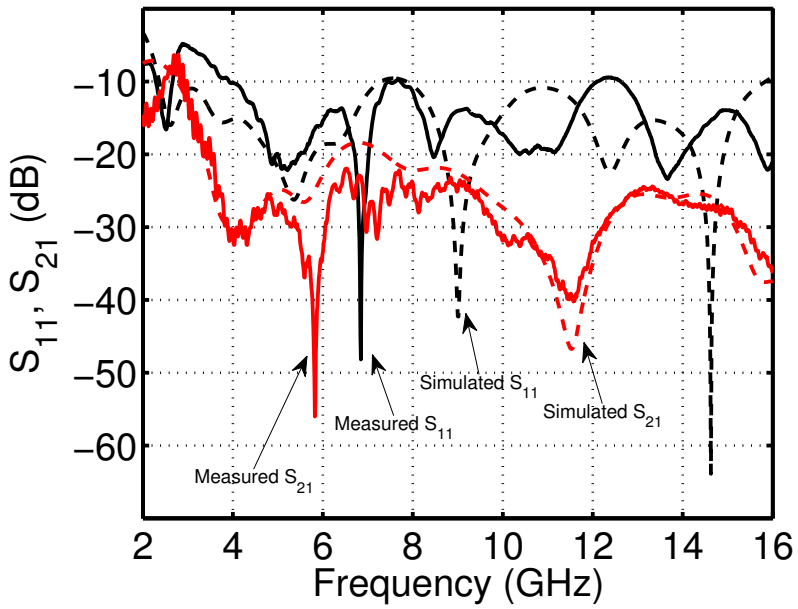


Figure 6.7: Simulated and measured magnitude of reflection ($S_{11}$) of transmission ($S_{21}$) coefficients.

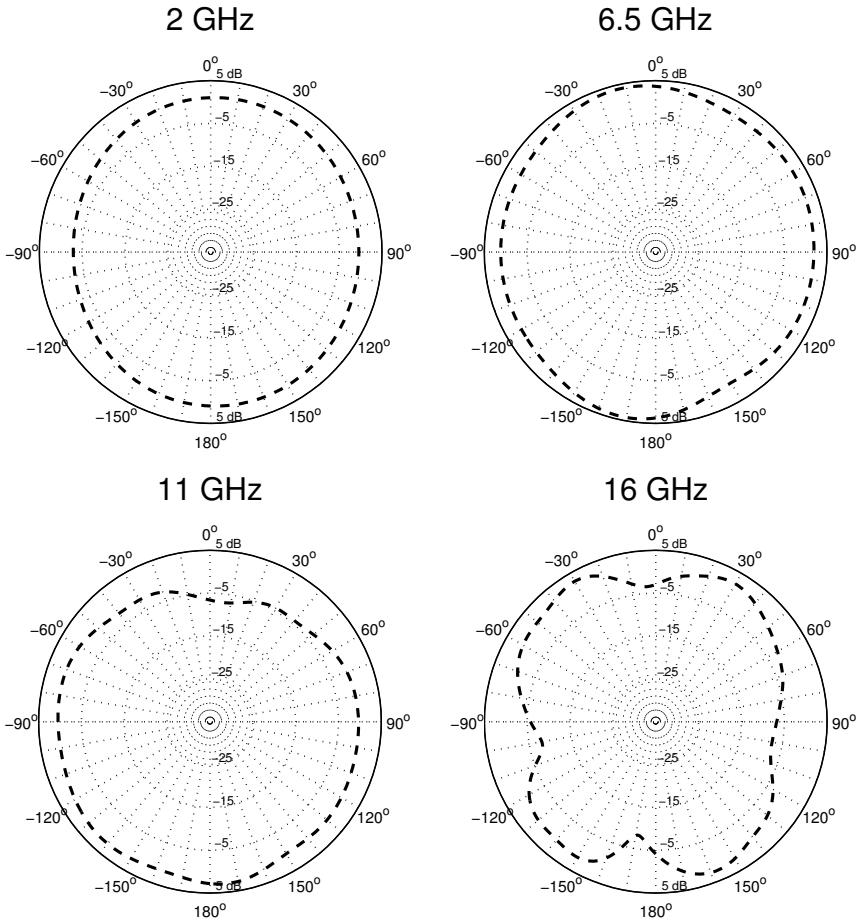


Figure 6.8: Simulated antenna radiation pattern on the $x$-$z$ plane (cf. Fig. 6.5).

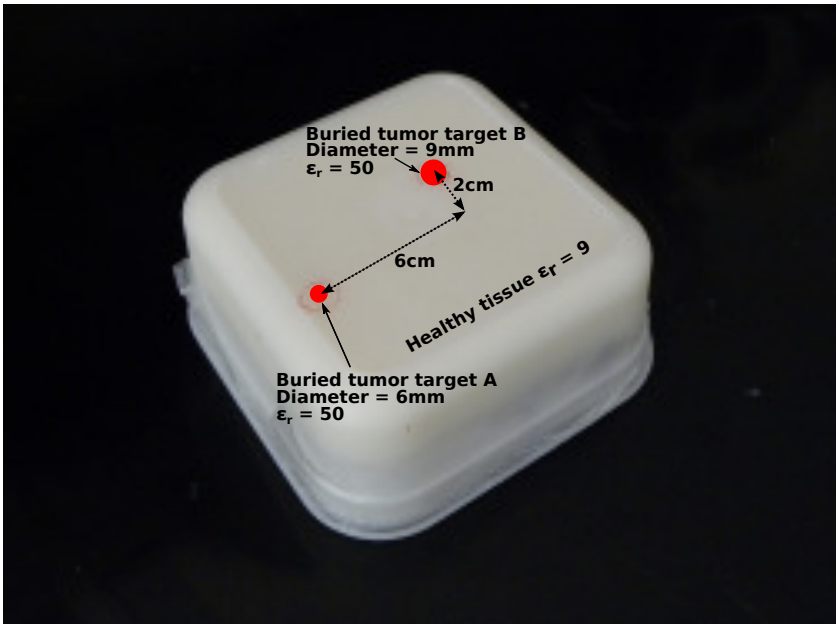


Figure 6.9: Photograph of the implemented breast phantom.

## 6.3 Physical Breast Phantom

Microwave imaging for breast cancer detection seeks to identify the presence and location of relevant tumor targets [5]. Accordingly, a physical breast phantom is realized to conduct experiments on breast cancer detection. The recipe is based on the work presented in [59].

The phantom mimics the electrical properties of the breast tissues and tumors over a wide range of frequencies. It is mainly based on glycerin, that provides moisture leading to less water evaporation allowing the phantom to retain its dielectric properties for a long time - even for six months if wrapped in a vinyl/plastic film. Also, it can retain the shape and it is minimally prone to the formation of lumps [59]. A non-toxic bactericide can be used to prevent the breakdown of the polymer by bacterial agents.

The material modeling the healthy tissue is a mixture of glycerin, double distilled/de-ionized water, ethylene glycol, polyethelene powder, and agar [59]. The recipe is easy to make, consistent, accurate and has been extensively tested over more than two years [59]. Of course the realized phantom cannot exactly trace the dispersive properties of living tissues. Its purpose is to offer a consistent and reliable contrasts of dielectric properties among tissue groups. To complete the scenario, two enclosures of different diameters filled with tap water are buried inside the breast, mimicking two tumor targets.

The resulting physical breast phantom is shown in Fig. 6.9. The dimensions are approximately 11x11x3 cm and it can be fully contained in a plastic tupperware. To prevent the formation of air bubbles, it was deposited while still liquid and properly mixed to eliminate all the lumps. The phantom lasted several weeks without showing any sign of bacterial infection.

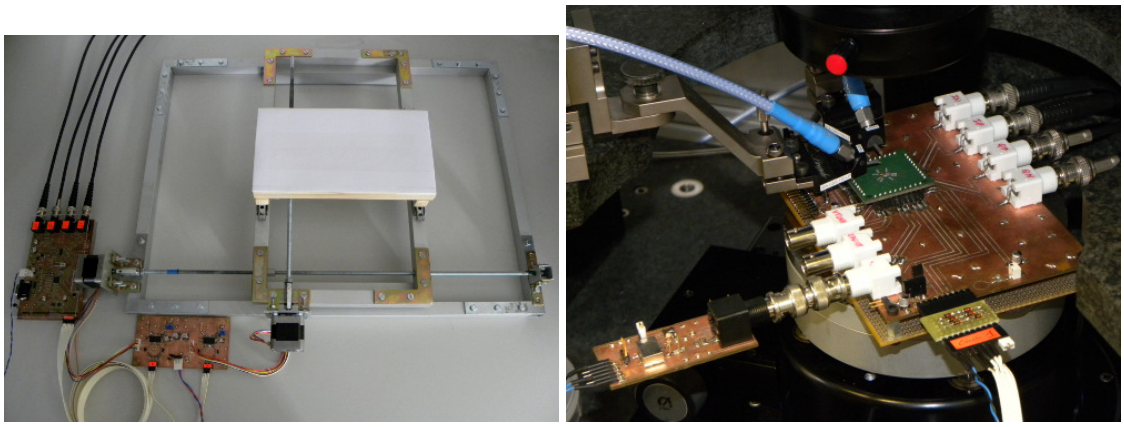

(a) (b)

Figure 6.10: Photograph of the measurement setup: (a) Custom metal frame, along with the acquisition PCB, and the motor control board. (b) Chip-on-board assembly of the integrated transceiver housed in the probe station.

## 6.4 Imaging Results

Several tests have been carried out to asses the functionality of the presented integrated radar transceiver and the planar antenna structure as an effective imaging tool. Based on the shape of the employed antenna array, three different imaging setups are available, as detailed out in Chapter 1. A planar antenna array configuration is chosen to arrange a proof-of-concept testbed for the imaging capabilities of the presented microwave radar. Compared to the hemispherical or cylindrical configuration, the planar one allows an easy and fast mechanical reconfiguration of the number of antennas and mutual distance, such that the array behavior can be synthetically obtained by moving a single imaging element to all the desired antenna locations. To further ease the testing, an approach similar to inverse synthetic array radar (ISAR) is used: the antenna position is fixed while the target is moved over all the desired positions [26].

The target is placed on a wood plane support, moved by high-precision stepped motors over a custom metal frame (cf. Fig. 6.10). The planar antennas are installed on a rigid support over the frame. The CMOS transceiver is assembled in chip-on-board fashion (cf. Fig. 6.10(b)): all the pads are directly bonded to a PCB with the exception of the RF pads which are probed. More advanced packaging options can be employed in future developments of the system to yield a more compact assembly. In particular, the direct mounting of the transceiver chip on the antenna board can be envisioned. An acquisition PCB (cf. Fig. 6.10(a)), featuring a commercial ADS1282 ADC completes the setup. A personal computer controls the measurement steps, stores the measured data and runs offline all the calculations required to obtain the images.

### 6.4.1 Signal Acquisition and Calibration

To record the data for image generation, the target is placed on the support, the transmitter illuminates the scene frequency by frequency by transmitting a single tone at the time, and the receiver measures the backscatter from the target. The baseband quadrature output signals are sampled and digitized by the external ADC. The procedure is iterated to cover all the desired target positions.

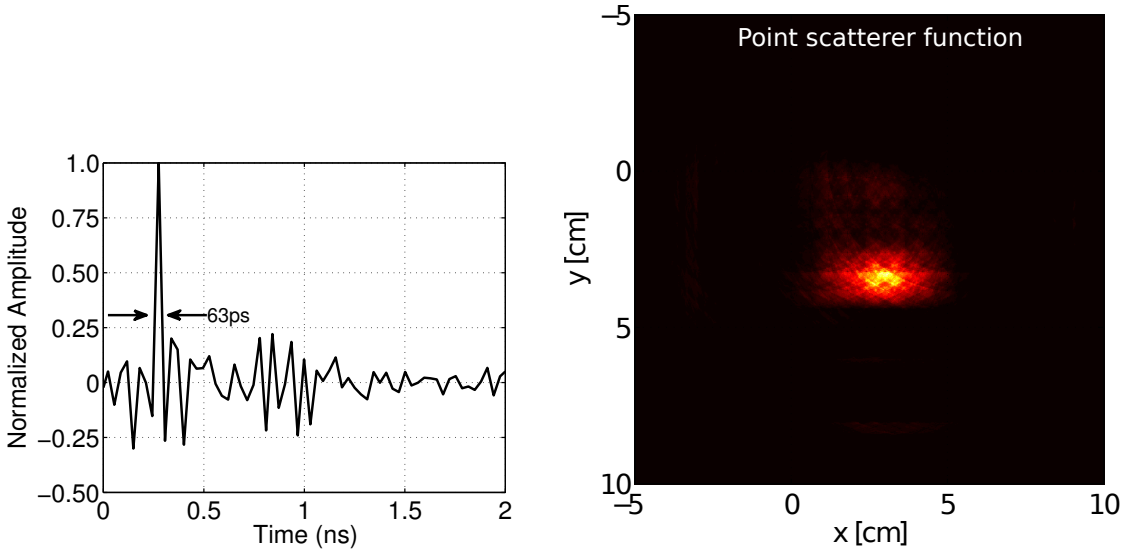


(a) (b)

Figure 6.11: Measured synthetic time-domain pulse scattered off a metallic plane (a); measured radar image of a 3.5mm-diameter metallic bead used as point scatterer (b).

In order to cope with the receiver and ADC offsets, which are a critical impairment in a direct conversion architecture, the measurement is made of two parts: First, the switch embedded in the transmitter poly-phase harmonic rejection filter is turned on. This allows to measure all the offsets due to components mismatch, local oscillator feedthrough, self mixing, and transmitter-to-receiver leakage through the substrate of the integrated circuit, as well as the ADC intrinsic offset. Second, the transmitter output buffer is turned on and the scene is effectively illuminated. The first measurement is subtracted from the second one to obtain a calibrated response.

A further calibration procedure is required to be able to discriminate the reflections due to the measurement setup and the surrounding environment. The procedure is similar to the "match/short" calibration usually performed on VNAs. A background acquisition (corresponding to the "match" measurement) is first carried out by performing a measurement with no target on the support. This data will be subtracted by the raw data obtained when the target is present. Then, a metallic plane is placed 4.6 cm away from the antenna structure. This corresponds to a "short" measurement, and allows to identify the reference plane of the radar system [28].

### 6.4.2 Measurement Results

As a first test of the correct operation of the system, the backscatter off a metallic plane displaced by 0.5 cm from the reference plane is measured. The time-domain synthetic pulse obtained after IFFT is shown in Fig. 6.11(a). The pulse is well defined and its duration is 63 ps. This corresponds to a slant-range resolution of 9 mm in the air and 3 mm in the body, where the phase velocity reduces by three times because of the different electrical properties of the body tissues [19].

A 3.5 mm-diameter metallic bead is used as a point scatterer to asses the ability of the radar to properly detect small scatterers. The measured radar point scatterer function is shown in Fig. 6.11(b). No artifacts are observed, yielding to a well defined image of the scatterer.

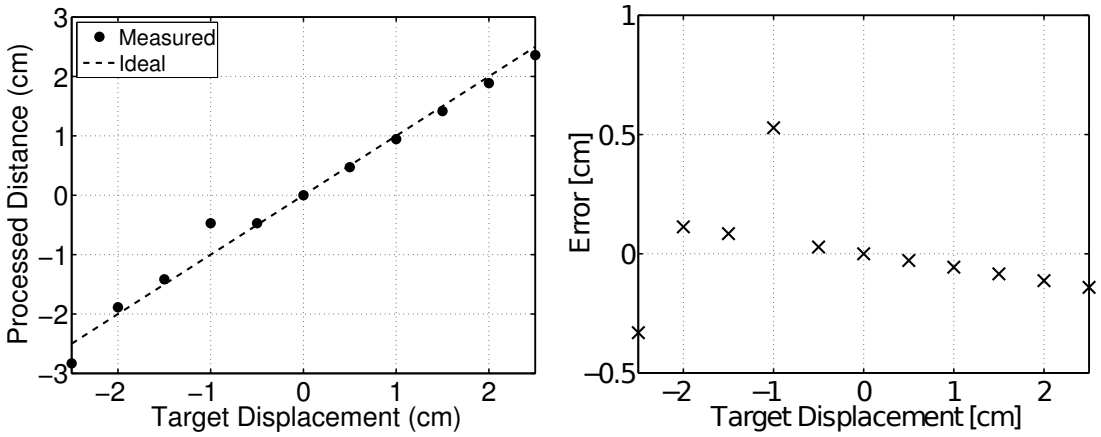


(a) (b)

Figure 6.12: Measured displacement of a metallic plane with respect to the reference plane (a); measurement accuracy (b).

The metallic plane is then placed at different distances from the antennas to characterize the ability of the system to properly detect the distance. The measured displacements from the reference plane are shown in Fig. 6.12(a) and compared to ideal positions. The measurement accuracy is always better than 0.5 cm, as highlighted in Fig. 6.12(b).

To assess the functionality of the proposed radar transceiver in seeking to identify the presence and location of relevant scatters inside the breast, the realized phantom is placed on the support and the set of wideband measurements is performed. The setup is shown in Fig. 6.13. The antenna is scanned over an equivalent array of 23 cm by 15 cm at 1 cm steps. Figure 6.14(a) shows the resulting image on the $x$-$y$ plane for $z = 7$ cm: Both tumors are correctly detected and located, and the scatterers are well confined and enhanced with respect to the surrounding clutter. The same imaging experiment is repeated using a commercial VNA, as illustrated in Fig. 6.14(b). The comparison between the obtained images shows that the proposed system is effectively capable of replacing the VNA in a setup for breast cancer imaging.

The measured radar image on the $z$-$x$ plane for $y = 1$ cm is shown in Fig. 6.15(a). The plane cuts through both targets, and in fact the two tumors are clearly visible in the cross-section. A small artifact is also visible. However, since it lays outside the volume of the phantom, it does not hinder the detection of the targets. The measured radar image on the $z$-$y$ plane for $x = 1.5$ cm is shown in Fig. 6.15(b). This plane cuts through the tumor target "B" (cf. Fig. 6.14(a)). The tumor is well defined, despite the presence of some clutter that forms a sort of trail.

## 6.5 Conclusions

The presented integrated radar transceiver and companion transmission/reception antenna structure are, to the best of the authors' knowledge, the first attempt of integrated custom hardware dedicated to microwave imaging systems for medical applications, in particular for the early diagnosis of breast cancer. The experimental results, performed on a realistic breast phantom, clearly show that the proposed system can replace commercial laboratory equipment with advantages in terms of performance, size, and cost of the imaging setup. We believe that this

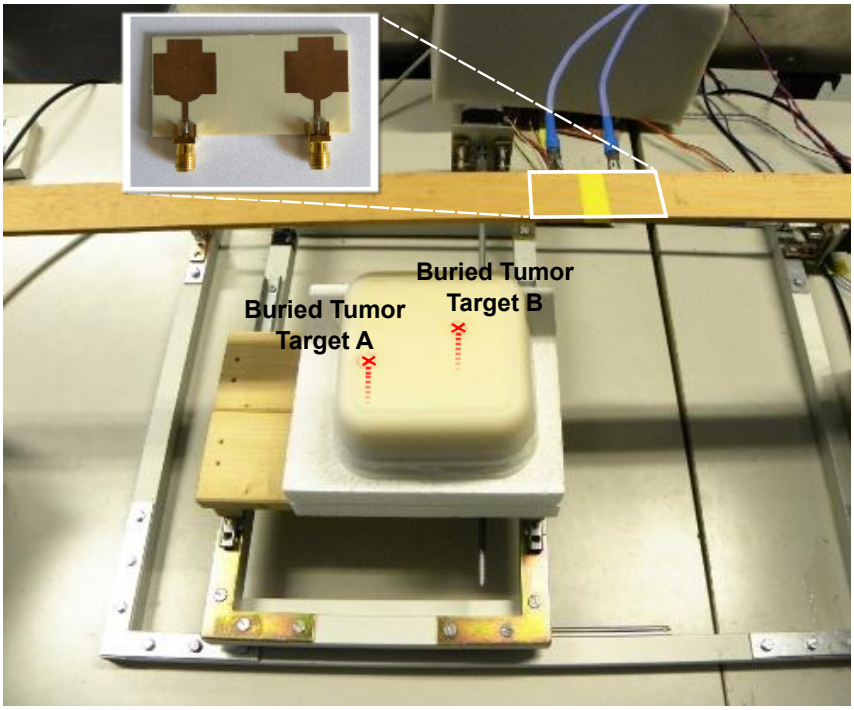


Figure 6.13: Photograph of the measurement setup.

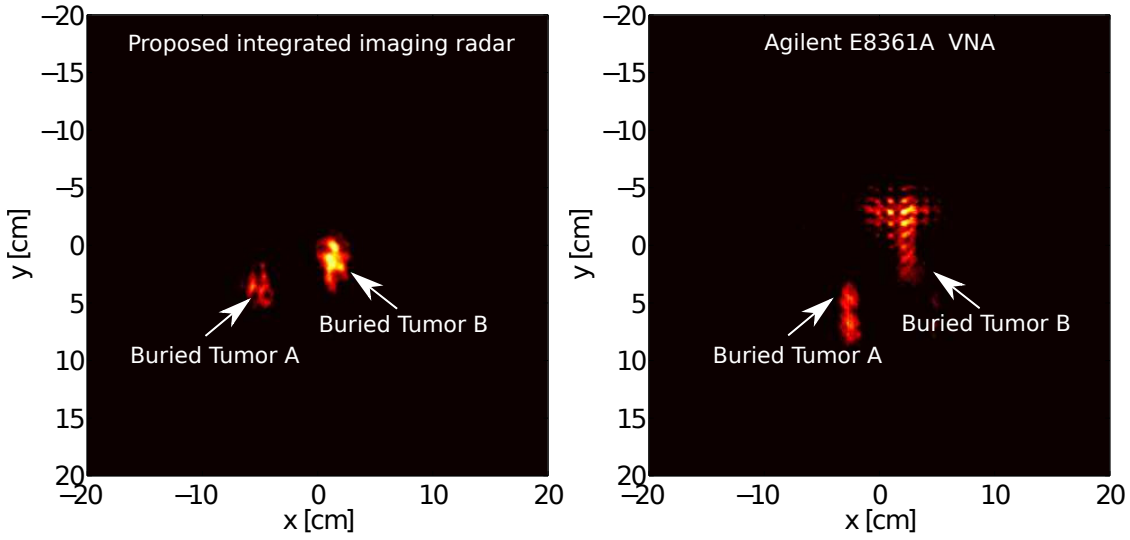


(a) (b)

Figure 6.14: Measured radar image of a breast phantom mimicking healthy tissue ($\epsilon_r \sim 9$) with two buried tumors ($\epsilon_r \sim 50$) on the $x$-$y$ plane for $z = 7$ cm. The crosses indicate the actual tumor target position. The image on the left is obtained using the proposed integrated radar. The same experiment is repeated using a commercial VNA in the setup (image on the right). The comparison between the two radar images clearly shows that the proposed integrated circuit is capable of replacing a VNA in a setup for medical imaging applications.

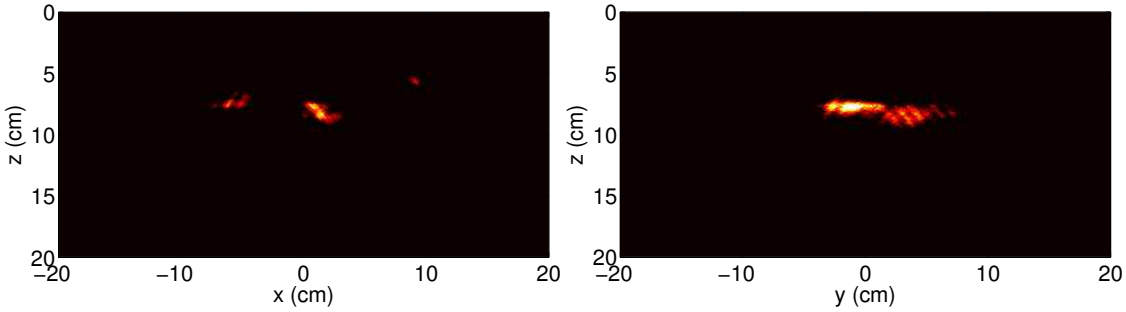


(a) (b)

Figure 6.15: (a) Measured radar image on the $z$-$x$ plane for $y = 1$ cm. (b) Measured radar image on the $z$-$y$ plane for $x = 1.5$ cm.

effort of custom hardware design can effectively contribute to the development of a technology, the microwave radar imaging, that has the potential to significantly improve the health of people.

# 7 Conclusions

In this thesis, I investigated the opportunities offered by microwaves and state-of-art silicon technologies to realize a low cost and compact breast cancer imaging and detection system based on stepped-frequency continuous (SFCW) wave radar.

A through behavioral analysis of two different transceiver architectures for UWB breast cancer imaging employing a SFCW radar system was presented. A mathematical model of the direct conversion and super heterodyne architectures together with a numerical breast phantom was developed. FDTD simulations data were used on the behavioral model to investigate the limits of both architectures from a circuit-level point of view. The result is that the simplicity of the direct conversion makes the receiver more robust towards the critical circuit impairments for this application, that is the random phase mismatches between the TX and RX local oscillators.

Insight is given into the challenging requirements for the targeted imaging transceiver. In fact, the transceiver needs to operate over a very large frequency range from 2 to 18 GHz to detect tumors with a resolution of 3 mm inside the body. An instantaneous dynamic range in excess of 100 dB is necessary over the whole 14 GHz bandwidth to properly process the signals backscattered from the breast. Moreover, since the imaging process is based on phase measurements, the I/Q phase inaccuracies must be kept below 1.5 ° over more than three octaves. Achieving such a tight specifications over a bandwidth that is more than twice the one of WiMedia and SDR systems is a great challenge.

The transceiver was realized in a 65 nm CMOS process. It occupies an area of 1.3 by 1 $mm^2$ and it consumes 204 mW from a 1.2 V power supply. The RX features 36 dB conversion gain, > 29 dBm compression point, 7 dB noise figure, and 30 Hz 1/f noise corner. The TX outputs 14 dBm with > 40 dBc harmonic rejection and < 109 dBc/Hz phase noise at 1 MHz offset. The radar achieves 3 mm resolution within the body, and 107 dB dynamic range, a performance enabling the use for breast cancer diagnostic imaging. The design of the imaging transceiver was complemented by a couple of wideband patch antennas with decoupling structure.

Several experiments were carried out to assess the imaging performances of the realized transceiver. Among them, the most significant shows that the proposed radar is able to correctly recognize two tumor scatters buried inside a physical breast phantom realized to conduct the experiment. Both tumors are correctly detected and located, and the scatterers are well confined and

enhanced with respect to the surrounding clutter.

To put this result in perspective, the high resolution obtainable with the proposed imaging transceiver may also be employed in other medical scenarios. Yearly-based nevus imaging is the most effective tool to prevent severe skin cancer (i.e. melanoma). A high resolution three dimensional image of the inner part would certainly improve the global diagnostic picture offered to the medical operator [21]. Also, increasing interest was shown by urologists toward the prostate imaging as an important tool for tumor localization, staging and detection of recurrences [91]. Generally talking, the proposed radar system can be employed whenever a difference in the tissue dielectric properties is present. Consequently, its effectiveness can be further improved by the continuous advances of the medical contrast agents [14], a research field that has seen a dramatic increase of interest in the recent years [92].

To conclude, the presented integrated radar transceiver and companion transmission/reception antenna structure are, to the best of my knowledge, the first attempt of integrated custom hardware dedicated to microwave imaging systems for medical applications, in particular for the early diagnosis of breast cancer. The experimental results, performed on a realistic breast phantom, clearly show that the proposed system can replace commercial laboratory equipment with advantages in terms of performance, size, and cost of the imaging setup. We believe that this effort of custom hardware design can effectively contribute to the development of a technology, the microwave radar imaging, that has the potential to significantly improve the health of people.

# A High-Order Output Matching Networks for Broadband Power Amplifiers

CMOS technology offers a powerful platform for realizing a various range of high data rate non-line-of-sight wireless applications. Thanks to the rapid device scaling in recent years, a full radio system can be embedded in a single chip with unparalleled integration level and extensive digital processing. However, power amplifier, which greatly affects the entire transmitter power efficiency and output signal quality, still remains one of the most challenging blocks for the full transceiver implementation. Due to the limited device breakdown voltage, a large impedance transformation radio to generate high output power is often needed. This often results in prohibitive passive loss and complicates the design process.

In this section, we analyze three possible broadband passive matching networks able to couple the signal generated by the power devices to the load. These networks fall inside the category of the so-called singly terminated filters (STF), where the filter is terminated with the characteristic impedance on one side only. A design method to convert the presented networks to a transformer-based differential-to-single-ended topology is also presented, along with its design constraints.

## A.1 Transfer Function Derivation

The three different coupling networks considered in this analysis are shown in Fig. A.1. The power amplifier that drives the network is modeled as an ideal current source. Its parasitic output capacitance is supposed to be included in the filters' capacitors $C_1$. The load resistance is $R_L$. Fig A.1(a) shows the $\Gamma$ filter, made of a parallel RLC network and a series RLC network. Fig A.1(b) and A.1(c) show the $\pi_C$ and $\pi_L$ filters, respectively. These two filters are made of two parallel RLC tanks coupled with a capacitor and an inductor, respectively. The target of this derivation is to get insight into the design of the networks. As such, two hypothesis are made to easy the mathematical derivation:

- All the tanks have the same intrinsic resonant frequency
- The quality factor Q of tanks is high enough

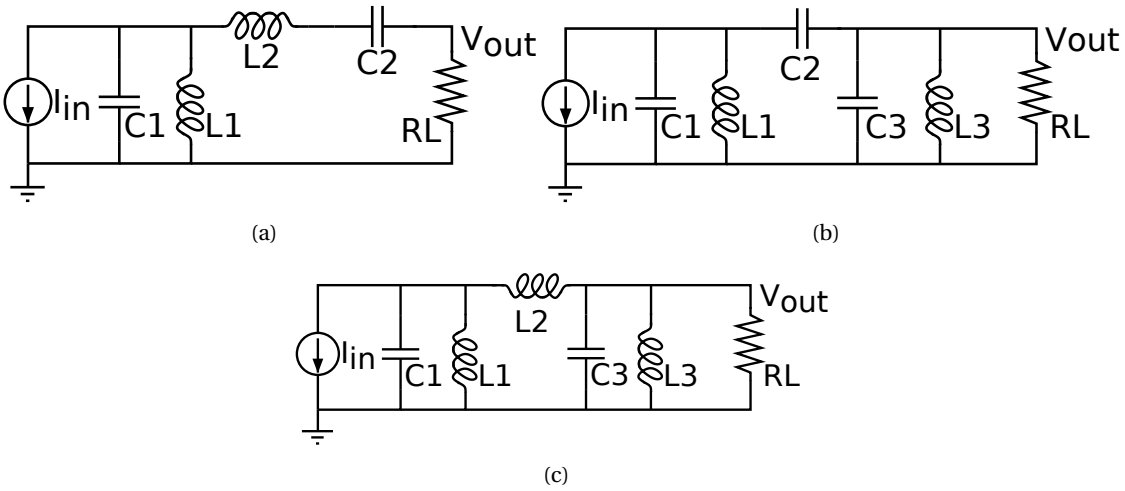


Figure A.1: The analyzed three different output filters: A.1(a) is the Γ filter, A.1(b) is the $\pi_C$ filter and A.1(c) is the $\pi_L$ filter.

### A.1.1 Γ Filter

The Γ filter is shown in Fig. A.1(a). The impedance of the two LC tanks is

$$\begin{aligned} Z_1 &= \frac{sL_1}{1+s^2L_1C_1} \\ Z_2 &= \frac{1+sC_2R_L+s^2L_2C_2}{sC_2}. \end{aligned} \tag{A.1}$$

The transfer function from the input current $I_{in}$ to the output voltage $V_{out}$ can be written as

$$\frac{V_{out}}{I_{in}} = T(s) = \frac{N(s)}{D(s)} = R_L\frac{Z_1}{Z_1+Z_2}, \tag{A.2}$$

where

$$N(s) = s^2\frac{mR_L}{\omega_0^2}, \tag{A.3}$$

and

$$D(s) = 1+\frac{s}{\omega_0 Q_L}+\frac{s^2}{\omega_0^2}(2+m)+\frac{s^3}{\omega_0^3 Q_L}+\frac{s^4}{\omega_0^4}, \tag{A.4}$$

where $\omega_0^2 = \frac{1}{L_1C_1} = \frac{1}{L_2C_2}$, $m = L_1/L_2 = C_2/C_1$ and $Q_L = \frac{1}{\omega_0 C_2 R_L}$. When $Q_L$ is large enough, the denominator of (A.2) becomes

$$D(s) \simeq 1+\frac{s^2}{\omega_0^2}(2+m)+\frac{s^4}{\omega_0^4}, \tag{A.5}$$

and therefore

$$\begin{aligned} s_{1\ldots4} &= \pm j\omega_0\sqrt{\left|-\frac{m+2}{2}\pm\frac{\sqrt{m^2+4m}}{2}\right|} \\ &= \pm j\omega_0\overline{\beta}_{1,2}. \end{aligned} \tag{A.6}$$

At this point, since (A.4) is forth-order, it can be certainly written as

$$\begin{aligned} D(s) =& \left(1+\frac{s}{\beta_1 Q_1}+\frac{s^2}{\beta_1^2}\right)\left(1+\frac{s}{\beta_2 Q_2}+\frac{s^2}{\beta_2^2}\right) \\ =& 1+s\left(\frac{1}{\beta_1 Q_1}+\frac{1}{\beta_2 Q_2}\right)+s^3\left(\frac{1}{\beta_1\beta_2^2 Q_1}+\frac{1}{\beta_1^2\beta_2 Q_2}\right)+\dots \end{aligned} \tag{A.7}$$

By equating the first and third order terms of (A.4) and (A.7), we obtain the following system:

$$\begin{cases} \frac{1}{\overline{\beta}_1 Q_1}+\frac{1}{\overline{\beta}_2 Q_2}=\frac{1}{Q_L} \\ \frac{1}{\overline{\beta}_1\overline{\beta}_2^2 Q_1}+\frac{1}{\overline{\beta}_1^2\overline{\beta}_2 Q_2}=\frac{1}{Q_L} \end{cases} \tag{A.8}$$

and the values of $Q_1$ and $Q_2$ as:

$$\begin{aligned} Q_1 =& Q_L\frac{\overline{\beta}_1^2-\overline{\beta}_2^2}{\overline{\beta}_1\overline{\beta}_2^2(\overline{\beta}_1^2-1)} \\ Q_2 =& Q_L\frac{\overline{\beta}_1^2-\overline{\beta}_2^2}{\overline{\beta}_1^2\overline{\beta}_2(\overline{\beta}_2^2-1)}. \end{aligned} \tag{A.9}$$

### A.1.2 $\pi_C$ Filter

The $\pi_C$ filter is shown in Fig. A.1(b). The impedance of the two LC tanks is

$$\begin{aligned} Z_1 =& \frac{sL_1}{1+s^2L_1C_1} \\ Z_3 =& \frac{sL_3}{1+\frac{s}{\omega_0 Q+\frac{s^2}{\omega_0^2}}}, \end{aligned} \tag{A.10}$$

where $Q_L = R_L C_3$ and $\omega_0 = \frac{1}{L_3C_3} = \frac{1}{L_1C_1}$. At this point, the transfer function from the input current $I_{in}$ to the output voltage $V_{out}$ is

$$\frac{V_{out}}{I_{in}} = T(s) = \frac{N(s)}{D(s)} = \frac{Z_1}{Z_1+\frac{1}{sC_2}+Z_3}Z_3, \tag{A.11}$$

where

$$N(s) = s^3\frac{mR_L}{\omega_0^3 Q_L}, \tag{A.12}$$

and

$$\begin{aligned} D(s) = & 1 + \\ & s\left(\frac{1}{\omega_0 Q_L}\right) + \\ & s^2\left(\frac{m+k}{\omega_0^2} + \frac{2}{\omega_0^2}\right) + \\ & s^3\left(\frac{m+1}{\omega_0^3 Q_L}\right) + \\ & s^4\left(\frac{1}{\omega_0^4} + \frac{m+k}{\omega_0^4}\right), \end{aligned} \tag{A.13}$$

where $m = C_2/C_1$ and $k = C_2/C_3$. When $Q_L$ is large enough the denominator of (**??**) becomes

$$D(s) \simeq 1 + s^2\left(\frac{m+k}{\omega_0^2} + \frac{2}{\omega_0^2}\right) + s^4\left(\frac{1}{\omega_0^4} + \frac{m+k}{\omega_0^4}\right) \tag{A.14}$$

and therefore

$$\begin{aligned} s_{1\ldots4} &= \pm j\omega_0\sqrt{|x_{1,2}|} \\ &= \pm j\omega_0\overline{\beta}_{1,2}, \end{aligned} \tag{A.15}$$

where

$$\begin{aligned} x_1 &= -1 \\ x_2 &= -\frac{1}{(m+k+1)}. \end{aligned} \tag{A.16}$$

At this point, (A.13) can be written as

$$\begin{aligned} D(s) &= \left(1 + \frac{s}{\beta_1 Q_1} + \frac{s^2}{\beta_1^2}\right)\left(1 + \frac{s}{\beta_2 Q_2} + \frac{s^2}{\beta_2^2}\right) \\ &= s\left(\frac{1}{\beta_1 Q_1} + \frac{1}{\beta_2 Q_2}\right) + s^3\left(\frac{1}{\beta_1\beta_2^2 Q_1} + \frac{1}{\beta_1^2\beta_2 Q_2}\right) + \ldots \end{aligned} \tag{A.17}$$

By equating the first and third order terms of (A.13) and (A.17), we obtain the following system:

$$\begin{cases} \frac{1}{\overline{\beta}_1 Q_1} + \frac{1}{\overline{\beta}_2 Q_2} = \frac{1}{Q_L} \\ \frac{1}{\overline{\beta}_1\overline{\beta}_2^2 Q_1} + \frac{1}{\overline{\beta}_1^2\overline{\beta}_2 Q_2} = \frac{m+1}{Q_L} \end{cases} \tag{A.18}$$

and the values of $Q_1$ and $Q_2$ as:

$$\begin{aligned} Q_1 &= Q_L \frac{\overline{\beta}_1^2 - \overline{\beta}_2^2}{\overline{\beta}_1\overline{\beta}_2^2(\overline{\beta}_1^2 m + \overline{\beta}_1^2 - 1)} \\ Q_2 &= Q_L \frac{\overline{\beta}_1^2 - \overline{\beta}_2^2}{\overline{\beta}_1^2\overline{\beta}_2(\overline{\beta}_2^2 m + \overline{\beta}_2^2 - 1)}. \end{aligned} \tag{A.19}$$

### A.1.3 $\pi_L$ Filter

The $\pi_L$ filter is shown in Fig. A.1(c). The impedance of the two LC tanks is

$$\begin{aligned} Z_1 &= \frac{sL_1}{1+s^2L_1C_1} \\ Z_3 &= \frac{sL_3}{1+\frac{s}{\omega_0 Q+\frac{s^2}{\omega_0^2}}}, \end{aligned} \tag{A.20}$$

where $Q_L = R_L C_3$ and $\omega_0 = \frac{1}{L_3C_3} = \frac{1}{L_1C_1}$. At this point, the transfer function from the input current $I_{in}$ to the output voltage $V_{out}$ is

$$\frac{V_{out}}{I_{in}} = T(s) = \frac{N(s)}{D(s)} = \frac{Z_1}{Z_1+sL_2+Z_3}Z_3, \tag{A.21}$$

where

$$N(s) = s\frac{mR_L}{\omega_0 Q_L}, \tag{A.22}$$

and

$$\begin{aligned} D(s) =& 1+m+k+ \\ & s\left(\frac{1+m}{\omega_0 Q_L}\right)+ \\ & s^2\left(\frac{2+m+k}{\omega_0^2}\right)+ \\ & s^3\left(\frac{1}{\omega_0^3 Q_L}\right)+ \\ & s^4\left(\frac{1}{\omega_0^4}\right), \end{aligned} \tag{A.23}$$

where $m = L_1/L_2$ and $k = L_3/L_2$. When $Q_L$ is large enough the denominator of (A.23) becomes

$$D(s) \simeq 1+m+k+\frac{s^2}{\omega_0^2}(2+m+k)+\frac{s^4}{\omega_0^4}, \tag{A.24}$$

and therefore

$$\begin{aligned} s_{1\ldots4} &= \pm j\omega_0\sqrt{|x_{1,2}|} \\ &= \pm j\omega_0\overline{\beta}_{1,2}, \end{aligned} \tag{A.25}$$

where

$$\begin{aligned} x_1 &= -1 \\ x_2 &= -(m+k+1). \end{aligned} \tag{A.26}$$

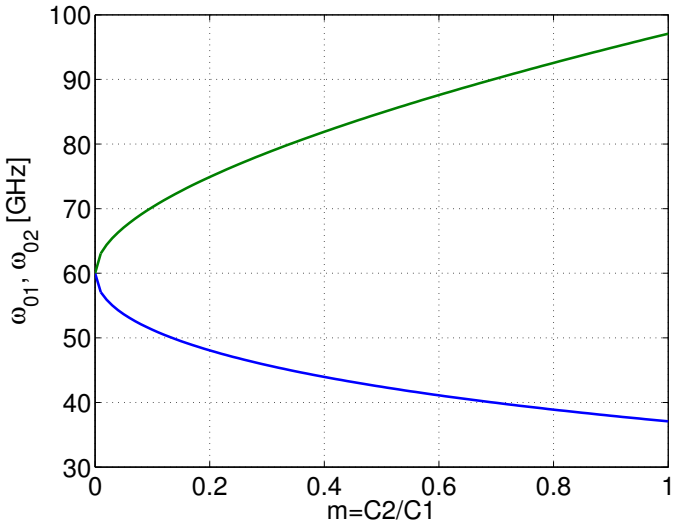


Figure A.2: Pole splitting behavior of Γ filter.

At this point, (A.23) can be written as

$$\begin{aligned} D(s) &= \left(1+\frac{s}{\beta_1 Q_1}+\frac{s^2}{\beta_1^2}\right)\left(1+\frac{s}{\beta_2 Q_2}+\frac{s^2}{\beta_2^2}\right) \\ &= s\left(\frac{1}{\beta_1 Q_1}+\frac{1}{\beta_2 Q_2}\right)+s^3\left(\frac{1}{\beta_1\beta_2^2 Q_1}+\frac{1}{\beta_1^2\beta_2 Q_2}\right)+\dots \end{aligned} \tag{A.27}$$

By equating the first and third order terms of (A.23) and (A.27), we obtain the following system:

$$\begin{cases} \frac{1}{\overline{\beta}_1 Q_1}+\frac{1}{\overline{\beta}_2 Q_2}=\frac{m+1}{Q_L} \\ \frac{1}{\overline{\beta}_1\overline{\beta}_2^2 Q_1}+\frac{1}{\overline{\beta}_1^2\overline{\beta}_2 Q_2}=\frac{1}{Q_L} \end{cases} \tag{A.28}$$

and the values of $Q_1$ and $Q_2$ as:

$$\begin{aligned} Q_1 &= -Q_L\frac{\overline{\beta}_1^2-\overline{\beta}_2^2}{\overline{\beta}_1\overline{\beta}_2^2(m+1-\overline{\beta}_1^2)} \\ Q_2 &= Q_L\frac{\overline{\beta}_1^2-\overline{\beta}_2^2}{\overline{\beta}_1^2\overline{\beta}_2(m+1-\overline{\beta}_2^2)}. \end{aligned} \tag{A.29}$$

## A.2 Design Guidelines

The equations derived in the Section A.1 can be used to get insight on the design of the filters. For a desired bandwidth $B$ and given load resistance $R_L$, the three presented filters behave differently.

In the Γ filter, once the central frequency $\omega_0$ is set, the filter bandwidth can be adjusted by increasing the ratio $m = C_2/C_2$. This behavior is described by Eq. (A.6). An example is shown in Fig. A.2, where $\omega_0$=60 GHz and a bandwidth of 32 GHz (20 GHz plus some margin) can be obtained by setting $m$=0.4.

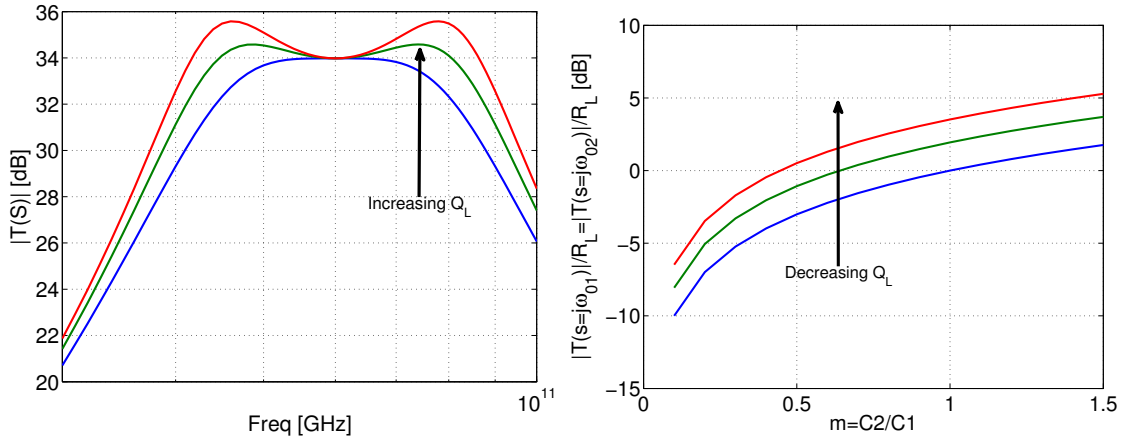


(a) (b)

Figure A.3: Behavior of the Γ filter as a function of the quality factor $Q_L$. In Fig. A.3(a) the behavior over the whole bandwidth. In Fig. A.3(b), the behavior of the edges of the bandwidth with respect to the center.

The increase or decrease of loaded quality factor $Q_L$ is responsible for the behavior of the filter at the edge of the bandwidth, as shown in Fig. A.3(a). Fig. A.3(b) shows the normalized filter response at the edges of the bandwidth: once the ratio $m$ is set, Q can be chosen such that the filter response is flat over the desired bandwidth. As an example, if $m$ is 0.4, a $Q_L$ of 1.25 is chosen for flat response. At this point, $R_L$, $\omega_0$, $m$ and $Q_L$ are fixed and all the components of the filter can be calculated as:

$$\begin{aligned} C_2 &= 1/(\omega_0 Q_L R_L) \\ L_2 &= 1/(\omega_0^2 C_2) \\ C_1 &= C_2/m \\ L_1 &= 1/(\omega_0^2 C_1). \end{aligned} \tag{A.30}$$

The $\pi_L$ and $\pi_C$ filters have a different behavior. In fact, in the Γ filter, once the central frequency $\omega_0$ is chosen, the poles are symmetrically splitting apart by increasing the capacitor ratio $m$. In the case of $\pi_C$ and $\pi_L$ filters, as anticipated by Eq. (A.15),(A.16) and Eq. (A.25),(A.26), $\omega_0$ is responsible for the position of the pole at the upper and lower edge of the bandwidth, respectively. The splitting action on the other pole is driven by the variable $d$, defined as $d = m + k$. As such, the complex poles for the $\pi_C$ filter can be written as

$$s_{1,2} = \pm j\omega_0, \quad s_{3,4} = \pm j\omega_0\sqrt{1/(d+1)}, \tag{A.31}$$

while the complex poles for the $\pi_L$ filter as

$$s_{1,2} = \pm j\omega_0\sqrt{d+1}, \quad s_{3,4} = \pm j\omega_0. \tag{A.32}$$

The situation is depicted in Fig. A.4, where the $\omega_0$ is set to 76 GHz and 44 GHz for the $\pi_C$ and $\pi_L$, respectively. In both the filters a bandwidth of 32 GHz can be obtained by setting $d$=2.25.

Similarly to the Γ filter, the loaded quality factor $Q_L$ is responsible for the behavior of the filter at one edge of the band and at center band. The situation is depicted in Fig. A.5. While the behavior

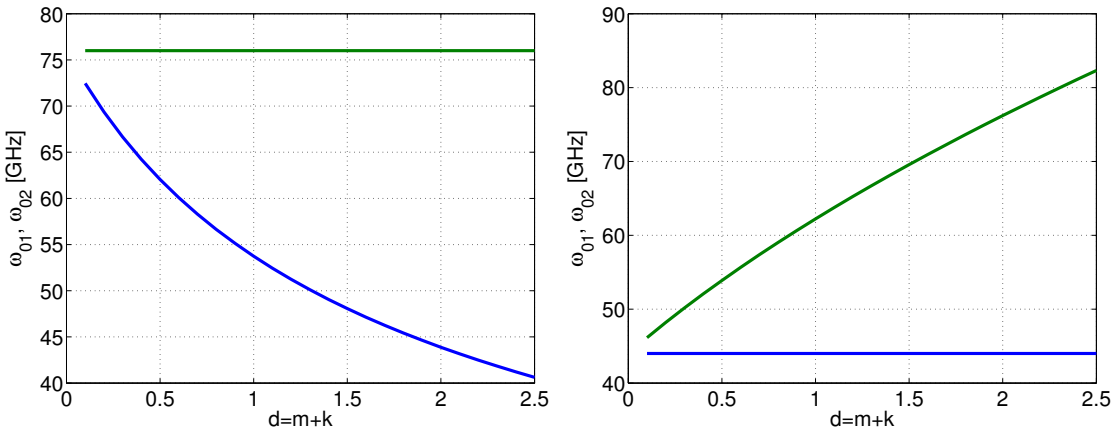


(a) (b)

Figure A.4: Pole splitting behavior of the $\pi_C$ filter (Fig. A.4(a)) and $\pi_L$ filter (Fig. A.5(b)).

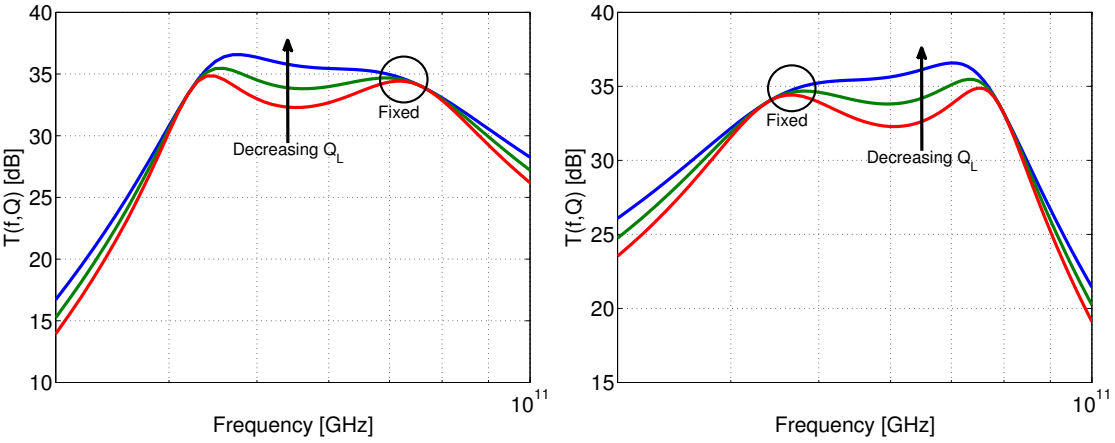


(a) (b)

Figure A.5: Behavior of the $\pi_C$ filter (Fig. A.5(a)) and $\pi_L$ filter (Fig. A.5(b)) for decreasing values of $Q_L$.

at $s_{1,2}$ and $s_{3,4}$ for the $\pi_C$ and $\pi_L$ filter, respectively, does not change with $Q_L$, by decreasing $Q_L$ the filter response at the center of the band can be properly tuned.

In fact, once $d$ has been picked for the desired bandwidth, $m$ and $Q_L$ can be chosen to obtain a flat filter response. An example is depicted in Fig. A.6, where the normalized filter response at the fixed edge of the bandwidth is plotted together with the one at center band as a function of $m$. A loaded quality factor $Q_L$=1.25 with $m$=1.15 yield 0 dB insertion loss; since $d$=2.25, $k = d - m$ is 1.1.

At this point, $R_L$, $\omega_0$, $m$, $d$, $k$ and $Q_L$ are fixed and all the components of the $\pi_C$ and $\pi_L$ filters

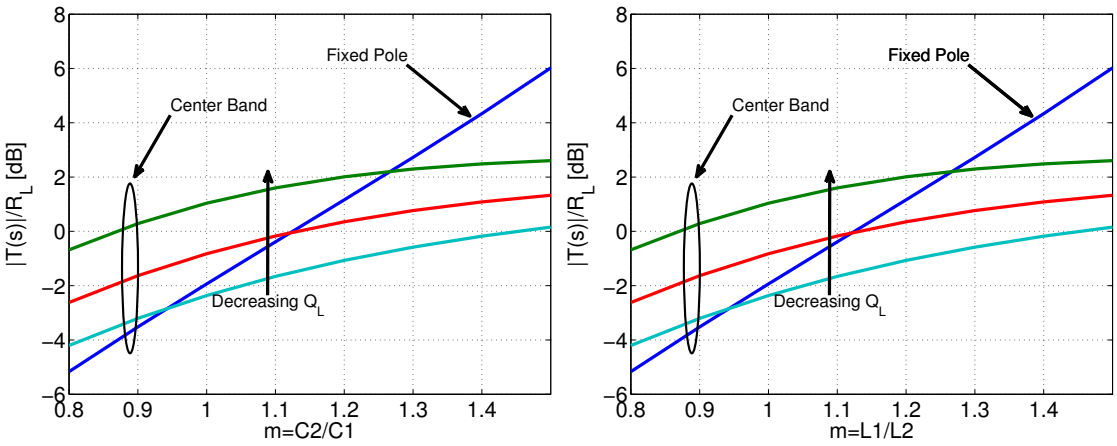


(a) (b)

Figure A.6: Behavior of the $\pi_C$ filter (Fig. A.6(a)) and $\pi_L$ filter (Fig. A.6(b)) for decreasing values of $Q_L$.

can be calculated as:

$$\begin{aligned} C_2 &= kQ_L/(R_L\omega_0), \\ C_1 &= C_2/m, \\ L_1 &= 1/(\omega_0^2 C_1), \\ C_3 &= C_2/k, \\ L_3 &= 1/(\omega_0^2 C_3), \end{aligned} \tag{A.33}$$

for the $\pi_C$ filter and

$$\begin{aligned} L_3 &= R_L/(\omega_0 Q_L), \\ L_2 &= L_3/k, \\ L_1 &= mL_2, \\ C_1 &= 1/(\omega_0^2 L_1), \\ C_3 &= 1/(\omega 0^2 L_3), \end{aligned} \tag{A.34}$$

for the $\pi_L$ filter.

For the sake of completeness, the behavior of the three considered filters is compared in Fig. A.7. The filters are designed to cover a bandwidth of 32 GHz centered around 60 GHz. Note that the $\pi_L$, $\Gamma$ and $\pi_C$ filters have 1, 2 and 3 zeros in the origin, respectively and the same number of poles. This translates to a different out-of-band behavior. Consequently, the $\pi_L$ filter shows a better suppression of the second and third harmonic of the center frequency $f_0$=60 GHz.

Table A.1 reports the value of the lumped elements needed to realize a filter with a bandwidth of 32 GHz centered around 60 GHz and flat response. All filters show synthesizable values.

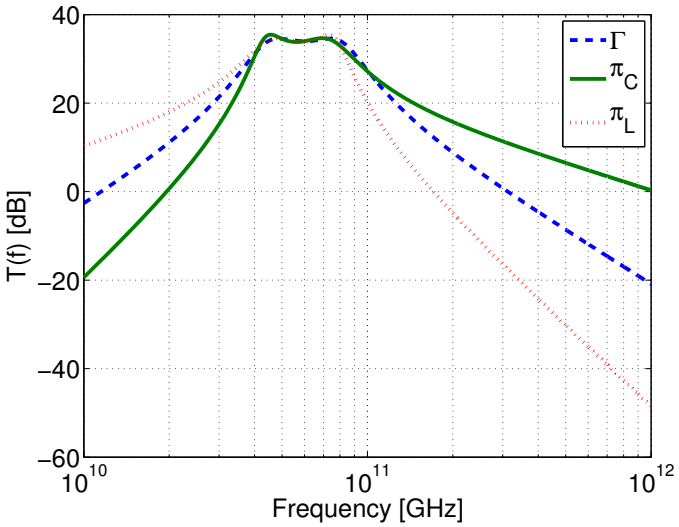


Figure A.7: Γ, $\pi_C$ and $\pi_L$ filter response comparison.

| | $C_1$ [fF] | $L_1$ [pH] | $C_2$ [fF] | $L_2$ [pH] | $C_3$ [fF] | $L_3$ [pH] | Att2h [dB] | Att3h [dB] |
|---|---|---|---|---|---|---|---|---|
| Γ | 84 | 82 | 42 | 165 | - | - | 13 | 23 |
| $\pi_C$ | 54 | 80 | 60 | - | 53 | 83 | 11 | 17 |
| $\pi_L$ | 94 | 138 | - | 125 | 90 | 144 | 22 | 35 |

Table A.1: Lumped elements values for Γ, $\pi_C$ and $\pi_L$ filters covering a bandwidth of 32 GHz centered around 60 GHz.

# B OOK Receiver System Level Considerations

In this section, the link budget of a typical receiver for On-Off-Keying modulation is presented. In the general case, such a receiver consists on a low noise amplifier (LNA), that amplifies the signal while introducing as less noise as possible, a squarer element, to extract the energy of the signal and some form of post-amplification or equalization to drive the decision element. The situation is summarized in the block diagram of Fig. B.1, where $s_{in}$ is the input signal, $n_s$ the noise of the antenna, $G_{amp}$ the gain of the LNA, $n_{LNA}$ the noise introduced by the LNA, $a_2$ the gain of the squarer element and $n_{int}$ the noise of all the following circuits. The presence of a squarer element makes the system non-linear and the computation of the receiver noise figure not straightforward. Calculations are based on the previously published results presented in [93].

The input signal-to-noise ratio (SNR) $\Lambda_{in} = E[s_{in}^2]/E[n_{in}^2]$, where $E[\cdot]$ is the expected value, is

$$\Lambda_{in} = \frac{E[s_{in}^2]}{E[n_{in}^2]} = \frac{E[s_{in}^2]}{E[n_s^2]} = \frac{E_b B_r}{N_o B} \tag{B.1}$$

where $B_r$ is the bitrate, $N_o = KT = -174 dBm/Hz$, $B$ the RF bandwidth of the system. The SNR at the output can be calculated as

$$\Lambda_{out} = \frac{E[s_{out}^2]}{E[n_{out}^2]} \tag{B.2}$$

where

$$E[s_{out}^2] = E[G(s_{in}^2)^2] = G_{amp}^4 a_2^2 E_b^2 B_r^2 \tag{B.3}$$

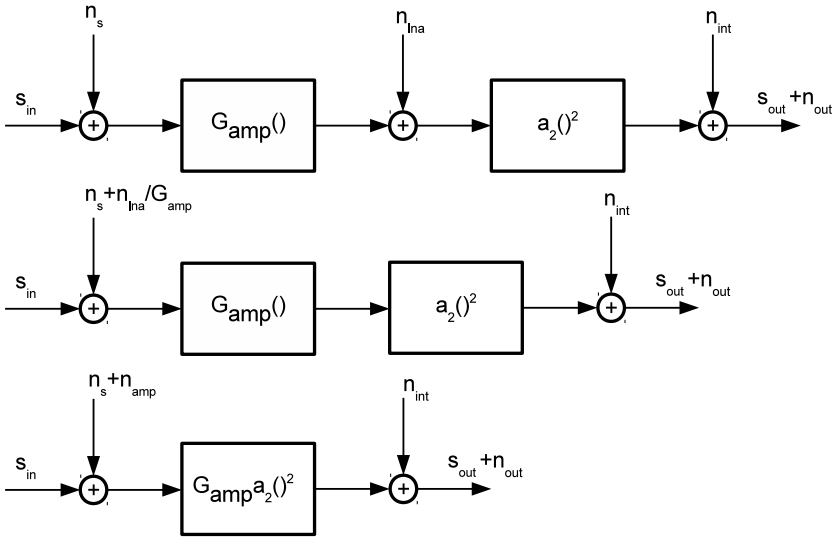


Figure B.1: On-Off-Keying receiver block diagram.

and

$$\begin{aligned} E[n_{out}^2] =& E[(n_{int} + G_{amp}^2 a_2 (s_{in} + n_s n_{amp})^2)^2] \\ & E[(n_{int} + G_{amp}^2 a_2 s_{in}^2 + G_{amp}^2 a_2 (n_s + n_{amp})^2 + 2G_{amp}^2 a_2 s_{in}(n_s n_{amp}))^2] \\ & E[(n_{int} + G_{amp}^2 a_2 (n_s + n_{amp})^2 + 2G_{amp}^2 a_2 s_{in}(n_s + n_{amp}))^2] \end{aligned} \tag{B.4}$$

where the term $Gs_{in}^2$ drops since we are evaluating the output noise power. Since $n_{int}$ is uncorrelated with $n_s + n_{amp}$ we can evaluate its expectation separately as

$$E[n_{int}^2] = \sigma_{n_{int}}^2. \tag{B.5}$$

As such, we are left with the following two terms to evaluate:

$$\begin{aligned} & E[(G_{amp}^2 a_2 (n_s + n_{amp})^2 + 2G_{amp}^2 a_2 s_{in}(n_s + n_{amp}))^2] = \\ & E[G_{amp}^4 a_2^2 (n_s + n_{amp})^4 + 4G_{amp}^4 a_2^2 s_{in}^2 (n_s + n_{amp})^2 + 4G_{amp}^4 a_2^2 s_{in}(n_s + n_{amp})^3]. \end{aligned} \tag{B.6}$$

By evaluating the expectation of the three terms we find:

$$\begin{aligned}
E[G^2(n_s+n_{amp})^4] &= E[G_{amp}^4 a_2^2 (n_s^2+n_{amp}^2+2n_s n_{amp})^2] \\
&= G_{amp}^4 a_2^2 E[n_s^4+n_{amp}^4+4n_s^2 n_{amp}^2+2n_s^2 n_{amp}^2+4n_s^3 n_{amp}+4n_s n_{amp}^3] \\
&= G_{amp}^4 a_2^2 (3\sigma_{n_s}^4+3\sigma_{n_{amp}}^4+6\sigma_{n_s}^2\sigma_{n_{amp}}^2+0+0) \\
&= 3G_{amp}^4 a_2^2 \sigma_{n_s}^4 \left(1+\frac{\sigma_{n_{amp}}^4}{\sigma_{n_s}^4}+2\frac{\sigma_{n_{amp}}^2}{\sigma_{n_s}^2}\right) \\
&= 3G_{amp}^4 a_2^2 \sigma_{n_s}^4 \left(1+\frac{\sigma_{n_{amp}}^2}{\sigma_{n_s}^2}\right)^2 \\
&= 3G_{amp}^4 a_2^2 \sigma_{n_s}^4 \left(1+\frac{\sigma_{n_{LNA}}^2}{G_{LNA}^2\sigma_{n_s}^2}\right)^2 \\
&= 3G_{amp}^4 a_2^2 \sigma_{n_s}^4 F_{amp}^2 \\
&= 3G_{amp}^4 a_2^2 N_o^2 B^2 F_{amp}^2,
\end{aligned} \tag{B.7}$$

$$\begin{aligned}
E[4G_{amp}^4 a_2^2 s_{in}^2 (n_s+n_{amp})^2] &= E[4G_{amp}^4 a_2^2 s_{in}^2 (n_s^2+n_{amp}^2)] + E[4G_{amp}^4 a_2^2 s_{in}^2 (2n_s n_{amp})] \\
&= 4G_{amp}^4 a_2^2 E_b B_r \sigma_{n_s}^2 (1+\frac{\sigma_{n_{amp}^2}}{\sigma_{n_s}^2}) + 0 \\
&= 4G_{amp}^4 a_2^2 E_b B_r N_o B F_{amp},
\end{aligned} \tag{B.8}$$

and

$$E[4G_{amp}^4 a_2^2 s_{in}(n_s+n_{amp})^3] = 0 \tag{B.9}$$

where the last term is zero since $n_s$ and $n_{amp}$ are normally distributed variables, their sum is a normally distributed variable and the odd-order moments of a normally distributed random variable are zero. Note also that the 4th-order central moment of a normally distributed random variable is $3\sigma^4$. We can hence write:

$$\Lambda_{out} = \frac{G_{amp}^4 a_2^2 E_b^2 B_r^2}{\sigma_{n_{int}}^2 + 4G_{amp}^4 a_2^2 E_b B_r N_o B F_{amp} + 3G_{amp}^4 a_2^2 N_o^2 B^2 F_{amp}^2}. \tag{B.10}$$

Solving for $P_b = E_b B_r$ we obtain:

$$\begin{aligned} P_b &= \frac{4G_{amp}^4 a_2^2 N_o B F_{amp} \Lambda_{out}}{2G_{amp}^4 a_2^2} \pm \\ &\pm \sqrt{\frac{16G_{amp}^8 a_2^4 N_o^2 B^2 F_{amp}^2 \Lambda_{out}^2 + 4G_{amp}^8 a_2^4 \sigma_{n_{int}}^2 \Lambda_{out} + 12G_{amp}^8 a_2^4 N_o^2 B^2 F_{amp}^2 \Lambda_{out}}{4G_{amp}^8 a_2^4}} \\ &= 2N_o B F_{amp} \Lambda_{out} \left(1 + \sqrt{1 + \frac{\sigma_{n_{int}}^2}{4G_{amp}^4 a_2^2 N_o^2 B^2 F_{amp}^2 \Lambda_{out}} + \frac{3}{4\Lambda_{out}}}\right). \end{aligned} \tag{B.11}$$

The receiver noise figure is eventually calculated as:

$$\mathrm{NF}_{RX} = \frac{\Lambda_{in}}{\Lambda_{out}} = 4F_{amp}\left(1 + \frac{\sigma_{n_{int}}^2}{4G_{amp}^4 a_2^2 E_b B_r N_o B F_{amp}} + \frac{3N_o B F_{amp}}{4E_b B_r}\right) \tag{B.12}$$

where $P_b = E_b B_r$ is given by (B.11).

Two important insights need to be highlighted: First, note that even if all the receiver blocks are completely noiseless, the nonlinear action of the squarer energy detector sets the receiver noise figure to 6 dB. Second, unlikely in a linear receiver case, the noise figure of the receiver does not depend only on the gain and noise figure of the single blocks, but also on the desired SNR at the output $\Lambda_{out}$, i.e. the BER of the receiver. This is due to the nonlinear action of the energy detector that multiplies the signal power by the power of the noise, as shown in Eq. (B.6).

As an example, Fig. B.2 shows the performance of a receiver where the LNA noise figure is set to 10 dB, the desired SNR at the output is 17 dB (desired BER is $10^{-12}$) with 6 dB link margin and the variance of the input referred noise of the equalizer is $4\mu V^2$. Note that if the equalizer did not introduce noise, the SNR at the input would be 37 dB.

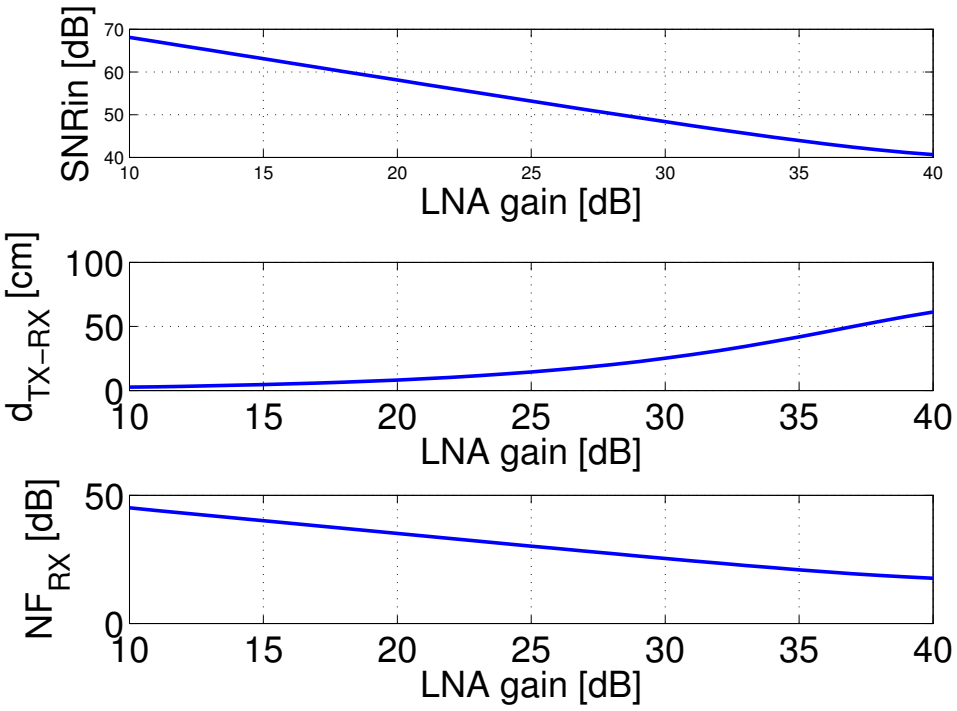


Figure B.2: Performance of the receiver with $NF_{LNA}$=10 dB, desired SNR at the decision element 22 dB, input referred noise of the equalizer $4\mu V^2$ as a function of the LNA gain.

# List of Publications

## Conference

1. Bassi, M.; Bevilacqua, A.; Gerosa, A.; Neviani, A.; , "Integrated transceivers for UWB breast cancer imaging: Architecture and circuit constraints," Circuits and Systems (ISCAS), 2011 IEEE International Symposium on , vol., no., pp.2087-2090, 15-18 May 2011, doi: 10.1109/ISCAS.2011.5938009

2. Bassi, M.; Caruso, M.; Bevilacqua, A.; Neviani, A.; , "A 1.75-15 GHz Stepped Frequency Receiver for Breast Cancer Imaging in 65 nm CMOS,", European Solid-State Circuits Conference (ESSCIRC), 2012 Proceedings of the

3. Bassi, M.; Caruso, M.; Bevilacqua, A.; Neviani, A.; , "A 2-16GHz 204mW 3mm-resolution stepped frequency radar for breast cancer diagnostic imaging in 65nm CMOS,", International Solid-State Circuits Conference (ISSCC), Accepted for publication

## Journal

1. Bassi, M.; Bevilacqua, A.; Gerosa, A.; Neviani, A.; , "Integrated SFCW Transceivers for UWB Breast Cancer Imaging: Architectures and Circuit Constraints," Circuits and Systems I: Regular Papers, IEEE Transactions on , vol.59, no.6, pp.1228-1241, June 2012, doi: 10.1109/TCSI.2011.2173400

2. Bassi, M.; Santinello, I., Bevilacqua, A., Bassi, PF.; , "Nanotecnologie, una grande rivoluzione che parte dal piccolo," Urologia, Accepted for publication

3. Bassi, M.; Caruso, M.; Bevilacqua, A.; Neviani, A.; , "An Integrated Microwave Imaging Radar with Planar Antennas for Breast Cancer Detection,", Microwave Theory and Techniques, IEEE Transactions on - Accepted for publication

# Bibliography


[1] "Surveillance, epidemiology, and end results (SEER) program research data (1973-2008), national cancer institute, DCCPS, surveillance research program, cancer statistics branch, released april 2011, based on the november 2010 submission." [Online]. Available: http://www.seer.cancer.gov

[2] M. Klemm, I. Craddock, J. Leendertz, A. Preece, and R. Benjamin, "Experimental and clinical results of breast cancer detection using UWB microwave radar," in *Antennas and Propagation Society International Symposium, 2008. AP-S 2008. IEEE*, Jul. 2008, pp. 1 –4.

[3] M. Klemm, D. Gibbins, J. Leendertz, T. Horseman, A. Preece, R. Benjamin, and I. Craddock, "Development and testing of a 60-element uwb conformal array for breast cancer imaging," in *Proc. of the 5th European Conference on Antennas and Propagation*, april 2011, pp. 3077–3079.

[4] C. Charles and D. Allstot, "A buffered charge pump with zero charge sharing," in *Circuits and Systems, 2008. ISCAS 2008. IEEE International Symposium on*, may 2008, pp. 2633 –2636.

[5] E. Fear, X. Li, S. Hagness, and M. Stuchly, "Confocal microwave imaging for breast cancer detection: localization of tumors in three dimensions," *IEEE Trans. Biomed. Eng.*, vol. 49, no. 8, pp. 812 –822, Aug. 2002.

[6] E. Fear, P. Meaney, and M. Stuchly, "Microwaves for breast cancer detection?" *IEEE Potentials*, vol. 22, no. 1, pp. 12 – 18, Feb. 2003.

[7] E. Bond, X. Li, S. Hagness, and B. Van Veen, "Microwave imaging via space-time beamforming for early detection of breast cancer," *IEEE Trans. Antennas Propag.*, vol. 51, no. 8, pp. 1690 – 1705, Aug. 2003.

[8] P. Meaney, M. Fanning, T. Zhou, A. Golnabi, S. Geimer, and K. Paulsen, "Clinical microwave breast imaging - 2D results and the evolution to 3D," in *International Conference on Electromagnetics in Advanced Applications*, Sep. 2009, pp. 881 –884.

[9] D. Kurrant, E. Fear, and D. Westwick, "Tumor response estimation in radar-based microwave breast cancer detection," *IEEE Trans. Biomed. Eng.*, vol. 55, no. 12, pp. 2801 –2811, Dec. 2008.

[10] N. Irishina, M. Moscoso, and O. Dorn, "Microwave imaging for early breast cancer detection using a shape-based strategy," *IEEE Trans. Biomed. Eng.*, vol. 56, no. 4, pp. 1143 –1153, Apr. 2009.

[11] D. Winters, J. Shea, P. Kosmas, B. Van Veen, and S. Hagness, "Three-dimensional microwave breast imaging: dispersive dielectric properties estimation using patient-specific basis functions," *IEEE Trans. Med. Imag.*, vol. 28, no. 7, pp. 969 –981, Jul. 2009.

[12] H. B. Lim, N. T. T. Nhung, E.-P. Li, and N. D. Thang, "Confocal microwave imaging for breast cancer detection: delay-multiply-and-sum image reconstruction algorithm," *IEEE Trans. Biomed. Eng.*, vol. 55, no. 6, pp. 1697 –1704, Jun. 2008.

[13] S. Davis, B. Van Veen, S. Hagness, and F. Kelcz, "Breast tumor characterization based on ultrawideband microwave backscatter," *IEEE Trans. Biomed. Eng.*, vol. 55, no. 1, pp. 237 –246, Jan. 2008.

[14] Y. Chen and P. Kosmas, "Detection and localization of tissue malignancy using contrast-enhanced microwave imaging: Exploring information theoretic criteria," *Biomedical Engineering, IEEE Transactions on*, vol. PP, no. 99, p. 1, 2011.

[15] S. J. Nass, I. C. Henderson, and J. C. Lashof, *Mammography and beyond: developing technologies for the early detection of breast cancer*. National Cancer Policy Board, Institute of Medicine, Division of Earth and Life Studies, National Research Council, 2001.

[16] P. T. Huynh, A. M. Jarolimek, and S. Daye, "The false-negative mammogram," *Radiograph*, vol. 18, no. 5, pp. 1137–1154, 1998.

[17] N. Nikolova, "Microwave Imaging for Breast Cancer," *IEEE Microwave Magazine*, vol. 12, no. 7, pp. 78–94, Dec. 2011.

[18] E. Fear, S. Hagness, P. Meaney, M. Okoniewski, and M. Stuchly, "Enhancing breast tumor detection with near-field imaging," *IEEE Microwave Magazine*, vol. 3, no. 1, pp. 48–56, Mar. 2002.

[19] M. Lazebnik, D. Popovic, L. McCartney, C. B. Watkins, M. J. Lindstrom, J. Harter, S. Sewall, T. Ogilvie, A. Magliocco, T. M. Breslin, W. Temple, D. Mew, J. H. Booske, M. Okoniewski, and S. C. Hagness, "A large-scale study of the ultrawideband microwave dielectric properties of normal, benign and malignant breast tissues obtained from cancer surgeries," *Physics in Medicine and Biology*, vol. 52, no. 20, p. 6093, 2007.

[20] T. Henriksson, M. Klemm, D. Gibbins, J. Leendertz, T. Horseman, A. Preece, R. Benjamin, and I. Craddock, "Clinical trials of a multistatic UWB radar for breast imaging," in *Loughborough Antennas and Propagation Conference*, nov. 2011, pp. 1–4.

[21] Y. Xing, K. D. Cromwell, and J. N. Cormier, "Review of diagnostic imaging modalities for the surveillance of melanoma patients," *Dermatology Research and Practice*, vol. 2012, no. 4, pp. 12–6, 2012.

[22] Y.-A. Li, M.-H. Hung, S.-J. Huang, and J. Lee, "A fully integrated 77GHz FMCW radar system in 65nm CMOS," in *IEEE ISSCC Digest of Technical Papers*, feb. 2010, pp. 216–217.

[23] T.-Y. Kao, A.-K. Chen, Y. Yan, T.-M. Shen, and J. Lin, "A flip-chip-packaged and fully integrated 60 GHz CMOS micro-radar sensor for heartbeat and mechanical vibration detections," in *IEEE Radio Frequency Integrated Circuits Symposium*, june 2012, pp. 443–446.

[24] A. Tang, G. Virbila, D. Murphy, F. Hsiao, Y. Wang, Q. Gu, Z. Xu, Y. Wu, M. Zhu, and M.-C. Chang, "A 144GHz 0.76cm-resolution sub-carrier SAR phase radar for 3D imaging in 65nm CMOS," in *IEEE ISSCC Digest of Technical Papers*, feb. 2012, pp. 264–266.

[25] M. Tiebout, H. Wohlmuth, H. Knapp, R. Salerno, M. Druml, M. Rest, J. Kaeferboeck, J. Wuertele, S. Ahmed, A. Schiessl, R. Juenemann, and A. Zielska, "Low power wideband receiver and transmitter chipset for mm-wave imaging in SiGe bipolar technology," *IEEE Journal of Solid-State Circuits*, vol. 47, no. 5, pp. 1175–1184, may 2012.

[26] D. R. Wehner, *High Resolution Radar*. Boston: Artech House Radar, 1994.

[27] M. Bialkowski, "Ultra wideband microwave system with novel image reconstruction strategies for breast cancer detection," in *European Microwave Conference*, sept. 2010, pp. 537–540.

[28] S. Ahmed, A. Schiessl, and L.-P. Schmidt, "A novel fully electronic active real-time imager based on a planar multistatic sparse array," *IEEE Trans. on Microwave Theory and Techniques*, vol. 59, no. 12, pp. 3567–3576, dec. 2011.

[29] C. Clemente, *Gray's Anatomy of the Human Body*. Lea & Febiger, 1985.

[30] W. H. Parsons, *Cancer of the Breast*. Springfield, IL: Thomas, 1959.

[31] J. Y. Wo, K. Chen, B. A. Neville, N. U. Lin, and R. S. Punglia, "Effect of very small tumor size on cancer-specific mortality in node-positive breast cancer," *J Clin Oncol*, May 2011.

[32] J. S. Michaelson, M. Silverstein, W. J., G. Weber, R. Moore, E. Halpern, D. Kopans, and K. Hughes, "Predicting the survival of patients with breast carcinoma using tumor size," *J Cancer*, Aug 2002.

[33] M. Hussain, "Ultra-wideband impulse radar-an overview of the principles," *IEEE Trans. Aerosp. Electron. Syst.*, vol. 13, no. 9, pp. 9 –14, sep 1998.

[34] ——, "Principles of space-time array processing for ultrawide-band impulse radar and radio communications," *IEEE Trans. Veh. Technol.*, vol. 51, no. 3, pp. 393 –403, may 2002.

[35] X. Li and S. Hagness, "A confocal microwave imaging algorithm for breast cancer detection," *IEEE Microw. Wireless Compon. Lett.*, vol. 11, no. 3, pp. 130 –132, Mar. 2001.

[36] D. Winters, B. Van Veen, and S. Hagness, "UWB microwave imaging for breast cancer detection: an algorithm for estimating the breast surface," in *IEEE Antennas and Propagation Society International Symposium*, july 2006, pp. 267–270.

[37] T. Williams, E. Fear, and D. Westwick, "Tissue sensing adaptive radar for breast cancer detection: investigations of reflections from the skin," in *IEEE Antennas and Propagation Society International Symposium*, vol. 3, june 2004, pp. 2436–2439.

[38] M. Bassi, A. Bevilacqua, A. Gerosa, and A. Neviani, "Integrated transceivers for UWB breast cancer imaging: Architecture and circuit constraints," in *Circuits and Systems (ISCAS), 2011 IEEE International Symposium on*, may 2011, pp. 2087 –2090.

[39] ——, "Integrated SFCW transceivers for UWB breast cancer imaging: Architectures and circuit constraints," *IEEE Trans. on Circuits and Systems I: Regular Papers*, vol. 59, no. 6, pp. 1228–1241, june 2012.

[40] X. Li, S. Davis, S. Hagness, D. van der Weide, and B. Van Veen, "Microwave imaging via space-time beamforming: experimental investigation of tumor detection in multilayer breast phantoms," *IEEE Trans. Microw. Theory Tech.*, vol. 52, no. 8, pp. 1856 – 1865, 2004.

[41] X. Li, E. Bond, B. Van Veen, and S. Hagness, "An overview of ultra-wideband microwave imaging via space-time beamforming for early-stage breast-cancer detection," *IEEE Antennas Propag. Mag.*, vol. 47, no. 1, pp. 19 – 34, Feb. 2005.

[42] B. Razavi, *RF microelectronics*. Prentice Hall PTR, 1998.

[43] S. Hagness, A. Taflove, and J. Bridges, "Three-dimensional FDTD analysis of a pulsed microwave confocal system for breast cancer detection: design of an antenna-array element," *IEEE Trans. Antennas Propag.*, vol. 47, no. 5, pp. 783 –791, May 1999.

[44] E. Fear and M. Stuchly, "Microwave system for breast tumor detection," *IEEE Microw. Guided Wave Lett.*, vol. 9, no. 11, pp. 470 –472, Nov. 1999.

[45] S. Hagness, A. Taflove, and J. Bridges, "Two-dimensional FDTD analysis of a pulsed microwave confocal system for breast cancer detection: fixed-focus and antenna-array sensors," *IEEE Trans. Biomed. Eng.*, vol. 45, no. 12, pp. 1470 –1479, Dec. 1998.

[46] A. F. Oskooi, D. Roundy, M. Ibanescu, P. Bermel, J. D. Joannopoulos, and S. G. Johnson, "MEEP: A flexible free-software package for electromagnetic simulations by the FDTD method," *Computer Physics Communications*, vol. 181, pp. 687–702, January 2010.

[47] ET Industries, "180 degree hybrid coupler-stripline design technical datasheet." [Online]. Available: http://www.etiworld.com/rf.pass.comp/180.Degree.Hybrid.Stripline.html

[48] J. E. Chen, "Modeling RF systems," 2005. [Online]. Available: http://www.designers-guide.org/Modeling/

[49] W. Sheng, A. Emira, and E. Sanchez-Sinencio, "CMOS RF receiver system design: a systematic approach," *IEEE Trans. Circuits Syst. I*, vol. 53, no. 5, pp. 1023 – 1034, may 2006.

[50] C. Enz and G. Temes, "Circuit techniques for reducing the effects of op-amp imperfections: autozeroing, correlated double sampling, and chopper stabilization," *Proc. IEEE*, vol. 84, no. 11, pp. 1584 –1614, Nov. 1996.

[51] S. Rong and H. Luong, "A 0.05-to-10GHz 19-to-22GHz and 38-to-44GHz SDR frequency synthesizer in 0.13 $\mu$m CMOS," in *Proceedings of IEEE International Solid-State Circuits Conference (ISSCC)*, feb. 2011, pp. 464 –466.

[52] S. Toso, A. Bevilacqua, M. Tiebout, N. Da Dalt, A. Gerosa, and A. Neviani, "A 0.06 mm$^2$ 11 mw local oscillator for the GSM standard in 65 nm CMOS," *IEEE J. Solid-State Circuits*, vol. 45, no. 7, pp. 1295 –1304, july 2010.

[53] S. Dal Toso, A. Bevilacqua, M. Tiebout, N. Da Dalt, A. Gerosa, and A. Neviani, "An integrated divide-by-two direct injection-locking frequency divider for bands $s$ through $k_u$," *IEEE Trans. Microw. Theory Tech.*, vol. 58, no. 7, pp. 1686 –1695, july 2010.

[54] A. Bevilacqua, F. P. Pavan, C. Sandner, A. Gerosa, and A. Neviani, "A 3.4-7 GHz transformer-based dual-mode wideband VCO," in *Proceedings of the 32nd European Solid-State Circuits Conference (ESSCIRC)*, sept. 2006, pp. 440 –443.

[55] J. Borremans, A. Bevilacqua, S. Bronckers, M. Dehan, M. Kuijk, P. Wambacq, and J. Craninckx, "A compact wideband front-end using a single-inductor dual-band VCO in 90 nm digital CMOS," *IEEE J. Solid-State Circuits*, vol. 43, no. 12, pp. 2693 –2705, dec. 2008.

[56] A. Bevilacqua and A. Niknejad, "An ultrawideband CMOS low-noise amplifier for 3.1-10.6-GHz wireless receivers," *IEEE J. Solid-State Circuits*, vol. 39, no. 12, pp. 2259 – 2268, dec. 2004.

[57] F. Bruccoleri, E. Klumperink, and B. Nauta, "Wide-band CMOS low-noise amplifier exploiting thermal noise canceling," *IEEE J. Solid-State Circuits*, vol. 39, no. 2, pp. 275 – 282, feb. 2004.

[58] A. Bevilacqua, M. Camponeschi, M. Tiebout, A. Gerosa, and A. Neviani, "Design of broadband inductorless LNAs in ultra-scaled CMOS technologies," in *IEEE International Symposium on Circuits and Systems (ISCAS)*, may 2008, pp. 1300 –1303.

[59] S. Blaakmeer, E. Klumperink, D. Leenaerts, and B. Nauta, "Wideband balun-LNA with simultaneous output balancing, noise-canceling and distortion-canceling," *IEEE Journal of Solid-State Circuits*, vol. 43, no. 6, pp. 1341–1350, June 2008.

[60] P. Kinget, R. Melville, D. Long, and V. Gopinathan, "An injection-locking scheme for precision quadrature generation," *IEEE J. Solid-State Circuits*, vol. 37, no. 7, pp. 845 –851, jul 2002.

[61] M. Bassi, M. Caruso, A. Bevilacqua, and A. Neviani, "A 1.75–15 GHz stepped frequency receiver for breast cancer imaging in 65nm CMOS," in *Proc. of the IEEE European Solid-State Circuits Conference*, 2012, pp. 353–356.

[62] V. Giannini, P. Nuzzo, C. Soens, K. Vengattaramane, J. Ryckaert, M. Goffioul, B. Debaillie, J. Borremans, J. Van Driessche, J. Craninckx, and M. Ingels, "A 2-mm$^2$ 0.1–5 GHz software-defined radio receiver in 45-nm digital CMOS," *IEEE Journal of Solid-State Circuits*, vol. 44, no. 12, pp. 3486–3498, Dec. 2009.

[63] A. Goel, B. Analui, and H. Hashemi, "A 130-nm CMOS 100-Hz–6-GHz reconfigurable vector signal analyzer and software-defined receiver," *IEEE Transactions on Microwave Theory and Techniques*, vol. 60, no. 5, pp. 1375–1389, May 2012.

[64] D. Leenaerts, R. van de Beek, J. Bergervoet, H. Kundur, G. van der Weide, A. Kapoor, T. Y. Pu, Y. Fang, Y. J. Wang, B. Mukkada, H. Lim, V. Kiran, C. S. Lim, S. Badiu, and A. Chang, "A 65 nm CMOS inductorless triple band group WiMedia UWB PHY," *IEEE Journal of Solid-State Circuits*, vol. 44, no. 12, pp. 3499–3510, Dec. 2009.

[65] O. Werther, M. Cavin, A. Schneider, R. Renninger, B. Liang, L. Bu, Y. Jin, J. Rogers, and J. Marcincavage, "A fully integrated 14 band, 3.1 to 10.6 GHz 0.13 $\mu$m SiGe BiCMOS UWB RF transceiver," *IEEE Journal of Solid-State Circuits*, vol. 43, no. 12, pp. 2829–2843, Dec. 2008.

[66] S. Chehrazi, A. Mirzaei, and A. Abidi, "Noise in current-commutating passive fet mixers," *IEEE Transactions on Circuits and Systems I: Regular Papers*, vol. 57, no. 2, pp. 332 –344, feb. 2010.

[67] C. Enz, E. Vittoz, and F. Krummenacher, "A CMOS chopper amplifier," *IEEE Journal of Solid-State Circuits*, vol. 22, no. 3, pp. 335–342, Jun 1987.

[68] A. Bakker, K. Thiele, and J. Huijsing, "A CMOS nested-chopper instrumentation amplifier with 100-nV offset," *IEEE Journal of Solid-State Circuits*, vol. 35, no. 12, pp. 1877–1883, Dec. 2000.

[69] R. Wu, K. Makinwa, and J. Huijsing, "A chopper current-feedback instrumentation amplifier with a 1 mHz 1/f noise corner and an ac-coupled ripple reduction loop," *IEEE Journal of Solid-State Circuits*, vol. 44, no. 12, pp. 3232–3243, Dec. 2009.

[70] J.-C. Chien and L.-H. Lu, "Analysis and design of wideband injection-locked ring oscillators with multiple-input injection," *IEEE Journal of Solid-State Circuits*, vol. 42, no. 9, pp. 1906–1915, 2007.

[71] T.-S. Chu and H. Hashemi, "A CMOS UWB camera with 7×7 simultaneous active pixels," in *IEEE ISSCC Digest of Technical Papers*, Feb. 2008, pp. 120–121.

[72] K. Kundert, *Phase-Locking in High Performance Systems*. Behzad Razavi (editor), IEEE Press, 2003.

[73] D. Banerjee, *PLL performance, simulation and design*. Available Online, 2006.

[74] S. Cheng, H. Tong, J. Silva-Martinez, and A. Karsilayan, "Design and analysis of an ultrahigh-speed glitch-free fully differential charge pump with minimum output current variation and accurate matching," *Circuits and Systems II: Express Briefs, IEEE Transactions on*, vol. 53, no. 9, pp. 843 –847, sept. 2006.

[75] H. Shanan, G. Retz, K. Mulvaney, and P. Quinlan, "A 2.4ghz 2mb/s versatile PLL-based transmitter using digital pre-emphasis and auto calibration in 0.18 $\mu m$ CMOS for WPAN," in *Solid-State Circuits Conference - Digest of Technical Papers, 2009. ISSCC 2009. IEEE International*, feb. 2009, pp. 420 –421,421a.

[76] S. D. Toso, "Analysis and design of injection-locked building blocks for rf frequency generation in ultra-scaled CMOS technologies," Ph.D. dissertation, University of Padova, Italy, 2010.

[77] C. Vaucher, I. Ferencic, M. Locher, S. Sedvallson, U. Voegeli, and Z. Wang, "A family of low-power truly modular programmable dividers in standard 0.35-$\mu$m CMOS technology," *Solid-State Circuits, IEEE Journal of*, vol. 35, no. 7, pp. 1039 –1045, july 2000.

[78] S. Rong and H. Luong, "A 0.05-to-10ghz 19-to-22ghz and 38-to-44ghz SDR frequency synthesizer in 0.13 $\mu$m CMOS," in *Solid-State Circuits Conference Digest of Technical Papers (ISSCC), 2011 IEEE International*, feb. 2011, pp. 464 –466.

[79] M. Kossel, T. Morf, J. Weiss, P. Buchmann, C. Menolfi, T. Toifl, and M. Schmatz, "LC PLL with 1.2-octave locking range based on mutual-inductance switching in 45-nm SOI CMOS," *Solid-State Circuits, IEEE Journal of*, vol. 44, no. 2, pp. 436 –449, feb. 2009.

[80] J. Borremans, K. Vengattaramane, V. Giannini, B. Debaillie, W. Van Thillo, and J. Craninckx, "A 86 mhz-12 ghz digital-intensive PLL for software-defined radios, using a 6 fj/step TDC in 40 nm digital CMOS," *Solid-State Circuits, IEEE Journal of*, vol. 45, no. 10, pp. 2116 –2129, oct. 2010.

[81] J.-Y. Lee, S.-H. Lee, H. Kim, and H.-K. Yu, "A 28.5-32-ghz fast settling multichannel PLL synthesizer for 60-ghz WPAN radio," *Microwave Theory and Techniques, IEEE Transactions on*, vol. 56, no. 5, pp. 1234 –1246, may 2008.

[82] S. Osmany, F. Herzel, and J. Scheytt, "An integrated 0.6-4.6 ghz, 5-7 ghz, 10-14 ghz, and 20-28 ghz frequency synthesizer for software-defined radio applications," *Solid-State Circuits, IEEE Journal of*, vol. 45, no. 9, pp. 1657 –1668, sept. 2010.

[83] O. Richard, A. Siligaris, F. Badets, C. Dehos, C. Dufis, P. Busson, P. Vincent, D. Belot, and P. Urard, "A 17.5-to-20.94ghz and 35-to-41.88ghz PLL in 65nm CMOS for wireless HD applications," in *Solid-State Circuits Conference Digest of Technical Papers (ISSCC), 2010 IEEE International*, feb. 2010, pp. 252 –253.

[84] B. Floyd, "A 15 to 18-ghz programmable sub-integer frequency synthesizer for a 60-ghz transceiver," in *Radio Frequency Integrated Circuits (RFIC) Symposium, 2007 IEEE*, june 2007, pp. 529 –532.

[85] J. Osorio, C. Vaucher, B. Huff, E. v.d. Heijden, and A. de Graauw, "A 21.7-to-27.8ghz 2.6-degrees-rms 40mw frequency synthesizer in 45nm CMOS for mm-wave communication applications," in *Solid-State Circuits Conference Digest of Technical Papers (ISSCC), 2011 IEEE International*, feb. 2011, pp. 278 –280.

[86] M. Caruso, M. Bassi, A. Bevilacqua, and A. Neviani, "A 2-16 ghz 204 mw 3 mm-resolution stepped frequency radar for breast cancer diagnostic imaging in 65 nm cmos," in *IEEE ISSCC Digest of Technical Papers - accepted for publication*, Feb. 2013.

[87] M. Bassi, M. Caruso, A. Bevilacqua, and A. Neviani, "An integrated microwave imaging radar with planar antennas for breast cancer detection," *Microwave Theory and Techniques, IEEE Transactions on - accepted for publication*.

[88] T.-G. Ma and S.-K. Jeng, "Planar miniature tapered-slot-fed annular slot antennas for ultrawide-band radios," *Antennas and Propagation, IEEE Transactions on*, vol. 53, no. 3, pp. 1194 – 1202, march 2005.

[89] S.-Y. Suh, W. Stutzman, and W. Davis, "A new ultrawideband printed monopole antenna: the planar inverted cone antenna (pica)," *Antennas and Propagation, IEEE Transactions on*, vol. 52, no. 5, pp. 1361 – 1364, may 2004.

[90] M. Sun, Y. P. Zhang, and Y. Lu, "Miniaturization of planar monopole antenna for ultrawideband radios," *Antennas and Propagation, IEEE Transactions on*, vol. 58, no. 7, pp. 2420 –2425, july 2010.

[91] S. W. T. P. J. Heijmink, J. J. Futterer, S. S. Strum, W. J. G. Oyen, F. Frauscher, J. A. Witjes, and J. O. Barentsz, "State-of-the-art uroradiologic imaging in the diagnosis of prostate cancer," *Acta Oncologica*, vol. 50, no. S1, pp. 25–38, 2011.

[92] S. Semenov, "Microwave tomography: review of the progress towards clinical applications," *Philosophical Transactions of the Royal Society A: Mathematical, Physical and Engineering Sciences*, vol. 367, no. 1900, pp. 3021–3042, 2009.

[93] S. Solda, M. Caruso, A. Bevilacqua, A. Gerosa, D. Vogrig, and A. Neviani, "A 5 Mb/s UWB-IR transceiver front-end for wireless sensor networks in 0.13 $\mu$m CMOS," *Solid-State Circuits, IEEE Journal of*, vol. 46, no. 7, pp. 1636 –1647, july 2011.